DIRECTIONAL WAVEFIELD DECOMPOSITION OF SNAPSHOTS OF ACOUSTIC WAVEFIELDS

DIRECTIONAL WAVEFIELD DECOMPOSITION OF SNAPSHOTS OF ACOUSTIC WAVEFIELDS

Proefschrift

ter verkrijging van de graad van doctor
aan de Technische Universiteit Delft,
op gezag van de Rector Magnificus
prof. dr. ir. T.H.J.J van der Hagen,
voorzitter van het College voor Promoties,
in het openbaar te verdedigen op
maandag 18 mei 2020 om 12:30 uur.

door

Max Enno HOLICKI

M.Sc. in Applied Geophysics,
IDEA League Programma (Delft, Zürich, Aachen)
geboren te Stade, Duitsland.

Dit proefschrift is goedgekeurd door de promotoren:

Dr. ir. G.G. Drijkoningen
Prof. dr. ir. C.P.A. Wapenaar

Samenstelling promotiecommissie:

Rector Magnificus	voorzitter
Dr. ir. G.G. Drijkoningen	Technische Universiteit Delft
Prof. dr. ir. C.P.A. Wapenaar	Technische Universiteit Delft
Onafhankelijke leden:	
Prof. dr. ir. E.C. Slob	Technische Universiteit Delft
Prof. dr. ir. L.G. Evers	Technische Universiteit Delft
Prof. dr. J.O.A. Robertsson	Eidgenössische Technische Hochschule Zürich
Dr. ir. D.J. Verschuur	Technische Universiteit Delft
Dr. ir. R.F. Hegge	Aramco Overseas Company B.V.

Keywords: Acoustic, Snapshot, Wavefield Decomposition, Imaging, RTM

Printed by: ProefschriftMaken || www.proefschriftmaken.nl

ISBN 978-94-6366-277-2

An electronic version of this dissertation is available at
http://repository.tudelft.nl/.

To the wonders of the world,
which we can experience due
to our progenitors' never-
ending strive to survive.
Danke Birgit & Peter

Max Holicki

CONTENTS

SUMMARY

In acoustic exploration and monitoring imaging plays a critical role in uncovering structure and minute changes therein. It is, however, often hampered by unfulfilled assumptions. One such assumption in the context of reflection imaging is that estimated incident and reflected wavefields at a reflector travel in opposite directions with respect to the reflector surface-normal vector. In Reverse Time Migration (RTM) this is often not the case due to the common use of modelling operators that implicitly account for scattering to estimate incident and reflected wavefields at an interface. This results in artefacts in the output RTM image.

A partial remedy to these artefacts is to directionally decompose wavefields during the RTM imaging step. This allows for the decomposition of the incident wavefield at a horizontal interface into a down-going wavefield, which in conjunction with the up-going reflected wavefield can be used to estimate the reflectivity at the interface. This effectively removes the possibility of using a down-going incident wavefield with a down-going reflected wavefield to estimate reflectivity, which is not physical.

Directional wavefield decomposition classically decomposes multicomponent wavefields recorded along a horizontal surface into up- and down-going wavefields. For acoustics this is a solved problem. However, not all techniques implicitly use wavefields recorded along flat surfaces. RTM, for example, commonly works on snapshots of a wavefield, hence the classical decomposition techniques are hardly applicable. Other techniques have been developed to solve this problem, but still only decompose into up- and down-going wavefields as it is assumed that the media of interest only vary in the vertical direction. None allow for an elegant decomposition of a wavefield according to all possible travel directions. In this thesis (Chapter 2) we develop a snapshot acoustic directional wavefield decomposition technique with an emphasis on the fact that the method works on snapshots of wavefields in time and that the direction with respect to which the decomposition occurs is arbitrary, and not simply the vertical direction as in up-down decomposition. Like other decomposition techniques it is effectuated through the scaled addition of two wavefield components, in this case the pressure and its time derivative. We demonstrate how to directionally decompose an acoustic wavefield according to the directions of propagation of its constituent plane waves by showing how to separate a wavefield into its constituent plane waves. This allows for approximate wavefield decomposition in arbitrary media, even normal to interfaces. This is an obvious boon for imaging complex structures, as imaging should occur normal to surfaces and not only in the vertical direction. This method is designed for wavefields that exist in one or more spatial dimensions and the locally varying decomposition directions must be prescribed by the user.

As this method is fundamentally new, we relate it to well established decomposition techniques (Chapter 3). We compare Poynting decomposition, plane-wave decomposition, analytic decomposition and conventional surface-normal decomposition to our

snapshot wavefield decomposition and mathematically derive the other techniques in terms of acoustic snapshot directional wavefield decomposition. This underpins the validity of snapshot directional wavefield decomposition as a proper decomposition technique and allows for the exposure of the limitations, advantages and disadvantages of each of the discussed techniques.

The preceding discussion is complemented by looking at directionally decomposing simple plane-wave examples (Chapter 4). In the first example two interfering propagating plane waves that travel in opposite vertical directions are considered and are promptly separated by decomposing the wavefield into up- and down-going waves using our proposed decomposition operators. The second example is more challenging as spatially evanescent waves are considered. Such waves are diffusive in one or more spatial dimensions. In this case our proposed decomposition operators break down and we are not able to correctly decompose the wavefield.

As already stated the newly developed decomposition scheme can be used for improving imaging in RTM (Chapter 5). By directionally decomposing wavefields normal to interfaces the concept of a reflection coefficient is honoured. Conventionally wavefields are decomposed into up- and down-going waves before imaging, which stems from the assumption that the Earth is horizontally layered. This removes backscatter artefacts from RTM images that are caused by the use of modelling operators that implicitly account for scattering when the medium only varies in the vertical direction. The Earth, however, is rarely horizontally layered. Most interesting structures like salt flanks or faults are commonly more vertical than horizontal. Imaging using decomposed up- and down-going wavefields performs poorly for these. Imaging using wavefields decomposed according to interface normals is the key here. It is expensive but effective for all dips.

As part of this work field data were acquired and processed along a transect in the Danube near Novi Sad, Serbia. Although these data were not initially shot for showing the newly developed decomposition method, we applied it successfully to these field data (Appendix A). This demonstrates that the operators perform well under real field conditions with ample of noise present.

SAMENVATTING

Bij akoestische exploratie en monitoring speelt beeldvorming een cruciale rol voor het ontdekken van structuren en de minuscule veranderingen in deze structuren. Deze waarnemingen worden echter vaak bemoeilijkt vanwege onvervulde aannames. Een van zulke aannames in de context van het afbeelden van reflecties is dat de geschatte inkomende en gereflecteerde golfvelden bij een reflector in tegengestelde richting bewegen ten opzichte van de vector die loodrecht op het oppervlak van de reflector staat. Bij Reverse Time Migration (RTM) is dit vaak niet het geval omdat de inkomende en gereflecteerde golfvelden bij een grensvlak over het algemeen geschat worden met behulp van modelleringsoperatoren gebaseerd op verstrooiing. Dit resulteert in fouten in het RTM-gevormde beeld.

Het ontbinden van het golfveld in afzonderlijke richtingen tijdens het vormen van het RTM-beeld kan deze fouten voor een deel verminderen. Door toe te staan dat het inkomende golfveld bij het grensvlak ontbonden wordt in een neergaand veld, kan deze richtingsafhankelijke ontbinding gebruikt worden in combinatie met het opgaande gereflecteerde veld om de reflectiviteit aan het grensvlak te bepalen. Hierdoor wordt de mogelijkheid verwijderd dat het neergaande inkomende veld en het neergaande gereflecteerde veld worden gebruikt om de reflectiviteit te schatten, wat niet-fysisch is.

Historisch gezien wordt richtingsafhankelijk ontbinding van het golfveld gebruikt om golfvelden die via verschillende componenten gemeten zijn langs een horizontaal oppervlak, om te zetten in op- en neergaande golfvelden. Voor akoestische golfvelden is dit een opgelost probleem. Echter, niet alle technieken maken impliciet gebruik van golfvelden die gemeten zijn langs platte oppervlakken. RTM maakt bijvoorbeeld gebruik van momentopnames van het golfveld, waardoor conventionele technieken voor ontbinding van het golfveld nauwelijks toepasbaar zijn. Andere technieken zijn ontwikkeld om dit probleem op te lossen, maar deze maken nog steeds enkel gebruik van op- en neergaande golfvelden omdat ze aannemen dat de media van belang alleen veranderen in de verticale richting. Geen van deze technieken maakt gebruik van een elegante ontbinding in alle mogelijke richtingen. In dit proefschrift (Hoofdstuk 2) ontwikkelen we een methode om momentopnames van akoestische golfvelden te ontbinden in verschillende richtingen, met nadruk op het feit dat de methode werkt op momentopnames in tijd en dat de richting waarin de ontbinding plaatsvindt arbitrair is en niet alleen in verticale richting. Zoals in andere decompositietechnieken wordt dit geeffectueerd via een geschaalde optelling van twee componenten van het golfveld, in dit geval de druk en zijn tijdafgeleid. We laten zien hoe een akoestisch golfveld ontbonden kan worden in de richting van de voortplanting van de bijbehorende vlakke golven door te laten zien hoe het golfveld gescheiden kan worden in zijn bijbehorende vlakke golven. Dit laat een benadering in golfveldontbinding toe voor ieder type media, zelfs als de ontbindingsrichting

Vertaald door: J.A. Brackenhoff & G.G. Drijkoningen.

loodrecht op de grensvlakken staat. Dit is een duidelijk voordeel voor de beeldvorming van complexe structuren aangezien beeldvorming loodrecht op de vlakken zou moeten plaatsvinden en niet alleen in de verticale richting. Deze methode is ontwropen voor geolfvelden die in één of meer spatiele dimensies bestaan, en de lokaal vari erende decompositierichting moet voorgeschreven worden door de gebruiker.

Aangezien deze methode fundamenteel nieuw is, wordt het gerelateerd aan goedvastgestelde ontbindingstechnieken (Hoofdstuk 3). De zogenaamde Poynting ontbinding, een vlakke-golf ontbinding, een ontbinding in termen van (complexe) analytische functies en een conventionele ontbinding loodrecht op het oppervlak worden vergeleken met de ontbinding van die van ons, die met momentopnames van het golfveld, en we leiden deze andere technieken af in termen van richtingsafhankelijke ontbinding van akoestische golfvelden via momentopnames. Dit laat zien dat deze methode de juiste manier van ontbinden is en laat de beperkingen, voordelen en nadelen van de verschillende technieken zien.

De voorafgaande discussie wordt aangevuld door te kijken naar het richtingsafhankelijk ontbinden van simpele vlakke-golf voorbeelden (Hoofdstuk 4). In het eerste voorbeeld worden twee interfererende golven beschouwd die in tegengestelde verticale richtingen bewegen en die ontbonden worden in op- en neergaande golven, gebruik makende van onze ontbindingsoperatoren. Het tweede voorbeeld is uitdagender aangezien ze spatieel uitdovend, ofwel “evanescent”, zijn. Deze golven zijn diffusief in een of meer ruimtelijke dimensies. In dit geval werken onze ontbindingsoperatoren niet langer en moeten ze uitgebreid worden voor complexe golfgetallen. Gebruik makende van de uitgebreidere ontbindingsoperatoren kan het golfveld ook op de juiste manier ontbonden worden.

Zoals eerder aangegeven kan het nieuw-ontwikkelde ontbindingsschema gebruikt worden om beeldvorming met RTM te verbeteren (Hoofdstuk 5). Door golfvelden richtingsafhankelijk te ontbinden loodrecht op de grensvlakken, wordt het concept van een reflectiecoëfficiënt gehonoreerd. Conventioneel worden golfvelden ontbonden in op- en neergaande golven voordat de beeldvorming plaatsvindt, waarin de aanname ligt dat de aarde horizontaal gelaagd is. Dit verwijdert teruggekaatste artefacten uit RTM beelden die veroorzaakt worden door het gebruik van gemodelleerde verstrooiingsoperatoren in het geval dat het medium alleen in de verticale richting verandert. De aarde is echter zelden horizontaal gelaagd. De meest interessante structuren, zoals de flanken van zoutdiapieren of breuken, zijn normaliter meer verticaal dan horizontaal. Beeldvorming met behulp van ontbinding in op- en neergaande golfvelden doen het slecht in zulke gevallen. Daarom is het gebruik van golfvelden die zijn ontbonden in een richting die loodrecht op de grensvlakken staat, in dit geval de sleutel. Het is duur maar effectief voor alle hellingen.

Als gedeelte van dit werk zijn veldgegevens opgenomen langs een traject in de rivier de Donau, vlakbij Novi Sad in Servië, en deze gegevens zijn later bewerkt. Alhoewel deze gegevens aanvankelijk niet werden gemeten voor het valideren van de nieuwontwikkelde ontbindingsmethode, hebben wij deze methode met succes toegepast op deze gegevens (Bijlage A). Hiermee tonen we aan dat de operatoren ook goed werken op gegevens onder werkelijke veldcondities, onder de aanwezigheid van veel ruis.

1

INTRODUCTION

1.1. WHAT IS EXPLORATION SEISMOLOGY?

Understanding our planet is becoming quintessential to humanity. The rapid changes of our planet, like those brought about by climate change and humanity's unending thirst for resources to sustain its population growth and living standards, make it more important than ever to understand what is below our feet.

Geophysics is the study of just that. It aims to physically explain the processes and material distribution inside planets, with a focus on finding subsurface resources and understanding planetary threats, like earthquakes. As this is still a very large field of study it is often further broken down into two large groups: 1) the study of processes, like the geodynamo that generates the Earth's magnetic field, and 2) the study of techniques to better understand the planet and the processes that go on inside.

Seismology, which is the umbrella under which this thesis falls, is part of the latter. It relates to listening to acoustic and elastic waves that travel in a planet and from them to gain information on the planet's internal structure and composition.

In seismology a distinction is made between exploration seismology and classical seismology. Classical seismology is mainly concerned with using a limited number of spatially fixed highly sophisticated sensors to evaluate the structure and composition of a planet using natural and/or anthropogenic sources, like earthquakes or the detonation of explosives.

In exploration seismology, which is a minimally invasive testing technique, vast arrays of sensors are used in conjunction with controlled sources, like dynamite blasts, to explore the structure of the upper crust of our planet. This is mostly done for the exploration for and later exploitation of fossil fuel reserves. As such, exploration seismology has been heavily industrialized to the point where the current largest man-made objects by spatial extent are seismic acquisition vessels that have deployed their towed streamers. The spatial extend of the vessel and towed streamers can cover an area of up to 17.6 km^2 (Bizley, 2016).

Although many of the concepts explained in this thesis apply to both conventional seismology and seismic exploration, the assumed dense sampling of recorded wavefields

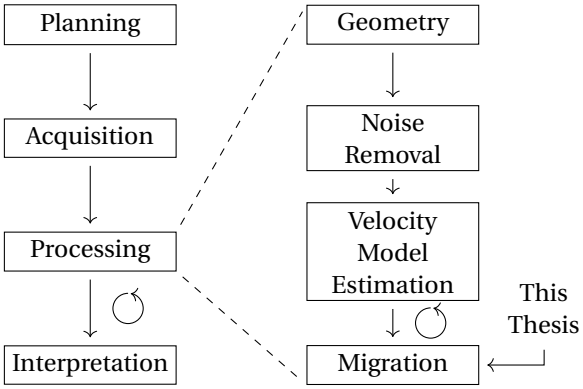

Figure 1.1: Simplified workflow of a seismic exploration campaign on the left. On the right is a simplified processing workflow. Circular arrows indicate stages with a circular feedback to update seismic results. This thesis fits into the migration/imaging part of the processing flow.

is akin to that found in exploration seismology. This places most of this work pertaining to imaging in exploration seismic settings. The application of concepts to synthetic data, however, has merits in both fields.

1.2. THE EXPLORATION-SEISMIC WORKFLOW

The general workflow of a seismic exploration campaign is shown in Figure 1.1, and is exposed in greater detail in Yilmaz (2001). First the campaign is planned, this involves detailing where, when and how the data will be acquired, but also entails communication with stakeholders and permitting. Then the actual seismic acquisition campaign begins.

During acquisition a controlled source, often an impulsive source, is used to generate acoustic/elastic wavefields. Common sources include dynamite blasts, vibroseis, and air guns. Vibroseis affix sufficiently massive base plates to a surface and vibrate these to generate elastic waves, while air guns inject pressurized gas into a fluid to generate a bubble which subsequently collapses and generates acoustic waves in the fluid. Sources range in size from centimeter-scale piezoelectric transducers (commonly used in borehole geophysics or laboratory settings), which function similar to conventional audio speakers, up to atomic blasts, as were used by the Soviet Union (Scheimer and Borg, 1984).

The wavefields resulting from the source propagate into the target medium under investigation and undergo scattering due to changes in medium properties. The scattered wavefields are then sensed by sensors, whose outputs are digitized and recorded. These sensors are often a mix of particle velocity and acoustic pressure sensors. Such recordings are commonly repeated for many sources to acquire sufficient data.

The resultant data are then processed to estimate the internal structure of the volume under investigation. If not already done during acquisition, this processing step begins with the aggregation of metadata regarding the acquisition campaign. This often entails applying location data to the recorded data in a step known as geometry setting. During this stage the data are also often normalized and regularized onto processable spatial grids. At various stages throughout processing the data are also denoised using a range

of filtering techniques to enhance the signal to noise ratio.

Following this the data are used to estimate a wavespeed model of the medium of interest. For this commonly tomographic approaches, which only consider traveltimes, or more advanced techniques like full waveform inversion are used. The generated wavespeed model is then used in conjunction with the preprocessed data in a technique known as migration to form structural images of the medium.

Further processing steps aim at either improving the estimation of medium parameters like the wave speed, elastic coefficients and the density or to improve the structural image. The final structural image then forms the basis of geological models, which are generated by interpreting the images.These are then used to better understand the medium of interest, often with the intent of exploring for and later exploitation of resources.

1.3. THE THESIS IN CONTEXT

This work fits into the context of constructing structural images using acoustic wave theory, see migration in Figure 1.1. Traditionally seismic exploration experiments were simple reflection experiments. This means that it is assumed that only the direct wave from the source to reflectors and the associated reflected waves from the medium are recorded. Multiply reflected waves are disregarded by assuming that the recorded data does not contain them.

Figure 1.2 shows an example of a typical simplified acquisition. A source, denoted by the black dot, excites a wavefield, which we choose to denote using rays. The rays indicate the surface normals to the wavefronts the source produces. The rays and associated wavefronts then propagate downwards into the medium where they are reflected at interfaces and propagate back up to the receivers. During migration this propagation process is undone using a process known as redatuming (Wapenaar and Berkhout, 1989), which moves sources and receivers onto the interface while homogenizing the medium above. Note that these redatumed sources and receivers are not actual sources and receivers; they are virtual. The reflection amplitude of the virtual receivers due to the virtual source on the interface is then used to estimate the reflectivity of the interface during the imaging step. Commonly only coincident virtual sources and receivers are used to estimate reflectivity.

A major challenge here is the redatuming step because mathematical assumptions that rarely hold in reality are used to simplify the problem. A common assumption is the Born approximation which assumes that wavefield scattering is purely defined by the incident wavefield due to the source at a scatterer and not by the total wavefield, which also contains the scattered wavefields due to other scatterers. This simplification leads to incorrect reflection strength estimates when using the redatumed virtual sources and receivers.

An associated problem is the choice of the redatuming operator which can be formulated in terms of either spatial- or temporal-extrapolation operators. Depth-extrapolation operators, which are spatial-extrapolation operators, extrapolate a wavefield recorded on one depth level to another depth level. This generally does not include scattering, but transmission effects are commonly accounted for. Alternatively time-extrapolation operators can be used to estimate wavefields at retarded or advanced times. Approximate

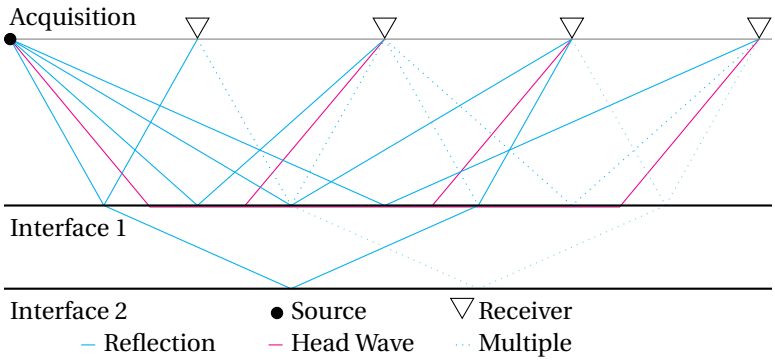

Figure 1.2: Ray diagram of single-source acoustic acquisition at the surface above two interfaces between layers with different medium properties, where at the first interface velocity increases with depth while at the second it decreases with depth.

redatuming can be achieved with these operators by back-injecting recorded wavefields into an estimated model of the medium, extrapolating the wavefield forward or backward in time and recording the resultant wavefield at a target depth level. The redatuming is approximate because the temporal-extrapolation operators tend to include scattering. In migration schemes using these operators, the source wavefield is extrapolated forward in time while the receiver wavefield is extrapolated backwards in time. For the receiver wavefield the backwards-in-time extrapolation means that the wavefield propagation is undone and that reflections collapse onto their corresponding interfaces.

For a homogeneous medium the redatumed wavefields using spatial- and temporal-extrapolation operators are identical. For inhomogeneous media they are not. The inhomogeneity results in additional non-physical events in the redatumed wavefield, constructed using temporal-extrapolation operators, which are generally considered to be artefacts. For that reason often only sufficiently smooth velocity models are considered, such that the scattering during temporal extrapolation is negligible.

In general these artefacts are not negligible. During the imaging step these artefacts can lead to errors due to the crosstalk between physical and non-physical, and non-physical and non-physical events. This problem is exasperated when using temporal-extrapolation operators as the wavefields can travel in all directions. When using spatial-extrapolation operators it is guaranteed that the extrapolated wavefield travels in the extrapolation direction. For a forward-in-depth extrapolated source wavefield that means that the wavefield is travelling downwards, while the corresponding receiver wavefield is travelling upwards. Using these two wavefields it is possible to estimate the reflectivity at a depth level. For the time-extrapolated wavefields this is hampered by the fact that both the receiver and the source wavefields can be up- and down-going. During the imaging step this can lead to crosstalk between wavefields that are both down or up going, which is indicative of transmissivity rather than reflectivity.

This problem particularly plagues Reverse Time Migration (RTM) (Hemon, 1978; Baysal et al., 1983; McMechan, 1983; Whitmore, 1983), and is expanded on in Díaz and Sava (2015). Directional wavefield decomposition can alleviate this problem as already

been noted by many, see for example Fei et al. (2010) or Liu et al. (2011). Directional wavefield decomposition at a horizontal interface allows for the separation of up- and down-going waves such that only down-going source wavefields are used in conjunction with up-going receiver wavefields to estimate the reflectivity at the interface. This does not remove all artefacts from the redatumed wavefields using time-extrapolation operators, but allows for an improvement in the estimation of reflectivity.

In this work a novel acoustic wavefield decomposition scheme is developed. Wavefield decomposition schemes already exist, see for example White (1965), Frasier (1970), Ursin (1983), Kennett (1984), Dankbaar (1985), Suprajitno and Greenhalgh (1985), and Wapenaar et al. (1990). Novel about the scheme developed in this thesis is that it separates the waves according to their propagation direction using knowledge of the wavefield everywhere in space at a given instance in time, i.e. a snapshot of a wavefield. This is in contrast to the other methods mentioned previously, which need to know the wavefield partially in space, but for all times. Our proposed scheme, as discussed in great detail in Chapter 2, is related to other common schemes in Chapter 3, is demonstrated using simple plane-wave examples in Chapter 4, and applied to imaging schemes to improve the imaging results by suppressing artefacts in Chapter 5.

Building upon the fact that the decomposition operates on snapshots of a wavefield, the decomposition direction is arbitrary. This is in stark contrast to traditional schemes (White, 1965; Frasier, 1970; Ursin, 1983; Kennett, 1984; Dankbaar, 1985; Wapenaar et al., 1990), which decompose wavefields along flat surfaces only according to the normal direction. For traditional schemes operating on wavefields recorded for all times on a horizontal surface this means that the decomposition can only result in up- and down-going wavefields. Our proposed method though can separate freely between up- and down-going, or right- and left-going, or forwards- and backwards-going wavefields. The choice of the decomposition direction is arbitrary, especially if one considers that the coordinate system can be rotated freely in space. One can even decompose an already decomposed wavefield again to find the wavefield that is for example up-and-left going.

This flexibility of snapshot decomposition allows for the decomposition of wavefields even in spatially varying directions. This enables the adaptation of the decomposition direction based on expected reflector orientations such that wavefield decomposition occurs normal to reflectors, and not simply in the vertical direction. This can result in a better estimation of reflection coefficients of reflective surfaces that are not horizontal.

As another part of this work field data were acquired and conventionally processed, as described above, along a transect in the Danube river near Novi Sad, Serbia. The idea was to explore head-wave-based imaging techniques using the expected Scholte waves in the data. These waves have a very similar behaviour to head waves but only occur at water-solid interfaces. Unfortunately Scholte waves were absent from the data. The data, however, were still suitable for conventional P-wave processing into interpretable migrated P-wave sections. These sections along with a detailed summary of the processing are presented in Appendix A.

2

ACOUSTIC DIRECTIONAL SNAPSHOT WAVEFIELD DECOMPOSITION

Acoustic Up-down wavefield decomposition is effectuated by a scaled addition or subtraction of the pressure and vertical particle velocity, generally on horizontal or vertical surfaces, and works well for data given on such surfaces. The method, however, is not applicable to decomposing a wavefield when it is given at one instance in time, i.e., on snapshots. Such situations occur when a wavefield is modelled with methods like finite-difference techniques, for the purpose of, for example, Reverse Time Migration (RTM), where the entire wavefield is determined per time instance. We present an alternative decomposition method that is exact when working on snapshots of an acoustic wavefield in a homogeneous medium, but can easily be approximated to heterogeneous media, and allows the wavefield to be decomposed in arbitrary directions. Such a directional snapshot wavefield decomposition is achieved by recasting the acoustic system in terms of the time derivative of the pressure and the vertical particle velocity, as opposed to the vertical derivative in up-down decomposition for data given on a horizontal surface. As in up-down decomposition of data given at a horizontal surface, the system can be eigenvalue decomposed and the inverse of the eigenvector matrix decomposes the wavefield snapshot into fields of opposite directions, including up-down decomposition. As the vertical particle velocity can be rotated at will, this allows for decomposition of the wavefield into any spatial direction; even spatially varying directions are possible. We show the power and efficacy of the method by synthetic examples and models of increasing complexity.

This chapter was adapted from **Holicki** et al. (2019), based on work in **Holicki** et al. (2016, 2017).

2.1. INTRODUCTION

Multicomponent acoustic directional wavefield decomposition separates acoustic wavefields according to their direction of propagation. This is useful when distinguishing between waves entering a medium from above, like surface-related multiples from above the acquisition surface, and waves leaving the medium from below, like the reflection data geophysicists are often interested in. In marine seismology, acoustic wavefield decomposition using arrays of receivers below the water surface allows for the removal of the receiver ghost, an event caused by the reflection of a recorded up-going wavefield at the sea-surface that is then recorded as a time-delayed down-going wavefield. This process is known as receiver de-ghosting (Barr and Sanders, 1989). The removed receiver ghost can then be used as an additional source wavefield in processing, see Lu et al. (2015). Wavefield decomposition is also an important tool in acoustic imaging, where it is either a pre-requisite step before being able to image the subsurface (Wapenaar et al., 1990) or directly part of the imaging condition (Díaz and Sava, 2015).

Historically, multi-component wavefield decomposition is as old as the Poynting vector (Poynting, 1884), introduced to exploration geophysics for the acoustic case by Yoon and Marfurt (2006). Acoustic decomposition began in the 1960s when White (1965) developed the data-driven particle-velocity to pressure filter matching in P-Z summation. This, however, was inexact and was followed by the development of up-down decomposition for acoustic and elastic waves along horizontal recording surfaces by the likes of Frasier (1970), Ursin (1983), Kennett (1984), Dankbaar (1985), Wapenaar et al. (1990), and Aki and Richards (2002). At the same time plane-wave up-down decomposition along a vertical array of receivers was developed by Suprajitno and Greenhalgh (1985) for homogeneous vertical seismic profiles in wells, shortly followed by parametric decomposition by Leaney and Schlumberger (1990). More recent work has focused on the use of analytic wavefields in the directional decomposition of wavefields, which only requires spatial Hilbert transforms in the direction of decomposition but comes at the cost of having to model an additional wavefield, see Shen and Albertin (2015).

Although most of the above techniques operate in the horizontal wavenumber–frequency domain for a constant depth, we propose to decompose acoustic wavefields in the full-wavenumber domain for a constant time, i.e., on snapshots of the wavefield. Since the decomposition is in the full-wavenumber domain, we call it a directional decomposition. So we directionally decompose snapshots of an acoustic wavefield as opposed to decomposing a wavefield recorded on a horizontal interface into up- and down-going fields. To achieve this we assume the components of the wavefield are known everywhere, like in modelling. As in Ursin (1983), our alternative method works by scaling a component of the particle-velocity vector to the scalar pressure, and subsequently adding or subtracting the two to effectuate the directional decomposition.

We will begin this work by discussing the scalar acoustic system for homogeneous time-invariant media in the wavenumber domain. To derive purely spatial acoustic decomposition operators we will reformulate the acoustic system in terms of two independent linear equations. The eigenvalue decomposition of this system will then yield eigenvectors that allow us to directionally decompose the system.

Next we will demonstrate that decomposition is not limited to one global decomposition direction and that the wavefield can be decomposed at arbitrary points in arbitrary

directions by rotating the decomposition operator. We will finish by illustrating these operations on models with increasing complexity. Let us begin by reviewing the fundamentals of acoustic wavefield decomposition for homogeneous time-invariant media.

2.2. ACOUSTIC DIRECTIONAL SNAPSHOT WAVEFIELD DECOMPOSITION

The three-dimensional (3D) source-free acoustic system for time-invariant homogeneous media is governed by the linearized equations of continuity and motion respectively (Wapenaar and Berkhout, 1989):

$$\partial_t p = -\rho c^2 \boldsymbol{\nabla} \cdot \boldsymbol{v}, \tag{2.1}$$

$$\partial_t \boldsymbol{v} = -\frac{1}{\rho} \boldsymbol{\nabla} p, \tag{2.2}$$

where ∂_t is the temporal derivative along time t, $p(\boldsymbol{x}, t)$ is the acoustic pressure difference to the time- and space-independent background pressure, c is the time-independent acoustic velocity, ρ is the time-independent bulk density, $\boldsymbol{\nabla}$ is the del, or nabla, operator differentiating along all spatial dimensions with spatial coordinates $\boldsymbol{x}$, $\cdot$ denotes the vector dot product and $\boldsymbol{v}(\boldsymbol{x}, t)$ is the particle velocity vector. Note that vectors are denoted using bold lower-case symbols, while matrices are upper-case and bold.

Equations 2.1 and 2.2 are written in Cartesian coordinates with no preferential direction prescribed. For the following directional decomposition of acoustic waves, a preferential direction must be chosen; in geophysics this is often the vertical. We will denote this preferential direction with a subscript z, denoting an arbitrary direction.

We will now transform Equations 2.1 and 2.2 to the 3D-wavenumber-time domain. To this end we define the 3D-wavenumber Fourier transform as the Fourier transform over all spatial dimensions of a function $f(\boldsymbol{x}, t)$ as:

$$\tilde{f}(\boldsymbol{k}, t) = \int_{\mathbb{R}^3} f(\boldsymbol{x}, t) e^{i \boldsymbol{x} \cdot \boldsymbol{k}} \mathrm{d}\boldsymbol{x} = \mathscr{F}_{\boldsymbol{x}} f(\boldsymbol{x}, t), \tag{2.3}$$

where $\boldsymbol{k}$ is the vector of wavenumbers, or Fourier parameters, corresponding to the spatial coordinates $\boldsymbol{x}$, $\mathbb{R}^3$ is the set of real 3D coordinates, and $i = \sqrt{-1}$ is the imaginary unit. $\mathscr{F}_{\boldsymbol{x}}$ denotes the forward Fourier transform operator. Note that tildes are used to denote quantities in the 3D wavenumber–time domain.

With these assumptions we transform the source-free acoustic system, Equations 2.1 and 2.2, to the wavenumber-time domain, in which the system is decomposed into spatial plane waves:

$$\partial_t \tilde{p} = \rho c^2 i \boldsymbol{k} \cdot \tilde{\boldsymbol{v}}, \tag{2.4}$$

$$\partial_t \tilde{\boldsymbol{v}} = \frac{i \boldsymbol{k}}{\rho} \tilde{p}. \tag{2.5}$$

The corresponding acoustic pressure wave equation, found by inserting Equation 2.5 into 2.4, is:

$$\partial_t^2 \tilde{p} = -c^2 \boldsymbol{k} \cdot \boldsymbol{k} \tilde{p}. \tag{2.6}$$

We now wish to decompose the wavefield into a specific direction and its opposite direction. Usually this is accomplished by writing the acoustic system in terms of the pressure and the particle velocity in the direction of decomposition, the z direction. To express Equation 2.4 in terms of $\tilde{v}_z$ we back substitute $\tilde{v}_z$ from Equation 2.5 into Equation 2.6 and integrate over time for a zero constant of integration:

$$\partial_t \tilde{p} = \rho c^2 \frac{\boldsymbol{k}\cdot\boldsymbol{k}}{-ik_z}\tilde{v}_z \quad \text{for } k_z \neq 0. \tag{2.7}$$

Note that in this paper we do not use Einstein's summation convention for repeated subscripts.

Equation 2.7 only holds for $k_z \neq 0$; for $k_z = 0$ waves are travelling orthogonally to the z direction and are not accounted for in $\tilde{v}_z$. To resolve this undefined behaviour for $k_z = 0$ we have two options. We can zero the fraction for $k_z = 0$, which implicitly assumes the absence of waves travelling orthogonally to the z direction as all $\boldsymbol{k}$ are assumed to be zero for all $k_z = 0$, which is generally not the case. Alternatively, we can express the fraction for $k_z = 0$ in terms of orthogonal wavenumber components. For the moment we assume the former, however, in Section 2.2.3 we will discuss how to include orthogonal wavenumber components.

We can now combine Equation 2.7 with Equation 2.5 to find the following system in terms of $\tilde{p}$ and $\tilde{v}_z$:

$$\partial_t \begin{pmatrix} \tilde{p} \\ \tilde{v}_z \end{pmatrix} = \begin{pmatrix} 0 & \rho c^2 \frac{\boldsymbol{k}\cdot\boldsymbol{k}}{-ik_z} \\ \frac{ik_z}{\rho} & 0 \end{pmatrix} \begin{pmatrix} \tilde{p} \\ \tilde{v}_z \end{pmatrix}. \tag{2.8}$$

In matrix-vector notation we can write this as:

$$\partial_t \tilde{\boldsymbol{q}}_z = \tilde{\boldsymbol{A}}_z \tilde{\boldsymbol{q}}_z, \tag{2.9}$$

where:

$$\tilde{\boldsymbol{q}}_z = \begin{pmatrix} \tilde{p} \\ \tilde{v}_z \end{pmatrix}, \tag{2.10}$$

$$\tilde{\boldsymbol{A}}_z = \begin{pmatrix} 0 & \rho c^2 \frac{\boldsymbol{k}\cdot\boldsymbol{k}}{-ik_z} \\ \frac{ik_z}{\rho} & 0 \end{pmatrix}, \tag{2.11}$$

where the subscripts indicate to which particle velocity component $\tilde{\boldsymbol{q}}$ and $\tilde{\boldsymbol{A}}$ are related to.

Equation 2.9 represents a different starting point for directional decomposition than conventional up-down decomposition, see Ursin (1983) for example. In conventional decomposition the system is written with $\partial_z \boldsymbol{q}_z$ on the left-hand side, whereas here we have $\partial_t \boldsymbol{q}_z$.

2.2.1. EIGENVALUE DECOMPOSITION

Decomposing $\tilde{\boldsymbol{A}}$ into an eigenvalue matrix $\tilde{\boldsymbol{\Lambda}}$ and eigenvector matrix $\tilde{\boldsymbol{L}}$ we have:

$$\partial_t \tilde{\boldsymbol{q}}_z = \tilde{\boldsymbol{L}}\tilde{\boldsymbol{\Lambda}}\tilde{\boldsymbol{L}}^{-1}\tilde{\boldsymbol{q}}_z, \tag{2.12}$$

where we have for a judicial choice of the z direction as the principal direction and pressure normalization of the eigenvectors:

$$\tilde{\boldsymbol{\Lambda}}_z = ci\ \mathrm{sgn}(k_z)|\boldsymbol{k}| \begin{pmatrix} 1 & 0 \\ 0 & -1 \end{pmatrix}, \tag{2.13}$$

$$\tilde{\boldsymbol{L}}_{p,z} = \begin{pmatrix} 1 & 1 \\ \frac{1}{\rho c}\frac{|k_z|}{|\boldsymbol{k}|} & -\frac{1}{\rho c}\frac{|k_z|}{|\boldsymbol{k}|} \end{pmatrix}. \tag{2.14}$$

where sgn() is the signum function corresponding to a quantity divided by its magnitude $||$. Note that the subscript z indicates that the signs of the eigenvalues were chosen according to the sign of k_z. The subscript p is used to denote pressure-normalized eigenvectors, as opposed to the particle-velocity normalized eigenvectors which are shown later in Section 2.2.4.

We now define the decomposed fields $\tilde{\boldsymbol{d}}$ as the result of a general eigenvector matrix inverse $\tilde{\boldsymbol{L}}^{-1}$ acting on $\tilde{\boldsymbol{q}}$:

$$\tilde{\boldsymbol{d}} = \tilde{\boldsymbol{L}}^{-1}\tilde{\boldsymbol{q}}, \tag{2.15}$$

where for the pressure-normalized z-direction case:

$$\tilde{\boldsymbol{L}}^{-1}_{p,z} = \frac{1}{2}\begin{pmatrix} 1 & \rho c\frac{|\boldsymbol{k}|}{|k_z|} \\ 1 & -\rho c\frac{|\boldsymbol{k}|}{|k_z|} \end{pmatrix}. \tag{2.16}$$

Rearranging Equation 2.12 with the help of Equation 2.15 and the assumption that the medium parameters are time invariant we find:

$$\partial_t \tilde{\boldsymbol{d}} = \tilde{\boldsymbol{\Lambda}}\tilde{\boldsymbol{d}}. \tag{2.17}$$

We have now decomposed the acoustic wave equation into two first-order-in-time independent equations. Note that in Equation 2.17 we have not specified a direction or normalization.

To better understand Equation 2.17 let us look at its components in more detail for the case of choosing the signs according to the z direction. We can rewrite Equation 2.13 as the following by expressing $|\boldsymbol{k}|$ in terms of $|k_z|$ and the acute angle $\tilde{\theta}_z$ between them:

$$\tilde{\boldsymbol{\Lambda}}_z = ik_z\frac{c}{\cos(\tilde{\theta}_z)}\begin{pmatrix} 1 & 0 \\ 0 & -1 \end{pmatrix}, \tag{2.18}$$

where:

$$i\ \mathrm{sgn}(k_z)|\boldsymbol{k}| = \frac{ik_z}{\cos(\tilde{\theta}_z)}, \tag{2.19}$$

and:

$$\tilde{\theta}_z = \mathrm{arctan3}(k_x, |k_z|) \quad \text{where } -\frac{\pi}{2} < \tilde{\theta}_z \leq \frac{\pi}{2}. \tag{2.20}$$

We define arctan3(), which is similar to the common arctan2() variant, to be the following variant of the arctangent:

$$\operatorname{arctan3}(x,z) = \begin{cases} \arctan(\frac{x}{z}) & \text{if } z > 0, \\ \arctan(\frac{x}{z}) + \pi & \text{if } z < 0 \text{ and } x \geq 0, \\ \arctan(\frac{x}{z}) - \pi & \text{if } z < 0 \text{ and } x < 0, \\ +\frac{\pi}{2} & \text{if } z = 0 \text{ and } x \neq 0, \\ \text{undefined} & \text{if } z = 0 \text{ and } x = 0. \end{cases} \tag{2.21}$$

Again care must be taken for waves travelling in the orthogonal directions, as for these $\cos(\tilde{\theta}_i) = 0$ or undefined at the origin in the wavenumber domain, where the pressure and particle velocity must be zero. The pressure p must be zero since we assumed that it is measured with respect to the homogeneous time-invariant background pressure and the particle velocity must be zero such that the system as a whole is at rest, as this was assumed when deriving the acoustic wave equation (Aki and Richards, 2002). We again zero the operation, like for Equation 2.7, for $k_z = 0$.

Based on Equation 2.18, $\tilde{\boldsymbol{\Lambda}}$ corresponds to a modified derivative in the space domain in the z direction, due to the ik_z, however via Equation 2.17 the action of $\tilde{\boldsymbol{\Lambda}}$ is also equivalent to the time derivative. $\tilde{\boldsymbol{\Lambda}}$ evidently expresses the time derivative in terms of spatial derivatives.

With the judicious choice of normalization for $\tilde{\boldsymbol{L}}_{p,z}$ in Equation 2.16, the decomposed fields $\tilde{\boldsymbol{d}}_{p,z}$, Equation 2.15, can be interpreted as pressure wavefields:

$$\tilde{\boldsymbol{d}}_{p,z} = \begin{pmatrix} \tilde{p}_z^+ \\ \tilde{p}_z^- \end{pmatrix} = \frac{1}{2} \begin{pmatrix} 1 & \rho c \frac{|\boldsymbol{k}|}{|k_z|} \\ 1 & -\rho c \frac{|\boldsymbol{k}|}{|k_z|} \end{pmatrix} \begin{pmatrix} \tilde{p} \\ \tilde{v}_z \end{pmatrix}. \tag{2.22}$$

Because the pressure-normalized form of the eigenvectors is used we denote the decomposed fields in terms of the pressure wavefields p_z^+ and p_z^-. We can further express Equation 2.22 in terms of $\tilde{\theta}_i$ via Equation 2.19 as:

$$\begin{pmatrix} \tilde{p}_z^+ \\ \tilde{p}_z^- \end{pmatrix} = \frac{1}{2} \begin{pmatrix} 1 & \frac{\rho c}{\cos(\tilde{\theta}_z)} \\ 1 & -\frac{\rho c}{\cos(\tilde{\theta}_z)} \end{pmatrix} \begin{pmatrix} \tilde{p} \\ \tilde{v}_z \end{pmatrix}. \tag{2.23}$$

To better understand Equation 2.23 consider Figure 2.1, which shows how the scale factor of the decomposition depends on the angle $\tilde{\theta}$. For waves travelling at small angles to the z direction the scale factor is dominated by the local specific acoustic impedance, however as the wave begins to travel more and more obliquely to the z direction the scale factor grows asymptotically to infinity.

This asymptotic behaviour is due to the fact that we chose to approximate the acoustic system in terms of one component of the particle velocity. We can however recast the system in a more stable form that accounts for the asymptotic scaling by writing the system in terms of the magnitude of the full particle-velocity vector.

2.2.2. FORMULATION IN TERMS OF THE FULL PARTICLE-VELOCITY VECTOR

The asymptotic behaviour and the associated singularities in Figure 2.1 are due to the fraction in Equation 2.22. We now wish to write the action of the wavenumber fraction on

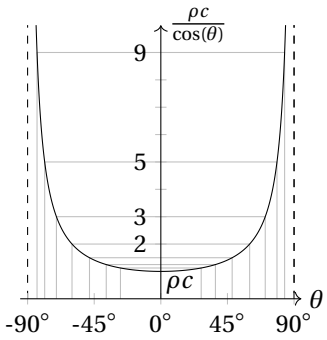

Figure 2.1: Acoustic wavefield decomposition scale factor for the z component of the particle velocity to the pressure with respect to the angle the corresponding plane wave makes with the z direction. To aid the reader the scale factors of 1.125, 1.25, 1.5, 2, 3, 5 and 9 times the specific acoustic impedance ρc are indicated in grey.

$\tilde{v}_z$ in terms of the magnitude of the particle-velocity vector. To do so we write the scaled z component of the particle velocity in Equation 2.22 in terms of its sign and absolute value:

$$\frac{|\boldsymbol{k}|}{|k_z|}\tilde{v}_z = \mathrm{sgn}(\tilde{v}_z)\left|\frac{\boldsymbol{k}}{k_z}\tilde{v}_z\right|. \tag{2.24}$$

Note that the signum of a complex quantity is that quantity divided by its magnitude. To interpret the magnitude term we return to the linearized equation of motion, Equation 2.5, and solve for the pressure in terms of the j^{th} and k^{th} components of the particle velocity:

$$\tilde{p} = \frac{\rho}{i\,k_j}\partial_t\tilde{v}_j = \frac{\rho}{i\,k_k}\partial_t\tilde{v}_k \quad \text{for } k_j \neq 0 \text{ and } k_k \neq 0. \tag{2.25}$$

Note that the second term in Equation 2.25 is not valid for $k_j = 0$, while the last term is not valid for $k_k = 0$. Evidently different particle-velocity components, which are not necessarily orthogonal, can account for wavenumber components that another component cannot account for and vice versa.

We can use Equation 2.25 to write the particle-velocity vector in terms of the z component:

$$\tilde{\boldsymbol{v}} = \frac{\boldsymbol{k}}{k_z}\tilde{v}_z \quad \text{for } k_z \neq 0. \tag{2.26}$$

Based on the above it becomes evident that the magnitude term in Equation 2.24 corresponds to the magnitude of the particle velocity vector:

$$\frac{|\boldsymbol{k}|}{|k_z|}\tilde{v}_z = \mathrm{sgn}(\tilde{v}_z)|\tilde{\boldsymbol{v}}|. \tag{2.27}$$

With this equation we can remove the asymptotic behaviour from Equation 2.22 by writing it in terms of the magnitude of the particle velocity:

$$\begin{pmatrix}\tilde{p}_z^+\\ \tilde{p}_z^-\end{pmatrix} = \frac{1}{2}\begin{pmatrix}1 & \rho c\\ 1 & -\rho c\end{pmatrix}\begin{pmatrix}\tilde{p}\\ \mathrm{sgn}(\tilde{v}_z)|\tilde{\boldsymbol{v}}|\end{pmatrix}. \tag{2.28}$$

Equation 2.28 now does not show any singular behaviour and is unconditionally stable.

2.2.3. ACCOUNTING FOR $k_z = 0$

Recall that for Equation 2.7 we chose to zero the operator for $k_z = 0$. This implicitly excludes the part of the wavefield where $k_z = 0$ but $\boldsymbol{k} \neq \mathbf{0}$, where $\mathbf{0}$ is the null vector. The consequence of this is that the eigenvalue decomposition does not hold for $k_z = 0$, because our sign choice for the eigenvalues is incomplete. Furthermore the elements in the second column of the matrix in Equation 2.16 are zero, causing wavefields travelling orthogonally to the z direction to be equally split between the decomposed fields for $k_z = 0$. This remains a problem in Equation 2.28 as $\tilde{v}_z = 0$ where $k_z = 0$. We will now correct for this by including the absent orthogonal information in Equation 2.7.

To introduce the orthogonal wavefield information into Equation 2.7, we recall from Equation 2.25 that although no individual component of the particle velocity can properly account for the total pressure field, an orthogonal set of particle-velocity components can. Noting that the equation of motion, Equation 2.5, dictates that any component of the particle velocity is zero where its corresponding wavenumber is zero, we now seek an equivalent to the z component of the particle velocity that where $k_z = 0$ is equal to the other components of the particle velocity.

To do so we must make a choice on how to order the dimensions. We introduce a generalized particle velocity $\tilde{v}_z$ that is equal to $\tilde{v}_z$ everywhere where $k_z \neq 0$. When $k_z = 0$ $\tilde{v}_z$ is equal to the first orthogonal component $\tilde{v}_x$ as long as $k_x \neq 0$, at which point $\tilde{v}_z$ is equal to $\tilde{v}_y$. At the origin in the wavenumber domain the generalized particle velocity is zero as each component of the particle velocity at the origin must be zero such that the acoustic system as a whole is at rest. The choice of how to order the particle velocity components where $k_z = 0$ is important because it defines how orthogonally travelling waves are mapped into the decomposed fields. Note that we should indicate either in the subscript or superscript of $\tilde{v}_z$ how the dimensions are ordered; we will assume that the ordering is always chosen using the same system and hence will not indicate the order of dimensions.

We now define the generalized particle velocity $\tilde{v}_z$ in three orthogonal dimensions (x, y, z) as:

$$\tilde{v}_z = \begin{cases} \tilde{v}_z & \text{if } k_z \neq 0, \\ \tilde{v}_x & \text{if } k_x \neq 0 \;\&\; k_z = 0, \\ \tilde{v}_y & \text{if } k_y \neq 0 \;\&\; k_z = k_x = 0, \\ 0 & \text{if } \boldsymbol{k} = \mathbf{0}. \end{cases} \tag{2.29}$$

The wavenumber κ_z associated with this generalized particle velocity that accounts for the orthogonal components we define as:

$$\kappa_z = \begin{cases} k_z & \text{if } k_z \neq 0 \\ k_x & \text{if } k_x \neq 0 \;\&\; k_z = 0, \\ k_y & \text{if } k_y \neq 0 \;\&\; k_z = k_x = 0, \\ 0 & \text{if } \boldsymbol{k} = \mathbf{0}. \end{cases} \tag{2.30}$$

Note that division by κ_z is still poorly defined at the origin in the wavenumber domain. When either the pressure or a particle-velocity component is divided by κ_z the result at the origin is assumed to be zero. This comes from our definition of the pressure being

measured with respect to the time- and space-invariant background pressure. The particle velocity on the other hand must be zero at the origin in the wavenumber domain such that the acoustic system is globally at rest and not travelling as a whole in some direction, which would invalidate the original derivation of the acoustic system.

We can now, analogously to Equation 2.26, fully express any particle-velocity component in terms of this generalized particle velocity $\tilde{v}_z$ and its associated wavenumber κ_z via:

$$\tilde{\boldsymbol{v}} = \frac{\boldsymbol{k}}{\kappa_z}\tilde{v}_z. \tag{2.31}$$

In order to find the acoustic system in terms of the generalized particle velocity $\tilde{v}_z$ we insert Equation 2.31 into Equations 2.4 and 2.5:

$$\partial_t \tilde{p} = \rho c^2 \frac{\boldsymbol{k}\cdot\boldsymbol{k}}{-i\kappa_z}\tilde{v}_z, \tag{2.32}$$

$$\partial_t \tilde{v}_z = \frac{i\kappa_z}{\rho}\tilde{p}. \tag{2.33}$$

Note that Equation 2.32 is now well defined everywhere.

From here the derivation of wavefield decomposition is identical to the earlier derivation in terms of $\tilde{v}_z$ and will not be repeated here. The only difference is that we replace $\tilde{v}_z$ with $\tilde{v}_z$ and k_z with κ_z.

In terms of the generalized particle-velocity vector, the pressure-normalized decomposition, Equation 2.22, reads:

$$\begin{pmatrix}\tilde{p}_z^+\\ \tilde{p}_z^-\end{pmatrix} = \frac{1}{2}\begin{pmatrix}1 & \rho c\frac{|\boldsymbol{k}|}{|\kappa_z|}\\ 1 & -\rho c\frac{|\boldsymbol{k}|}{|\kappa_z|}\end{pmatrix}\begin{pmatrix}\tilde{p}\\ \tilde{v}_z\end{pmatrix}. \tag{2.34}$$

The decomposition operator is now no longer undefined where $k_z = 0$.

We can remove the wavenumber scaling from Equation 2.34 by writing it in terms of the magnitude of the particle-velocity vector:

$$\begin{pmatrix}\tilde{p}_z^+\\ \tilde{p}_z^-\end{pmatrix} = \frac{1}{2}\begin{pmatrix}1 & \rho c\\ 1 & -\rho c\end{pmatrix}\begin{pmatrix}\tilde{p}\\ \operatorname{sgn}(\tilde{v}_z)|\tilde{\boldsymbol{v}}|\end{pmatrix}. \tag{2.35}$$

This form of the decomposition is unconditionally stable and fully satisfies Equation 2.17 with the eigenvalue matrix from Equation 2.13, but now in terms of κ_z, where the eigenvalues additionally account for orthogonally travelling waves.

The only major difference between decomposition in terms of $\tilde{v}_z$ and $\tilde{v}_z$ is how orthogonally travelling waves are decomposed, which occur where $k_z = 0$. These are decomposed according to the orthogonal directions. This means that if z corresponds to the vertical direction, then the orthogonally travelling waves are for example left-right decomposed, instead of being neglected and equally split up between the decomposed fields, as occurs in the previous derivation, see Figure 2.2.

This warrants a new nomenclature for the decomposition operators as the notion of up-down decomposition is inherently non-unique for $k_z = 0$. We choose to speak of (up-left)-(down-right) decomposition as opposed to simple up-down decomposition. In (up-left)-(down-right) decomposition we would map the purely left-going waves to the "up-going" decomposed field, while purely right going waves get mapped to the "down-going" field, or vice versa for (up-right)-(down-left) decomposition.

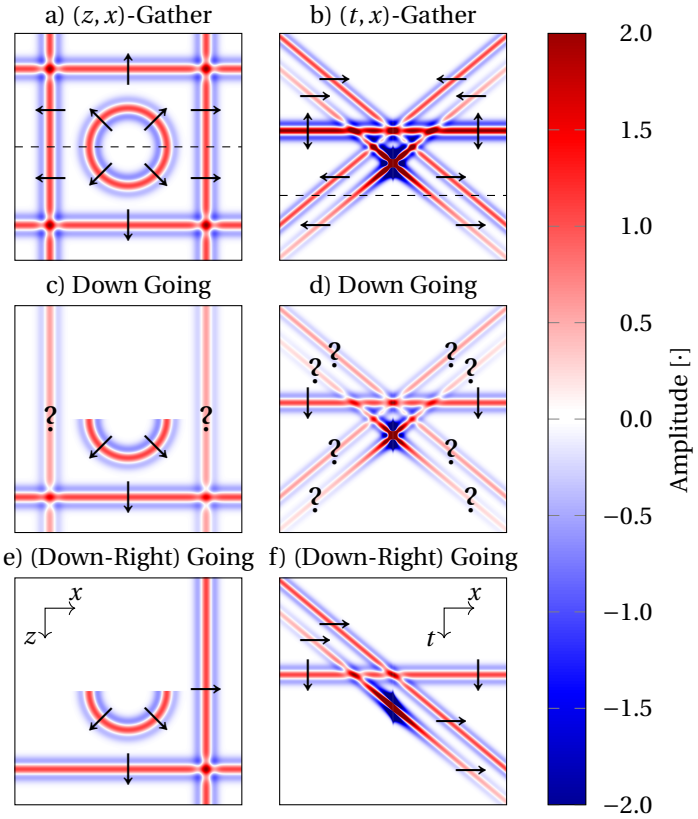

Figure 2.2: a) (z,x) and (b) (t,x) gathers of a three-dimensional wavefield, for $t = 0$ and $z = 0$ respectively. Arrows indicate local propagation direction, and the dashed lines indicate their intersection. c) and (d) are (a) and (b) up-down decomposed without properly taking into account horizontally travelling waves. e) and (f) are properly (up-left)-(down-right) decomposed versions of (a) and (b). Note how the horizontally travelling plane waves are both included with half amplitude in (c) and (d) and have unknown propagation directions, indicated by ?s. In (e) and (f), however, only the right-going plane wave is included and has a known propagation direction. Note that data at the spatial origin have been muted and that the coordinate system displayed in (e) applies to (a, c, and e) and the coordinate system in (f) applies to (b, d, and f).

2.2.4. PARTICLE-VELOCITY-NORMALIZED DECOMPOSITION

When we applied eigenvalue decomposition to Equation 2.9 in Section 2.2.1 we chose to normalize the eigenvectors such that the inverse of the eigenvector matrix scaled the particle velocity to the pressure, hence the name pressure-normalized decomposition. It is also possible to choose the eigenvectors such that the pressure is scaled to the particle velocity. The resulting decomposition is known as the particle-velocity-normalized decomposition:

$$\tilde{\boldsymbol{d}}_{v,z} = \begin{pmatrix} \tilde{v}_z^+ \\ \tilde{v}_z^- \end{pmatrix} = \frac{1}{2} \begin{pmatrix} \frac{1}{\rho c} \frac{|k_z|}{|\boldsymbol{k}|} & 1 \\ -\frac{1}{\rho c} \frac{|k_z|}{|\boldsymbol{k}|} & 1 \end{pmatrix} \begin{pmatrix} \tilde{p} \\ \tilde{v}_z \end{pmatrix}. \tag{2.36}$$

Note that Equation 2.36 in conjunction with Equation 2.22 implicitly means that we can change between pressure- and particle-velocity-normalized decomposed wavefields:

$$\begin{pmatrix}\tilde{v}_z^+\\ \tilde{v}_z^-\end{pmatrix} = \frac{|\kappa_z|}{\rho c|\boldsymbol{k}|}\begin{pmatrix}1 & 0\\ 0 & -1\end{pmatrix}\begin{pmatrix}\tilde{p}_z^+\\ \tilde{p}_z^-\end{pmatrix}. \tag{2.37}$$

These normalizations play an important role later in Figure 2.7, where they are indirectly used to decompose already decomposed fields along another direction.

2.2.5. ROTATING THE DECOMPOSITION DIRECTION

So far decomposition only occurred along the arbitrary z direction, along which the particle velocity was also recorded. We now wish to decompose the wavefield in some other direction defined by the angle vector $\boldsymbol{\phi}'$ with respect to the z direction. We have two options to achieve this: (1) We rotate the coordinate system such that the z direction points in the desired direction, which means that we also rotate the particle-velocity vector, and apply the same decomposition operator again, but in the new coordinate system. Or, (2) we can rotate the decomposition operator to decompose in the desired direction.

For the first option we need to rotate the wavefield vector $\tilde{\boldsymbol{q}}_z$, with generalized particle velocity component v_z, to point in the rotated z' direction. We recall that Equation 2.25 allowed us to express not necessarily orthogonal components of the particle velocity in terms of each other. We can also use it to rotate the generalized particle velocity as follows:

$$\tilde{v}_{z'} = \frac{\kappa_{z'}}{\kappa_z}\tilde{v}_z, \tag{2.38}$$

where we chose to rotate $\boldsymbol{k}$ by ϕ' to find $k_{z'}$ and the associated $\kappa_{z'}$. Rotating $\tilde{\boldsymbol{q}}_z$ to $\tilde{\boldsymbol{q}}_{z'}$ then is:

$$\tilde{\boldsymbol{q}}_{z'} = \begin{pmatrix}\tilde{p}\\ \tilde{v}_{z'}\end{pmatrix} = \begin{pmatrix}1 & 0\\ 0 & \frac{\kappa_{z'}}{\kappa_z}\end{pmatrix}\begin{pmatrix}\tilde{p}\\ \tilde{v}_{z'}\end{pmatrix} = \tilde{\boldsymbol{R}}\tilde{\boldsymbol{q}}_z. \tag{2.39}$$

Note that if Equation 2.39 is transformed back to the space domain it simply corresponds to only rotating the particle-velocity vector, leaving the pressure untouched as it is direction independent.

When we decompose the acoustic system again using the new coordinate system and sign the magnitude of the particle-velocity vector according to $\kappa_{z'}$ instead of κ_z then we decompose along the z' direction. Mathematically we write the decomposition, analogously to Equation 2.15, in the rotated coordinate system as:

$$\tilde{\boldsymbol{d}}_{z'} = \tilde{\boldsymbol{L}}_{z'}^{-1}\tilde{\boldsymbol{q}}_{z'}. \tag{2.40}$$

To rotate the decomposition operator instead of the particle velocity we back substitute Equation 2.39 into 2.40 to find:

$$\tilde{\boldsymbol{d}}_{z'} = \tilde{\boldsymbol{L}}_{z'}^{-1}\tilde{\boldsymbol{R}}\tilde{\boldsymbol{q}}_z. \tag{2.41}$$

We can now include the rotation operator into the decomposition operator to find the rotated decomposition operator, which is a function of the angle vector $\boldsymbol{\phi}$ as it works for

any angle. For the pressure normalized case, Equation 2.16, it would be:

$$\tilde{\boldsymbol{L}}^{-1}_{p,z}(\boldsymbol{\phi}) = \tilde{\boldsymbol{L}}^{-1}_{p,z'}\tilde{\boldsymbol{R}} = \frac{1}{2}\begin{pmatrix} 1 & \rho c \frac{\operatorname{sgn}(\kappa(\boldsymbol{\phi}))|\boldsymbol{k}|}{\operatorname{sgn}(\kappa_z)|\kappa_z|} \\ 1 & -\rho c \frac{\operatorname{sgn}(\kappa(\boldsymbol{\phi}))|\boldsymbol{k}|}{\operatorname{sgn}(\kappa_z)|\kappa_z|} \end{pmatrix}, \tag{2.42}$$

where $\kappa(\boldsymbol{\phi})$ is the rotated κ_z in the new coordinate system. We have now rotated the decomposition operator such that it uses a particle-velocity component pointing in one direction but directionally decomposes the wavefield along another.

Equation 2.42 also demonstrates that the decomposition direction is purely determined by the sign choice for $|\boldsymbol{k}|$, and not by the chosen particle-velocity component, which is accounted for in the denominators.

We can also use Equation 2.42 to make the a priori choice of the decomposition direction a posterior choice by extending the dimensionality of the operator output to additionally depend on the decomposition direction:

$$\tilde{\boldsymbol{d}}(\boldsymbol{k}, t, \boldsymbol{\phi}) = \tilde{\boldsymbol{L}}^{-1}_{z}(\boldsymbol{k}, \boldsymbol{\phi})\tilde{\boldsymbol{q}}_z(\boldsymbol{k}, t). \tag{2.43}$$

Now the decomposed wavefields $\tilde{\boldsymbol{d}}$ are decomposed along all possible directions. We effectively treat the inherent directional ambiguity of the decomposition in terms of additional dimensions and at the cost of associated work. Note that this does not fully treat the ambiguity in sign choice for $|\kappa_z|$ as we only deal with the subset of sign choices that leads to directionally decomposed wavefields. Furthermore for each $\boldsymbol{\phi}$ the decomposition is still a global operation in space. In the next section we discuss spatially varying decomposition directions.

2.2.6. SPATIALLY VARYING DECOMPOSITION DIRECTIONS

To have spatially varying decomposition directions we need to transform the decomposition back to the space domain and then choose a different decomposition direction at each point in the space domain. Note that this also means that the decomposition direction can change in time.

This is trivial with Equation 2.43. One can transform the decomposed results back to the space domain and then choose a different decomposition direction for every point in space and time. Mathematically this corresponds to extracting a $\boldsymbol{\phi} = \boldsymbol{\phi}'(\boldsymbol{x}, t)$ surface from the decomposed result of Equation 2.43 in the space domain.

Taking things step by step we first need to transform Equation 2.43 back to the space domain:

$$\boldsymbol{d}(\boldsymbol{x}, t, \boldsymbol{\phi}) = \mathscr{F}^{-1}_{\boldsymbol{x}}\tilde{\boldsymbol{L}}^{-1}_{z}(\boldsymbol{k}, \boldsymbol{\phi})\mathscr{F}_{\boldsymbol{x}}\boldsymbol{q}_z(\boldsymbol{x}, t). \tag{2.44}$$

To be able to extract a $\boldsymbol{\phi}'$ surface from Equation 2.44 we need to make the decomposition direction a function of space and time. A simple static-in-time 2D directional surface could be the radial direction away from some point, the origin for simplicity:

$$\phi'(x, z) = \operatorname{arctan2}(x, z), \tag{2.45}$$

where arctan2 is the following variant of the arctangent:

$$\operatorname{arctan2}(x,z) = \begin{cases} \arctan(\frac{x}{z}) & \text{if } z > 0, \\ \arctan(\frac{x}{z}) + \pi & \text{if } z < 0 \text{ and } x \geq 0, \\ \arctan(\frac{x}{z}) - \pi & \text{if } z < 0 \text{ and } x < 0, \\ +\frac{\pi}{2} & \text{if } z = 0 \text{ and } x > 0, \\ -\frac{\pi}{2} & \text{if } z = 0 \text{ and } x < 0, \\ \text{undefined} & \text{if } z = 0 \text{ and } x = 0. \end{cases} \tag{2.46}$$

Note that at the wavenumber-domain origin, where ϕ' is undefined, we are free to define ϕ' to point in any direction, for example the z direction.

Note that any other conceivable, not necessarily smooth, surface is also acceptable. This particular choice of directional surface is of interest though, because it decomposes wavefields into a wavefield collapsing towards a point and a wavefield expanding away from said point. If we now extract this surface from Equation 2.44 we find:

$$\boldsymbol{d}_{\phi'}(\boldsymbol{x}, t) = \boldsymbol{d}(\boldsymbol{x}, t, \phi'(x, t)). \tag{2.47}$$

Note that depending on how orthogonal directions are treated in the decomposition, waves travelling at a given point tangential to the clockwise direction around the centre belong to the outward-going wavefield, while waves travelling counter-clockwise belong to the inward-going wavefield. Notice that we no longer speak of down- and up-going waves; we now have to speak of waves going inwards and waves going outwards due to our choice of decomposition direction.

This example is demonstrated in Figure 2.3, in which an expanding and a collapsing wavefield (Figure 2.3a) are separated by decomposing the wavefield into a wavefield travelling towards the centre and one travelling away from it (Figure 2.3c). To aid in the visual inspection of the decomposition, the impedance-scaled particle velocity $\rho c v_{\phi'}$, measured in the directions defined by ϕ', is also included in Figure 2.3b. The associated desired decomposition angles are shown in Figure 2.3d.

The workflow for decomposing snapshots of an acoustic wavefield using spatially and possibly temporally varying wavefields is illustrated in Figure 2.4. The basic idea is to decompose snapshots of a wavefield everywhere in space for all desired decomposition directions, and then from the result to extract the desired decomposed fields in space and time. Note that extraction in other domains, like the wavenumber and/or frequency domains, may be fruitful, although the results may no longer be perfectly directionally decomposed.

2.2.7. APPROXIMATION FOR LOCALLY HOMOGENEOUS MEDIA

Now that we have derived the decomposition for globally homogeneous media we extend it, in an approximate sense, to locally homogeneous media. To do this we apply the wavenumber scaling of the decomposition in the wavenumber domain and multiply with the local specific acoustic impedance in the space domain. We achieve this by transforming the decomposition operator in Equation 2.34 back to the space domain. As the medium parameters are assumed to be globally homogeneous we can pull the

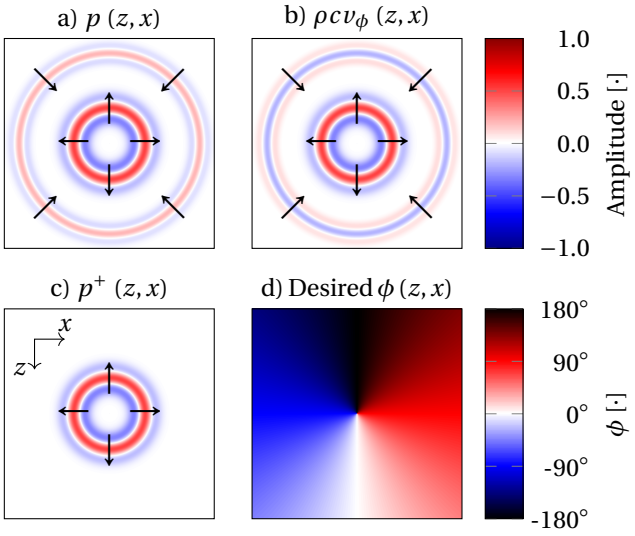

Figure 2.3: Directional decomposition of a pressure snapshot (a), consisting of an expanding wavefield (inner circle) and a collapsing wavefield (outer circle), by scaling the radial particle velocity (b) to (a), according to the desired decomposition direction (d), and adding the two to find the expanding pressure wavefield (c). Note that at the centre the wavefields were (up-left)-(down-right) decomposed and that the coordinate system displayed in (c) applies to all panels.

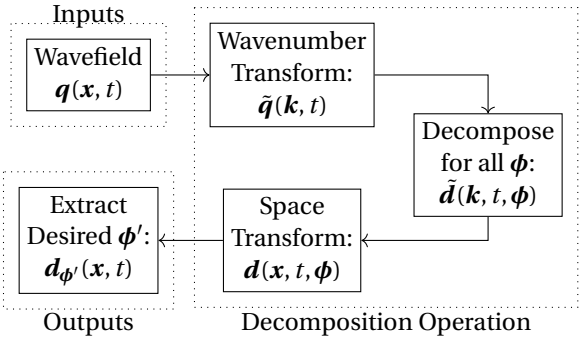

Figure 2.4: Concept behind having locally different decomposition directions.

Fourier transforms into the decomposition operator, Equation 2.34, where they cancel for the first column and sandwich the wavenumber fraction in the second:

$$\boldsymbol{L}_{p,z} = \frac{1}{2}\begin{pmatrix} 1 & \rho c \mathscr{F}_{\boldsymbol{x}}^{-1} \frac{|\boldsymbol{k}|}{|\kappa_z|} \mathscr{F}_{\boldsymbol{x}} \\ 1 & -\rho c \mathscr{F}_{\boldsymbol{x}}^{-1} \frac{|\boldsymbol{k}|}{|\kappa_z|} \mathscr{F}_{\boldsymbol{x}} \end{pmatrix}. \tag{2.48}$$

We can now let $\rho c = \rho(\boldsymbol{x})c(\boldsymbol{x})$ vary spatially in an approximation to decomposition in heterogeneous media. The decomposition is then as follows:

$$\begin{pmatrix} p_z^+ \\ p_z^- \end{pmatrix} = \frac{1}{2}\begin{pmatrix} 1 & \rho(\boldsymbol{x})c(\boldsymbol{x})\mathscr{F}_{\boldsymbol{x}}^{-1}\frac{|\boldsymbol{k}|}{|\kappa_z|}\mathscr{F}_{\boldsymbol{x}} \\ 1 & -\rho(\boldsymbol{x})c(\boldsymbol{x})\mathscr{F}_{\boldsymbol{x}}^{-1}\frac{|\boldsymbol{k}|}{|\kappa_z|}\mathscr{F}_{\boldsymbol{x}} \end{pmatrix}\begin{pmatrix} p \\ v_z \end{pmatrix}. \tag{2.49}$$

This approximation seems to be a relatively accurate decomposition that mimics plane-wave decomposition for heterogeneous media, as will be shown using synthetic examples later. It, however, does not take scattering properly into account, nevertheless it works very well for locally homogeneous media as we will demonstrate using synthetic examples in Section 2.4.

2.2.8. STEERING THE DECOMPOSITION DIRECTION ACCORDING TO THE MEDIUM

Allowing medium parameters to vary locally suggests that the decomposition direction could, in conjunction with Section 2.2.6, be tied to medium parameter variations. This for example would allow the decomposition direction to be normal to medium interfaces. This has ramifications for many acoustic processing techniques like imaging.

Given a snapshot of a wavefield in a known medium and Section 2.2.6, it is now possible to steer the decomposition direction based on local medium-parameter gradients at a point to ensure that the decomposition direction is always parallel to variations in medium parameters. To do so one computes the gradients of the acoustic velocity and the density, from which one derives two normalized direction maps by dividing by the magnitude of the respective gradients. These direction maps can then be used to steer the decomposition, however, the direction based on these two maps may be multivalued as the gradients in the bulk density and medium velocity are not necessarily aligned. This can approximately be accounted for by calculating specific-acoustic-impedance-based directions as follows:

$$\boldsymbol{n} = \frac{\boldsymbol{\nabla}\rho c}{|\boldsymbol{\nabla}\rho c|}, \tag{2.50}$$

where the vector $\boldsymbol{n}$ is the normalized local specific-acoustic-impedance-based direction that can be expressed in terms of angles. Note that the decomposition direction is ill-defined where the gradient is zero. In this case the decomposition direction must be explicitly chosen.

Let us illustrate the concept with an example. Figure 2.5a shows the constant-density Marmousi velocity model (Brougois et al., 1990), and below it a smoothed version to avoid discontinuous decomposition directions (Figure 2.5b), based on which ideal decomposition directions may be readily computed (Figure 2.5c). Note that wherever the gradient was zero the decomposition direction was chosen to point downwards. The vector field in Figure 2.5b shows coarsely the decomposition directions in Figure 2.5c, demonstrating that they are quasi-normal to velocity interfaces.

By tying the decomposition direction to local variations in medium parameters we can now approximately ensure that wavefields are decomposed into in- and out-going wavefields at interfaces. This can improve acoustic processing techniques, like imaging, by ensuring that decomposition is always normal to medium interfaces.

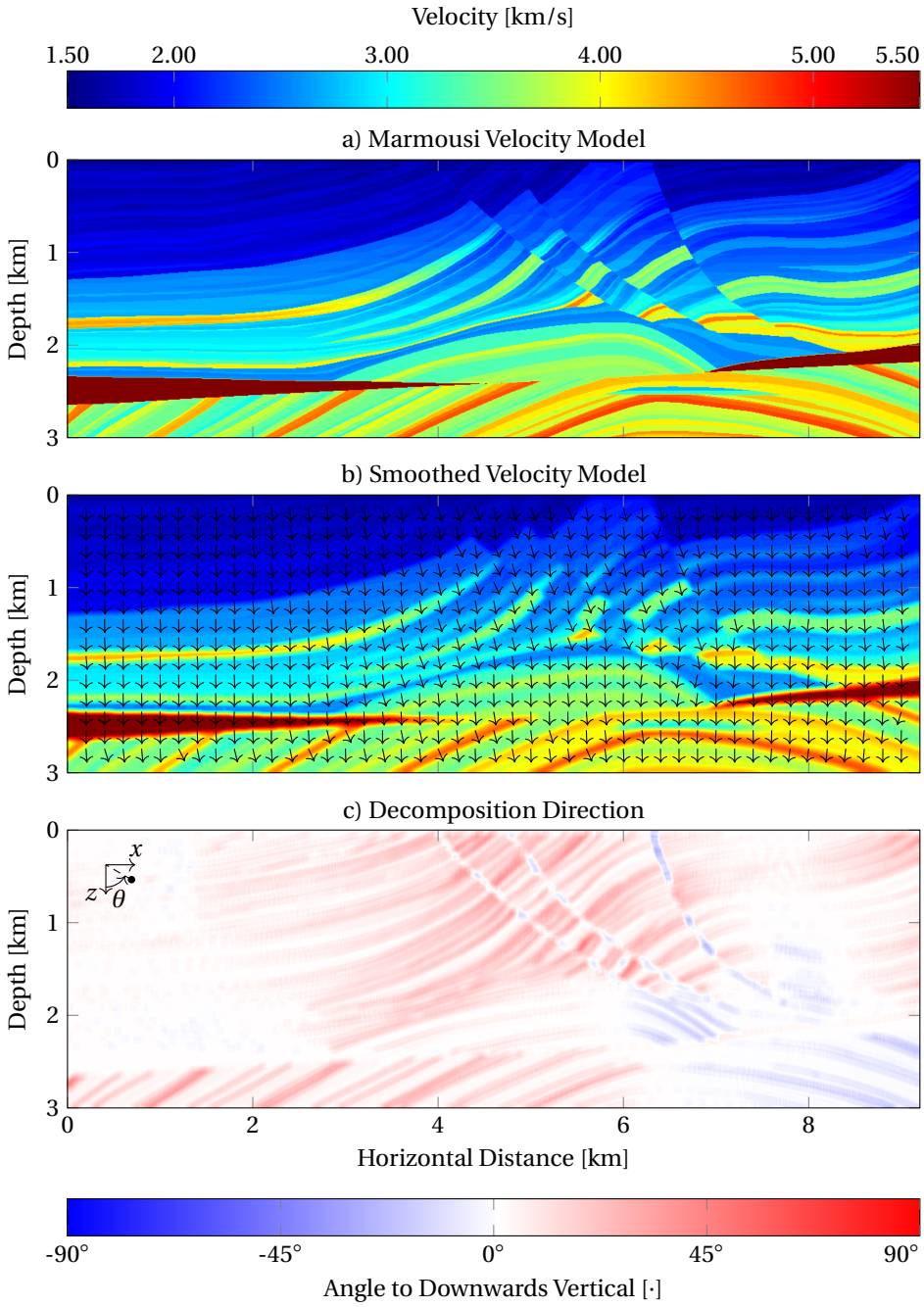

Figure 2.5: a) Marmousi velocity model smoothed using a 10x10 gridpoints moving-average filter (b) with associated downwards-pointing gradient-direction vectors, taken from decomposition direction map (c) used to steer directional wavefield decomposition.

2.3. NUMERICAL IMPLEMENTATION

Implementation of snapshot wavefield decomposition for homogeneous media is simple in the wavenumber domain and can be used as an approximation for heterogeneous media. The general decomposition workflow for multicomponent data in a homogeneous three-dimensional (3D) volume begins with transforming the data to the 3D-wavenumber-time domain, see Figure 2.6. Then for each desired decomposition direction, not all decomposition directions as in Section 2.2.6, the wavefield is iteratively decomposed and the decomposed results are transformed back to the space domain. At the end of each iteration only those points at which the current decomposition direction matches the desired decomposition at said point are kept. Thus the desired decomposed fields corresponding to the spatially varying decomposition direction are built up. This requires two forward spatial Fourier transforms, followed for each iteration by multiplication of the pressure and particle velocity with large diagonal operations to scale the transformed fields to each other for decomposition, depending on normalization, and two inverse Fourier transforms, followed by extracting the desired decomposed points. Based on Figure 2.6 this seems simple to implement, there are, however, some caveats.

In Section 2.2.6 we described how to achieve spatially varying decomposition directions. This required decomposing the wavefield according to all possible decomposition directions. This is numerically expensive. Hence, we suggest to precompute a list of desired decomposition directions, based on an impedance model for example. This list, if the decomposition direction angles are not strictly acute, is then scanned to eliminate decomposition directions pointing in opposite directions, as these can be computed simultaneously. To further reduce the workload the list of decomposition directions can be binned; later the decomposition results are then interpolated between their nearest bin centres.

It should be noted here that Equation 2.50 can become numerically unstable if the gradient is very small due to the inherent limited numerical precision of floating point numbers on computers. For the case where the medium is homogeneous we suggest to define a desired direction. For regions where the direction may be numerically imprecise we suggest to either increase the floating point precision of the computation or to interpolate these values based on neighbours to at least ensure a smoothly varying decomposition direction. For our examples the used models were stored using 32-bit IEEE 754 floating-point numbers, while the gradient computations were done by increasing the precision of these numbers to double-precision 64-bit IEEE 754 floating-point numbers. This avoided numerical precision problems in computing the gradient.

For the interpretation of decomposed snapshots we suggest that the decomposition-direction map is spatially smooth. The employed algorithm, however, can handle both smooth and non-smooth decomposition-direction maps. Using smooth decomposition-direction maps avoids sharp contrasts in decomposed amplitudes, while decomposed events remain continuous. This aids greatly in the visual inspection and interpretation of decomposed snapshots. Smooth decomposition direction maps can be computed with Equation 2.50 by either using a smooth impedance model, as we have done in our examples, or by smoothing the direction map after computing it.

Note that the decompositions require Fourier transforms, which for discrete data are generally formulated as finite dense circulant matrices acting on the whole domain

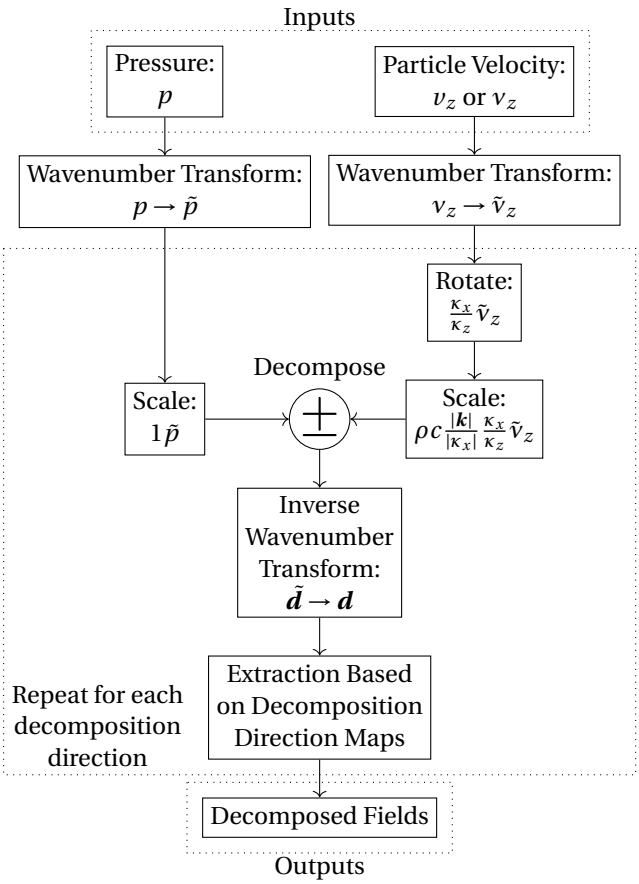

Figure 2.6: Workflow of directionally steered snapshot wavefield decomposition.

under the assumption that the domain is periodic. This is generally inaccurate as it is implicitly assumed that the signal is periodic in space, suggesting the need for tapering at domain edges to avoid step discontinuities at model boundaries in the space domain and associated aliasing in the wavenumber domain. As we will demonstrate with the synthetic examples in Section 2.4 this is not strictly necessary but may improve results. In contrast to the Fourier transform the rotation and scaling operators are diagonal matrices and only suffer from incorrectly scaling spatially aliased signals.

Furthermore, for discrete data when the wavefield components do not lie on the same space-time grid it is imperative for best results that the two components are interpolated to lie on the same grid. This ensures that the associated temporal and spatial phase shifts between the signals do not contaminate the decomposition. We found for our synthetic finite-difference examples that it was often acceptable to have the fields not on the same time grid, but they had to be on the same space grid. This is a function of the signal bandwidth in the wavenumber and frequency domains. The wider the bandwidth and

the closer these were to modelling limits, like the Courant number, the larger the error grew.

For all the figures in this work we shifted the particle velocities onto the pressure grid in the wavenumber domain by multiplying in two spatial dimensions the horizontal particle velocity by $\exp(-ik_x\Delta x/2)$, where Δx is the horizontal grid spacing, and the vertical particle velocity by $\exp(-ik_z\Delta z/2)$, where Δz is the vertical grid spacing. We also found that it was often also acceptable to simply linearly interpolate the particle velocities onto the pressure grid. This can be significantly faster and does not suffer from the inherent wrap-around effect of most discrete Fourier transforms, the resulting amplitudes however are often less accurate. To interpolate the particle velocity to the same time grid we used half the time derivative of the particle velocity at every time instance, which is a by-product of using a staggered finite difference scheme to step wavefields forward in time. As we often found that this is unnecessary for acceptable results in practice, all figures in this work show decomposed results without interpolating either the pressure or particle velocities onto the same time grid. Note that we do not suggest to shift staggered wavefields onto the same time grid in the frequency domain as this removes the advantage of this method of being able to act exclusively on snapshots of a wavefield.

For waves travelling at near-right angles to the decomposition direction, the wavenumber scaling in, for example, Equation 2.22 may become numerically unstable. In this case it is advantageous to cast the problem in terms of the magnitude of the particle-velocity vector, Equation 2.28. Using the magnitude of the particle velocity in 2D comes at the cost of requiring an additional spatial Fourier transform over the other component of the particle velocity.

We would like to conclude this section with a discussion on the numerical aspects of the decomposition algorithm, which is dominated by the Fourier transforms. In our case these were implemented through the FFTW 3.3.6-pl2 library (Frigo and Johnson, 2005). The compute time of the Fast Fourier Transforms (FFT) are expected to scale with $n\log(n)$, where n is the number of data points to be Fourier transformed. As such, we expect the compute time of the decomposition algorithm, when decomposing along one direction, to scale in the same fashion. When decomposing along many directions the compute time is expected to linearly increase with the number of directions to decompose along, as an additional Fourier transform is needed per additional direction. Although all examples in this work are in two spatial dimensions, decomposition in three spatial dimensions is also feasible. This comes at the cost that the algorithm's compute time is expected to increases approximately proportionally to n_3, the number of elements in the third spatial dimension, with respect to a two dimensional model that has the same size in the first two dimensions. When decomposing while modelling in a high-performance computing setting, the decomposition step can be offloaded to other compute nodes or dedicated FFT hardware to reduce the impact of the decomposition on the modelling time. Alternatively the decomposition operator can be reduced in size, written in the space domain and then iteratively convolved with the snapshot to decompose it. This reduces accuracy, especially for waves travelling nearly perpendicular to the decomposition direction.

In order to compare compute times, the average decomposition times for 100 1D, 2D

and 3D snapshots were determined, where each dimension had a size of 1000 points. We used a single thread without vectorization on a stock Xeon E5-2680 v3 central processing unit. The system's random access memory consisted of eight 32 GB Samsung M393A4K40BB1-CRC modules at 2,133 MHz with default settings in a dual channel configuration. The average compute times for the 1D, 2D and 3D snapshots are 6 μs, 15 ms and 29 s respectively. Between the 1D and 2D cases we expected a 2,000 fold increase, while between the 2D and 3D cases we expected a 1,500 fold increase. The above tests were assuming only one decomposition direction, but when 99 additional decomposition directions are also included, the compute times increase accordingly. Assuming we take 100 different directions, requiring 101 Fourier transforms, the average compute time of the 2D snapshots increased to 754 ms. For the 3D case the average compute time was 1460 s. Note that these values are only indicative and can vary between compute systems.

2.4. SYNTHETIC EXAMPLES

We now show synthetic examples to illustrate the theory and concepts discussed earlier. We begin with a constant-density constant-acoustic-velocity example and move on from there to a layered model with velocity and density variations and from there to the heterogeneous-velocity Marmousi model. We demonstrate on these models the various decompositions and their characteristics.

2.4.1. CONSTANT-PARAMETER MODEL

To illustrate the simplest case of decomposition, we choose a model where the density is constant at 1000 kg m^{-3} and the medium velocity is 1 km s^{-1}. The grid is 500 m-by-500 m discretized with a 1 m sampling rate and a 60 Hz peak-frequency Ricker wavelet, sampled every 0.5 ms, is injected as a volume injection source at the centre of the model with a 0.0175 s time delay. Figure 2.7 displays snapshots of said wavefield. Figures 2.7a-d show advancing snapshots of the wavefield, decomposed into down-going wavefields below. Figure 2.7e shows on the left a snapshot between Figures 2.7c and 2.7d in time. Now, however, the snapshot has not only been up-down decomposed but also left-right, as indicated by the arrows in the different panels. To the right of the decomposed snapshots are the corresponding amplitudes of the snapshots around the origin in the wavenumber domain.

The total wavefields, the central panels in Figures 2.7e and 2.7f, were first decomposed using Equation 2.23, zeroing the horizontal or vertical wavenumbers as applicable. To compute the wavefields travelling in quadrants the total wavefield was also decomposed into up- and down-going particle-velocity-normalized wavefields. These were rotated using Equation 2.26 to find the up- and down-going horizontal particle velocities. These in turn were then used in conjunction with the up- and down-going pressure to decompose the wavefields again into left- and right-going wavefields.

Consider the wavenumber spectrum of the total field, central panel of Figure 2.7f, which has a jittery amplitude behaviour due to the interfering waves in the central pane of Figure 2.7e. Wavefields propagating in opposite directions are destructively interfering, causing the amplitude of the total wavefield to be smaller than that of the decomposed fields. Furthermore, the amplitude distribution in the total field around the origin is not

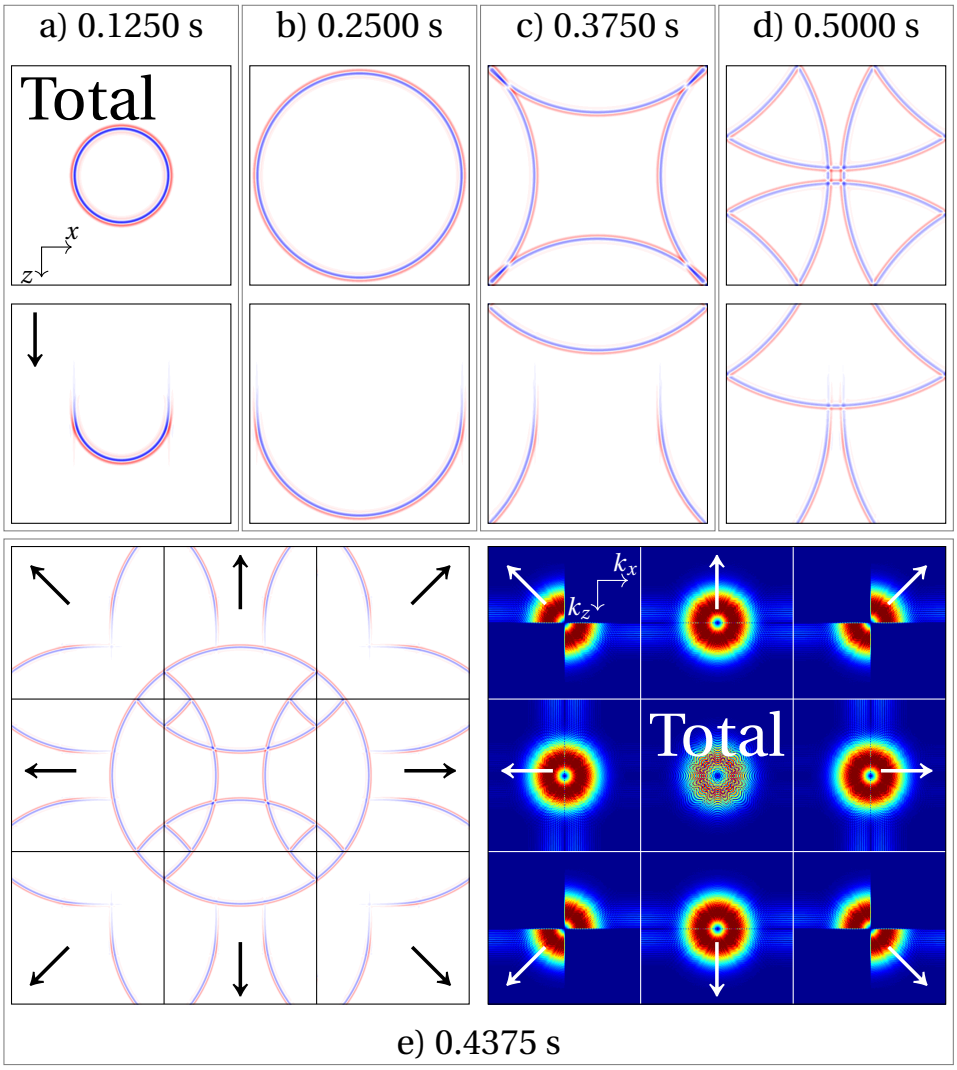

Figure 2.7: Homogeneous acoustic wavefield decomposition on a 500m-by-500m 1 km s^{-1} homogeneous model. The top row of (a)-(d) shows the total pressure snapshots decomposed into down-going snapshots below. e) shows a snapshot of the total pressure at 1.75 s directionally decomposed into quadrants. f) displays the corresponding wavenumber spectra, with the images centred on the origin. Note that the wavefields were decomposed in the wavenumber domain, and therefore low-wavenumber decomposition artefacts can be observed as vertical and horizontal bands. Furthermore the displayed coordinate systems in (a) also applies to (b), (c), (d) and the left side of (e), while the coordinate systems in the upper left panel on the right of (e) applies to the adjacent panels).

as clear as for the decomposed fields. After decomposition it is much clearer, however, that edge-related artefacts and artefacts due to the asymptotic scaling of the particle ve-

locity are also boosted. The amplitude spectra of the decomposed fields appear identical, however, the dominant difference between the decomposed fields is in the phase (not shown). This is expected as the wavefield radiated spherically away from the source at the centre. Further decomposing the wavefield corresponds to a simple quadrant mute in the wavenumber domain. Note that the decomposition order is highlighted by the horizontal erroneous bands due to asymptotic scaling. These bands would have been vertical if the wavefield had been first left-right decomposed and then up-down.

2.4.2. CONSTANT PARAMETER MODEL: COMPARISON OF DIFFERENT SCALINGS

To illustrate the possible numerical errors introduced by using the wavenumber-based scaling of Equation 2.22, as opposed to the magnitude of the particle-velocity vector, Equation 2.28, see Figure 2.8. Figures 2.8a and 2.8b show the pressure and specific-acoustic-impedance-scaled vertical particle velocity due to a sum of unit-amplitude Ricker wavelet plane waves travelling from left to right with increasing obliquity to the vertical axis. Figures 2.8c and 2.8d show the corresponding amplitudes around the origin (centre of panel) in the wavenumber-time domain. Note that the vertical particle velocity (Figure 2.8d) is missing the horizontally travelling wave corresponding to the horizontal red line segment in Figure 2.8c, see black ellipse.

We now scale the vertical particle velocity to the pressure using Equations 2.22 and 2.28, resulting in Figures 2.8e and 2.8f. Note that the scaled vertical particle velocity is set to zero for $k_z = 0$. When comparing Figures 2.8e and 2.8f to 2.8c and 2.8d the amplitudes of Figures 2.8c and 2.8f are very similar, except where $k_z = 0$, while the amplitudes of Figure 2.8e diverge from those in Figure 2.8f away from the origin as one approaches $k_z = 0$. The reason for this divergence is twofold: 1) numerical accuracy of the asymptotic wavenumber scaling in Equation 2.22 degrades as one approaches $k_z = 0$, resulting in horizontal artefacts as can be seen in the dashed circles in Figures 2.8g and 2.8h, and 2) aliasing due to the finite size of the domain causes wrap-around artefacts due to the cyclic nature of the employed Fourier transform, as can be seen in the spy-glasses in Figures 2.8g and 2.8h. The aliasing causes high wavenumbers to map to lower wavenumbers, and vice versa, which are subsequently incorrectly scaled. It is suspected that one does not see this effect in Figure 2.8h because the aliasing in the horizontal and vertical wavenumber for a given point in the wavenumber-time domain, when used to calculate the magnitude of the particle velocity, is equal/similar to the aliasing for the pressure at said point. It appears that using the magnitude of the particle velocity for decomposition on finite non-periodic domains is less corrupted by aliasing artefacts, suggesting that Equation 2.28 should be used over Equation 2.22 whenever possible.

2.4.3. FOUR-LAYER MODEL

In the previous examples, we did not show the effect of variations in medium parameters on the model. Figure 2.9 shows up-down decomposed wavefields for a four-layer model, with a density increase, velocity increase and constant specific-acoustic-impedance interface from top to bottom, as shown in Figure 2.9a. Figure 2.9b shows a pressure snapshot due to a volume injection source at the origin injecting a 50 Hz-peak-frequency Ricker wavelet with a time delay of 0.1 s. Figure 2.9f shows the corresponding recorded wavefield

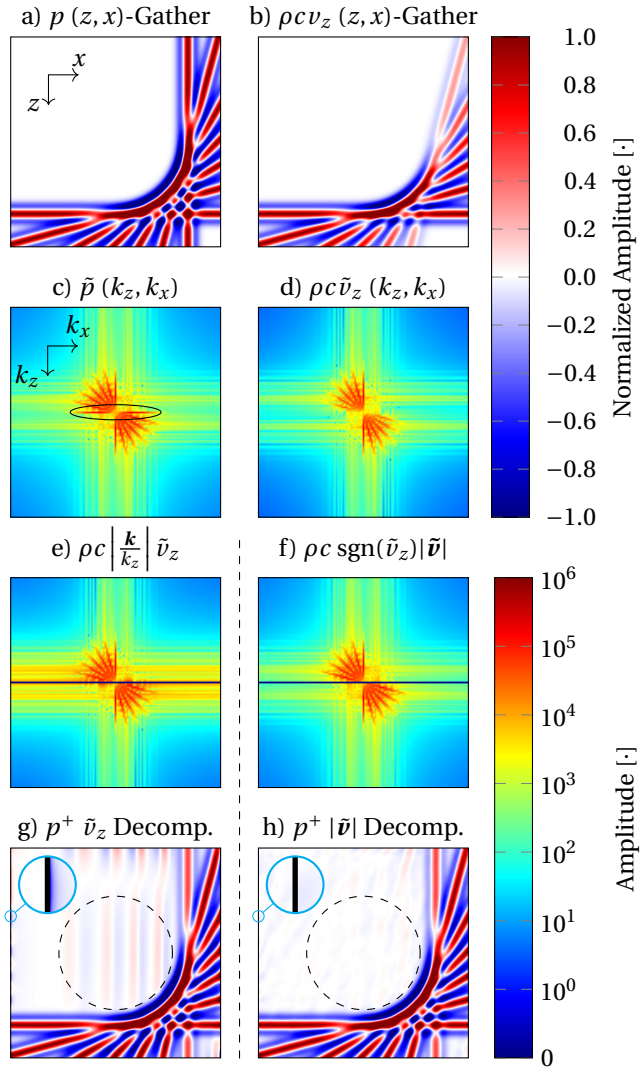

Figure 2.8: a) Superposition of pressure plane waves at 0°, 15°, 30°, 45°, 60°, 75° and 90° to the vertical with the (b) associated specific-acoustic-impedance-scaled vertical particle velocity. (c) and (d) are extracts around the origin of the magnitude of the wavenumber transforms of (a) and (b) respectively. (e) and (f) show scaled version of (c) and (d) according to Equations 2.22 and 2.28 respectively. The fields were muted where $k_z = 0$. (g) and (h) show the corresponding decomposed wavefields in the space domain. Please note that in all panels the origin is at the centre of the image and that the coordinate system displayed in (a) applies to (a, b, g and h), while the coordinate system shown in (c) applies to (c–f).

at a depth of 150 m, indicated by the dashed line in Figures 2.9b-d. Note that the top and bottom boundaries are both free surfaces while the left and right boundaries are absorbing, more precisely they are 500-element-wide perfectly matched layer boundaries

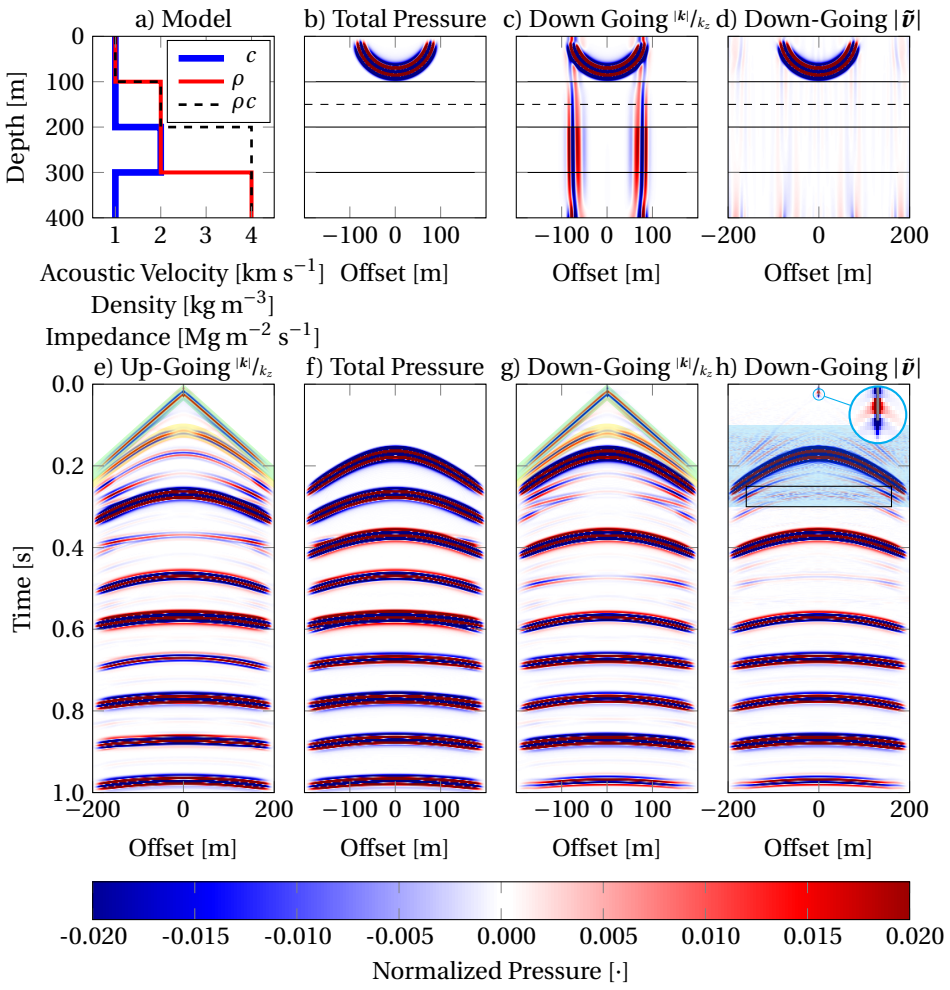

Figure 2.9: Pressure snapshot (b) from a four-layer model (a) decomposed into down-going waves by either scaling the vertical particle velocity in the wavenumber domain according to Equation 2.23 (c), or by using the magnitude of the particle-velocity vector according to Equation 2.35 (d). (f-h) show the corresponding wavefields recorded on the dashed surfaces in (b-d), while (e) shows the up-going wavefield found by subtracting (g) from (f) and dividing by two.

(Chew and Liu, 1996).

The wavefields in Figures 2.9b and 2.9f were then decomposed, using Equations 2.23 and 2.28, into down-going waves in Figures 2.9c and 2.9g, and Figures 2.9d and 2.9h respectively. Figure 2.9e shows the up-going pressure wavefield based on Equation 2.23. Note that all panels were tapered at the edges to avoid the Gibbs-Wilbraham phenomenon. Please also note that the amplitudes have been clipped at 5% of the maximum to illustrate that the errors are generally smaller than 1%.

Comparing Figures 2.9b-d, the large vertical artefacts in Figure 2.9c are immediately evident. These are caused by the incorrect scaling of small vertical wavenumbers due to aliasing artefacts because of the implicit fast Fourier transform jump-discontinuity at the surface. These artefacts are much smaller in Figure 2.9d. However, small artefacts associated to small vertical wavenumbers are visible throughout Figure 2.9c. It is suspected that these are caused by the interaction of the aliasing of the horizontal and vertical particle velocities, among other possible errors. These errors are also in part due to the heterogeneous medium.

We can see the same artefacts in Figures 2.9e, 2.9g and 2.9h, where the vertical bands in Figure 2.9c now appear as an erroneous event in Figures 2.9e and 2.9g that resembles a conventional direct wave when the source is at the same depth level as the acquisition surface, see shaded green area. When comparing Figures 2.9g and 2.9f there is another event that arrives in Figure 2.9g before the direct wave in Figure 2.9f, see yellow area. This event is associated with the erroneous vertical bands that arise due to the amplitude discontinuity when the wavefield reflects at the first interface, similar to the two vertical artefacts due to the tapered edge discontinuity at the top of the model causing two erroneous vertical events in Figure 2.9c. These errors are mostly absent from Figure 2.9h, they are only visible in time from about 0.1 s to 0.3 s, the cyan area, along with other noise, in the form of high-frequency noise. This noise is most evident inside the black box. Evidently decomposition in terms of the magnitude of the particle velocity, Equation 2.28, is not as sensitive to these errors as decomposition in terms of Equation 2.23.

Figure 2.9h, however, also suffers from other errors. Between 0.1 s and 0.3 s there appears the afore mentioned high-frequency noise, see cyan area. This noise is again due to the interaction of artefacts in both the horizontal and vertical particle velocities. If the model domain is made larger the errors become smaller, but they do not completely vanish as they are also partially due to the variations in medium parameters, which are quite strong for this model. Qualitatively decomposing in terms of the magnitude of the particle-velocity vector, Figure 2.9h, appears to perform better than only scaling the vertical component of the particle velocity in the decomposition, Figure 2.9g, when compared to conventional surface-normal decomposition, which is ideal for this scenario. The errors are more concentrated in Figure 2.9g though.

Note that both Figures 2.9h and 2.9g, as well as conventional decomposition, show errors around the source if the source is not explicitly included in the decomposition scheme. This can be seen in the spyglass in Figure 2.9h. In this case these errors have two components, the source itself, which was not properly accounted for, and the fact that the data were modelled using a staggered-grid finite-difference scheme, where the wavefield mismatch in space and time between the pressure and particle velocity is largest around source locations.

2.4.4. MARMOUSI MODEL: (UP-LEFT)-(DOWN-RIGHT) DECOMPOSITION

We have demonstrated that snapshot decomposition performs well on layered models. Let us now relax the lateral-homogeneity condition and consider fully heterogeneous velocity models. Figure 2.10 shows in the upper right the Marmousi velocity model (Figure 2.10b), with the source location marked using a red cross. In this case a 50 Hz Ricker

wavelet was injected. Figure 2.10c shows the total pressure wavefield for a snapshot at 0.9 s. The other two panels shows the pressure wavefield decomposed into up- and right-going waves, Figures 2.10a and 2.10d respectively. In this case the wavefields were decomposed using Equation 2.23, including the use of the horizontal particle velocity to account for horizontally travelling waves. Interesting here is to look at the curvature of the dominant events, and to see that they are well decomposed. The unexpected vertical and horizontal events in Figures 2.10a and 2.10d respectively are caused by the incorrect scaling due to the asymptotic nature of Equation 2.23 and the inherent incorrect scaling of aliased waves due to the heterogeneous nature of the model. As there is no reference decomposition for a model of this complexity it is difficult to grade the accuracy of the decomposition. Overall and when seen from one snapshot to another the decomposition appears to do well.

Figure 2.11 allows us to compare decomposed common-shot gathers at the source depth level, which were decomposed using Equation 2.35 at every time sample. We can see that we are able to nicely decompose the wavefield. Comparing the down-going wavefield to the plane-wave down-going reference response, one finds they are nearly identical, except at the bottom of the panels, because the plane-wave decomposed panel was tapered at the top and bottom to avoid wraparound artefacts. Note that for very early times the wavefield was not decomposed, as source artefacts were too dominant, due to the fact that the source was not taken into account in the decomposition.

2.4.5. MARMOUSI MODEL: IMPEDANCE-BASED DECOMPOSITION-DIRECTION STEERING

We have demonstrated that wavefields propagating in the Marmousi model can be easily decomposed along spatially invariant directions. We can take the decomposition a step further by decomposing in the direction normal to medium interfaces, as discussed in Section 2.2.8. Figure 2.12 shows the decomposition results, found using Equation 2.47, associated to the proposed decomposition directions in Figure 2.5, which were computed using Equation 2.50. Figure 2.12c shows the down-going interface-normal decomposed pressure-normalized wavefield. This decomposed wavefield, although very similar to the normal down-going pressure wavefield, is important for imaging with acoustic wavefields.

As Figure 2.12c is difficult to interpret with respect to the prescribed decomposition direction, Figure 2.12d shows desired decomposition directions radiating away from the source location. Using these directions we would then decompose the wavefield into waves travelling away from and towards the source. If one follows the curvature of the wavefronts in Figure 2.12e one can clearly see that they suggest the wavefield is propagating away from the source, with the exception of the dominant wave travelling upwards. This wave, however, is also travelling away from the source, its propagation angle is just nearly at a right angle to the decomposition direction. This wave, however, vanishes right below the source as there it is propagating towards the source.

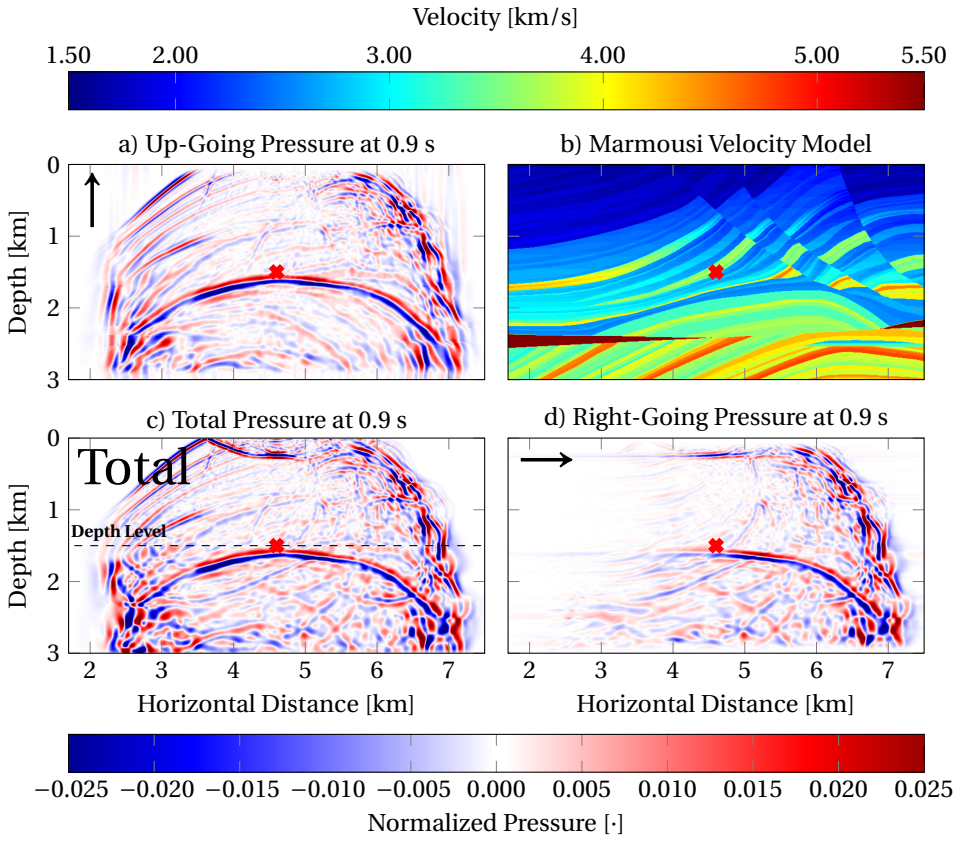

Figure 2.10: Pressure snapshot (c), from the constant-density Marmousi model (b), directionally decomposed into up- (a) and right-going (d) pressure-normalized wavefields. The source location is indicated by a red cross. Amplitudes are normalized to the unit amplitude Ricker source wavelet.

2.5. DISCUSSION & CONCLUSION

Conventional up-down wavefield decomposition is applied to wavefields recorded on horizontal surfaces to decompose into wavefields propagating up and down. This study took a different approach to conventional wavefield decomposition and derived operators that decompose wavefields at one instance in time that are known everywhere in space, effectively using a temporal surface instead of a spatial surface. This has advantages and disadvantages when compared to conventional decomposition.

Its biggest disadvantage is that the decomposition does not correspond to how acoustic data is generally acquired, which is on a single surface and not everywhere in space for one instance in time. This implies that this method is better suited for other applications, like decomposing wavefields as they are being modelled, for example using finite-difference schemes, to improve RTM imaging results, see Díaz and Sava (2015). This is where the proposed approach excels as the wavefield is known everywhere from one time step to the next, allowing for directional wavefield decomposition at every time

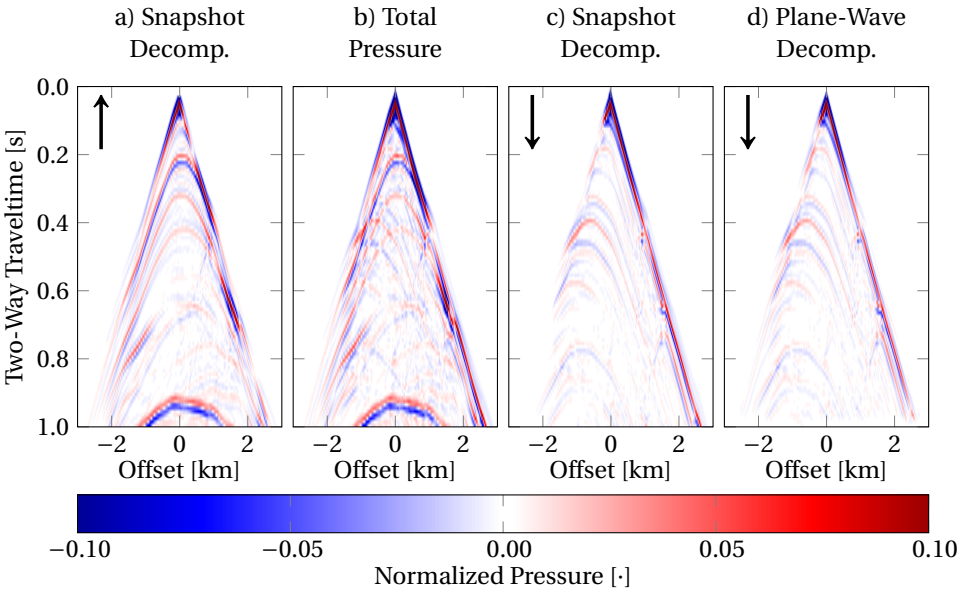

Figure 2.11: Directionally decomposed common-shot gathers, from the Marmousi model, through the source depth level, indicated on Figure 2.10. On the far right is the down-going resampled plane-wave decomposed reference response, see Suprajitno and Greenhalgh (1985), which was tapered at the top and bottom.

step, as opposed to having to record the wavefield and then later decompose it using conventional decomposition along some surface.

Another advantage over conventional decomposition is that in conventional decomposition the decomposition direction is always normal to the surface along which the decomposition occurs, whereas for the proposed scheme the wavefield can be decomposed into any direction. The same is achievable using conventional decomposition if the wavefield is known everywhere in space and time. Hence the proposed scheme is ideal for any algorithms based on snapshots of a wavefield like RTM, which would benefit from the ability to locally decompose wavefields normal to interfaces, not just between in- and out-going wavefields but also according to the quadrant from which the wave arrives using sub-decomposition.

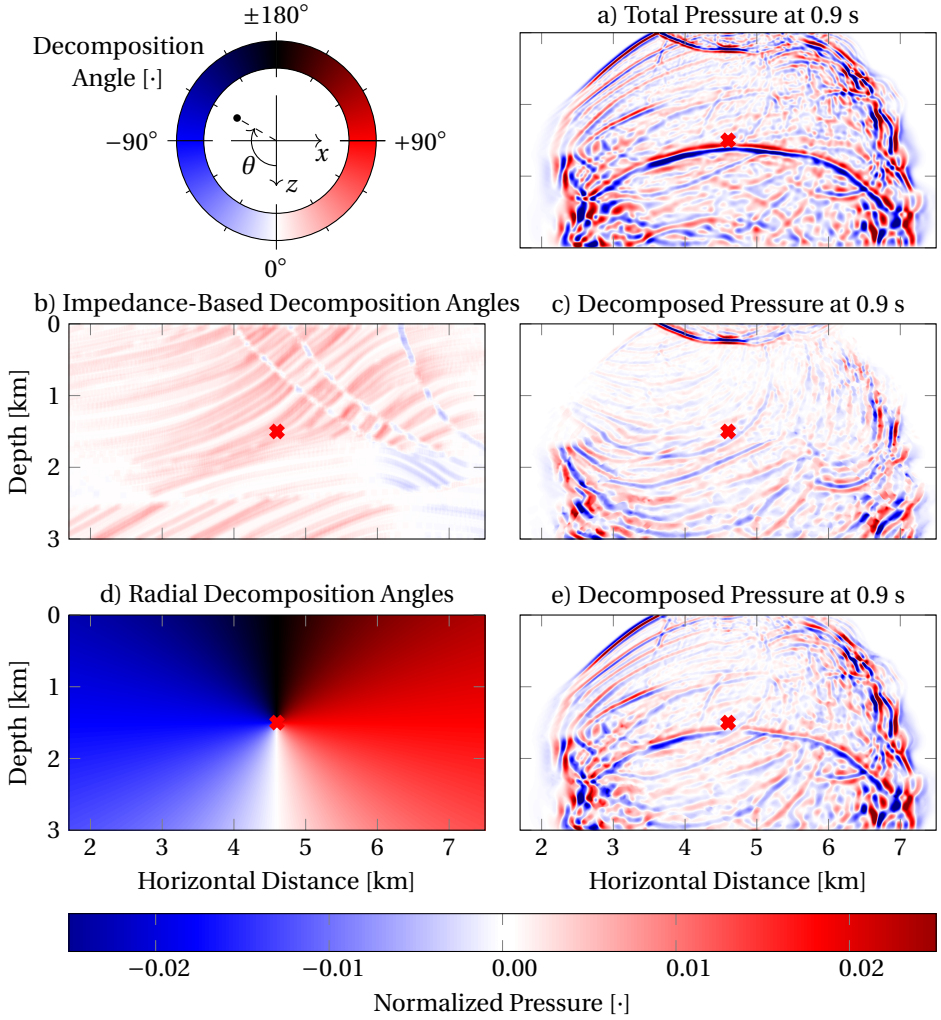

Figure 2.12: Acoustic wavefield propagated from the center of the Marmousi model, see Figure 2.5 for the velocity model, decomposed along variations in the impedance and radially away from the source. a) shows the total pressure wavefield 0.9 s after source excitation; the source location is indicated by a red cross. b) and d) show the decomposition angles parallel to impedance variations and radially away from the source location. c) and e) show the corresponding decomposed pressure-normalized wavefields according to the angles in b) and d) respectively. Note that for e) the wavefield at the source location was not decomposed as any wavefield at the source location must propagate away from it. Note that amplitudes are normalized to the unit amplitude Ricker source wavelet.

3

Acoustic Snapshot Directional Wavefield Decomposition in Relation to Other Decomposition Techniques

In the previous chapter we demonstrated the efficacy of acoustic snapshot directional wavefield decomposition. However, it is not the only directional wavefield decomposition, many have been published in the literature. In this chapter we will discuss prominent directional wavefield decomposition techniques and derive them in terms of acoustic snapshot directional wavefield decomposition. This will allow us to demonstrate that these decomposition schemes are mutually related.

3.1. INTRODUCTION

In the previous chapter we presented acoustic snapshot directional wavefield decomposition with little attention to the relation to other common wavefield-decomposition techniques. We will now relate them. We begin by discussing and deriving Poynting decomposition. From there onward, more complex schemes like plane-wave and analytic decomposition are discussed. Finally surface-normal decomposition on horizontal surfaces is discussed as the progenitor of acoustic snapshot directional wavefield decomposition.

3.2. POYNTING DECOMPOSITION

Poynting decomposition is a single-event space-time-domain labelling scheme. Poynting decomposition, named after Poynting (1884), uses local Poynting vectors, which are directional energy-flux-density vectors, to determine the direction a wave is travelling in. For an acoustic wavefield the Poynting vector is simply the product of the pressure p and particle velocity vector $\boldsymbol{v}$ (Yoon and Marfurt, 2006). In a locally homogeneous medium the Poynting vector indicates the wave-travel direction at a given point under the condition that the wavefield at that point is only travelling in one direction, i.e. there is no interference of waves at the point. This is often approximately the case for the direct wave in the vicinity of its source, and, as such, this decomposition finds use in reverse-time migration in low-reflectivity media, see e.g. Yoon and Marfurt (2006).

Note that when we speak of interfering wavefields in this section we mean a superposition of wavefields that at a given point in space and time travel in more than one direction. If the wavefield at a given space-time point only travels in one direction then it is interference free.

Components of interference-free Poynting vectors $p\boldsymbol{v}$ are positive if the wavefield is travelling in the positive direction along the corresponding axis and negative if the wavefield is travelling in the opposite direction. Where a component is zero the wavefield is travelling orthogonally to said axis. This can be used to label non-interfering wavefields according to their direction of propagation:

$$\begin{pmatrix} p_z^+ \\ p_z^- \end{pmatrix} = \begin{pmatrix} h(\ \ pv_z) \\ h(-pv_z) \end{pmatrix} p, \tag{3.1}$$

where $h()$ is the Heaviside step function, and p^+ is the pressure field travelling in the positive z direction, while p^- travels in the negative z direction. Equation 3.1 also holds for the particle velocity:

$$\begin{pmatrix} \boldsymbol{v}_z^+ \\ \boldsymbol{v}_z^- \end{pmatrix} = \begin{pmatrix} h(\ \ pv_z) \\ h(-pv_z) \end{pmatrix} \otimes_{\mathrm{k}} \boldsymbol{v}, \tag{3.2}$$

where $\otimes_{\mathrm{k}}$ denotes the Kronecker product.

The advantage of decomposing acoustic wavefields with Equation 3.1 or 3.2 is that the decomposition is both local in space and time and is trivial to implement. However, it fails for interfering waves as the local Poynting vector is then rotated to point somewhere, depending on the relative magnitudes between the interfering waves, possibly in an orthogonal direction. This means that Equation 3.1 or 3.2 will only hold in the limit as the wave to be decomposed has a much larger amplitude than that of the interfering

wavefield; this is often the case for the direct wavefield in acoustics. As such, Poynting decomposition is more of a labelling scheme based on the dominant local wave travel direction than an actual decomposition scheme.

EQUIVALENCE BETWEEN POYNTING & SNAPSHOT DECOMPOSITION

To demonstrate the equivalence of Poynting decomposition to acoustic snapshot directional wavefield decomposition in a homogeneous medium for non-interfering waves we return to Equation 2.23, repeated here for convenience:

$$\begin{pmatrix} \tilde{p}_z^+ \\ \tilde{p}_z^- \end{pmatrix} = \frac{1}{2} \begin{pmatrix} 1 & \frac{\rho c}{\cos(\tilde{\theta}_z)} \\ 1 & -\frac{\rho c}{\cos(\tilde{\theta}_z)} \end{pmatrix} \begin{pmatrix} \tilde{p} \\ \tilde{v}_z \end{pmatrix}, \tag{2.23}$$

where θ_z is defined according to Equation 2.20 and we neglect to consider waves travelling orthogonally to the desired decomposition direction z.

We now consider three cases. In the first case we consider that at a given point $\boldsymbol{k}_0$ in the wavenumber domain the wave is only travelling in the positive z direction, i.e. $\tilde{p}_z^-(\boldsymbol{k}_0, t) = 0$. In the second case we assume that the wavefield is only travelling in the negative z direction, i.e. $\tilde{p}_z^+(\boldsymbol{k}_0, t) = 0$. In the third case we take the situation that the pressure field at $\boldsymbol{k}_0$ corresponds to the sum of two wavefields travelling in opposite directions, i.e. $\tilde{p}_z(\boldsymbol{k}_0, t)$. Note that the following derivation will be in the wavenumber-time domain, as was done in the previous chapter.

CASE I: $\tilde{p}_z^-(\boldsymbol{k}_0, t) = 0$

If we consider that at a given point $\boldsymbol{k}_0$ in the wavenumber domain the corresponding plane wave in the space domain is only travelling in the positive z direction then for that point $\boldsymbol{k}_0$ we have that $\tilde{p}_z^-(\boldsymbol{k}_0, t) = 0$ and $\tilde{v}_z^-(\boldsymbol{k}_0, t) = 0$. Effectively this means that at $\boldsymbol{k}_0$ the wavefield is only travelling in one direction. Using this assumption the bottom row of Equation 2.23 gives:

$$\tilde{p}(\boldsymbol{k}_0, t) = \frac{\rho c}{\cos(\tilde{\theta}_z)} \tilde{v}_z(\boldsymbol{k}_0, t). \tag{3.3}$$

The fraction in Equation 3.3 is always positive since $\rho c \geq 0$ and $\cos(\tilde{\theta}_z) > 0$, as $-\pi/2 < \theta_z \leq \pi/2$, for waves not travelling orthogonally to the desired decomposition direction. In the absence of waves travelling in the negative z direction the following must then hold:

$$\operatorname{sgn}(\tilde{p}_z^+) = \operatorname{sgn}(\tilde{v}_z^+), \tag{3.4}$$

for waves travelling in the positive z direction. Furthermore the amplitude of the pressure and particle velocity are related:

$$|\tilde{p}| = \frac{\rho c}{\cos(\tilde{\theta}_z)} |\tilde{v}|. \tag{3.5}$$

CASE II: $\tilde{p}_z^+(\boldsymbol{k}_0, t) = 0$

We now consider the case where $\tilde{p}_z^+(\boldsymbol{k}_0, t) = 0$ and $\tilde{v}_z^+(\boldsymbol{k}_0, t) = 0$. In this case the top row of Equation 2.23 gives:

$$\tilde{p}(\boldsymbol{k}_0, t) = -\frac{\rho c}{\cos(\tilde{\theta}_z)} \tilde{v}_z(\boldsymbol{k}_0, t). \tag{3.6}$$

From this we can gather that for all wavefields travelling in the negative z direction the following must hold:

$$\operatorname{sgn}(\tilde{p}_z^-) = -\operatorname{sgn}(\tilde{v}_z^-). \tag{3.7}$$

Furthermore Equation 3.5 also holds in this case.

CASE III: $\tilde{p}_z^+(\boldsymbol{k}_0) \neq 0$ & $\tilde{p}_z^-(\boldsymbol{k}_0) \neq 0$

In this case we consider interfering waves so that we have waves travelling in opposite directions at a point $\boldsymbol{k}_0$ in the wavenumber domain. In this case we cannot further simplify Equation 2.23 and break it down to signum and amplitude relations. This means that Equations 3.4–3.7 do not hold when a point in the wavenumber domain corresponds to plane waves travelling in opposite directions.

TRANSFORMING BACK TO THE SPACE DOMAIN

We now have the necessary ingredients to derive Poynting decomposition. We write the pressure wavefield $\tilde{p}$ as a sum of wavefields $\tilde{p}_z^+$ and $\tilde{p}_z^-$, which are travelling in opposite z directions. Transforming this back to the space domain we find for the pressure and particle velocity in the z direction:

$$p = \frac{1}{(2\pi)^n}\int_{\mathbb{R}^n} \tilde{p}e^{-i\boldsymbol{k}\cdot\boldsymbol{x}}\mathrm{d}\boldsymbol{k} = \frac{1}{(2\pi)^n}\int_{\mathbb{R}^n} (\tilde{p}_z^+ + \tilde{p}_z^-)e^{-i\boldsymbol{k}\cdot\boldsymbol{x}}\mathrm{d}\boldsymbol{k}, \tag{3.8}$$

$$v_z = \frac{1}{(2\pi)^n}\int_{\mathbb{R}^n} \tilde{v}_z e^{-i\boldsymbol{k}\cdot\boldsymbol{x}}\mathrm{d}\boldsymbol{k} = \frac{1}{(2\pi)^n}\int_{\mathbb{R}^n} (\tilde{v}_z^+ + \tilde{v}_z^-)e^{-i\boldsymbol{k}\cdot\boldsymbol{x}}\mathrm{d}\boldsymbol{k}, \tag{3.9}$$

where n is the spatial dimensionality of the system and $\mathbb{R}$ denotes the set of real numbers. Using Equations 3.4, 3.5 and 3.7 we can rewrite Equation 3.9 as:

$$v_z = \frac{1}{(2\pi)^n}\int_{\mathbb{R}^n} \frac{\cos(\theta)}{\rho c}(\tilde{p}_z^+ - \tilde{p}_z^-)e^{-i\boldsymbol{k}\cdot\boldsymbol{x}}\mathrm{d}\boldsymbol{k}. \tag{3.10}$$

We are only interested in the wavefield at a given spatial location $\boldsymbol{x}_0$. $\tilde{p}$ in relation to $p(\boldsymbol{x}_0, t)$ consists of two components:

$$\tilde{p} = \tilde{p}_0 + \tilde{p}_1. \tag{3.11}$$

Here $\tilde{p}_0$ and $\tilde{p}_1$ are defined such that the effective contributing component of $\tilde{p}$ at $\boldsymbol{x}_0$ is $\tilde{p}_0$, as opposed to $\tilde{p}_1$, which does not contribute. Hence the inverse wavenumber transform of $\tilde{p}_1$ at $\boldsymbol{x}_0$ is zero:

$$\frac{1}{(2\pi)^n}\int_{\mathbb{R}^n} \tilde{p}_1 e^{-i\boldsymbol{k}\cdot\boldsymbol{x}_0}\mathrm{d}\boldsymbol{k} = 0. \tag{3.12}$$

The associated particle velocity is zero as well. This indirectly implies that $\tilde{p}_0$ may have wavenumber components in it that do not contribute to $p(\boldsymbol{x}_0, t)$, but contribute to to $v_z(\boldsymbol{x}_0, t)$ and vice versa. The subscript 1 only denotes those components that do not contribute to either field.

We can now write $\tilde{p} = \tilde{p}_0$ in Equations 3.8 and 3.9, which comprises of the effective contributing components of $\tilde{p}_z^+$ and $\tilde{p}_z^-$, $\tilde{p}_{z,0}^+$ and $\tilde{p}_{z,0}^-$ respectively:

$$p(\boldsymbol{x}_0, t) = \frac{1}{(2\pi)^n}\int_{\mathbb{R}^n} \tilde{p}_0 e^{-i\boldsymbol{k}\cdot\boldsymbol{x}_0}\mathrm{d}\boldsymbol{k} = \frac{1}{(2\pi)^n}\int_{\mathbb{R}^n} (\tilde{p}_{z,0}^+ + \tilde{p}_{z,0}^-)e^{-i\boldsymbol{k}\cdot\boldsymbol{x}_0}\mathrm{d}\boldsymbol{k}, \tag{3.13}$$

$$v_z(\boldsymbol{x}_0,t)=\frac{1}{(2\pi)^n}\int_{\mathbb{R}^n}\tilde{v}_{z,0}e^{-i\boldsymbol{k}\cdot\boldsymbol{x}_0}\mathrm{d}\boldsymbol{k}=\frac{1}{(2\pi)^n}\int_{\mathbb{R}^n}\frac{\cos(\theta)}{\rho c}(\tilde{p}^+_{z,0}-\tilde{p}^-_{z,0})e^{-i\boldsymbol{k}\cdot\boldsymbol{x}_0}\mathrm{d}\boldsymbol{k}. \tag{3.14}$$

We now need to assume that waves do not interfere at $\boldsymbol{x}_0$, i.e. there is only a single event at $\boldsymbol{x}_0$. This means two things:

1. All waves at $\boldsymbol{x}_0$ travel with the angle θ_0 with respect to the z direction.
2. All waves at $\boldsymbol{x}_0$ travel either in the positive z direction or the negative z direction.

These assumptions effectively mean that in the space-time domain the wavefield at a given point only corresponds to a single event, which, as such, is free of interference. Additionally note that these assumptions are needed to guarantee that the Poynting vector points in the wave-travel direction. If either assumption is invalidated, the Poynting vector may well point in a totally different direction.

The first assumption allows us to pull the fraction in Equation 3.14 out of the integral:

$$v_z(\boldsymbol{x}_0,t)=\frac{1}{(2\pi)^n}\int_{\mathbb{R}^n}\tilde{v}_{z,0}e^{-i\boldsymbol{k}\cdot\boldsymbol{x}_0}\mathrm{d}\boldsymbol{k}=\frac{\cos(\theta_0)}{\rho c}\frac{1}{(2\pi)^n}\int_{\mathbb{R}^n}(\tilde{p}^+_{z,0}-\tilde{p}^-_{z,0})e^{-i\boldsymbol{k}\cdot\boldsymbol{x}_0}\mathrm{d}\boldsymbol{k} \tag{3.15}$$

The second assumption means that either $\tilde{p}^+_z=0$ or $\tilde{p}^-_z=0$. This leads to the following. For $p^-_z(\boldsymbol{x}_0)=0$ Equation 3.15 becomes:

$$\begin{aligned}v^+_{z,0}(\boldsymbol{x}_0,t)&=\frac{\cos(\theta_0)}{\rho c}\frac{1}{(2\pi)^n}\int_{\mathbb{R}^n}\tilde{p}^+_{z,0}e^{-i\boldsymbol{k}\cdot\boldsymbol{x}_0}\mathrm{d}\boldsymbol{k},\\&=\frac{\cos(\theta_0)}{\rho c}p^+_z(\boldsymbol{x}_0),\end{aligned} \tag{3.16}$$

where p^+_z is the inverse Fourier transform $\tilde{p}^+_z(\boldsymbol{x}_0)$.

Equivalently for $p^-_z(\boldsymbol{x}_0)=0$:

$$\begin{aligned}v^-_{z,0}(\boldsymbol{x}_0,t)&=-\frac{\cos(\theta_0)}{\rho c}\frac{1}{(2\pi)^n}\int_{\mathbb{R}^n}\tilde{p}^-_{z,0}e^{-i\boldsymbol{k}\cdot\boldsymbol{x}_0}\mathrm{d}\boldsymbol{k},\\&=-\frac{\cos(\theta_0)}{\rho c}p^-_z(\boldsymbol{x}_0).\end{aligned} \tag{3.17}$$

Since the fractions in Equations 3.16 and 3.17 are always positive we can find the same wavenumber-domain signum and amplitude relations in the space domain, under the two assumptions above, i.e.:

$$\operatorname{sgn}(p^+_{z,0})=\operatorname{sgn}(v^+_{z,0}), \tag{3.18}$$

$$\operatorname{sgn}(p^-_{z,0})=-\operatorname{sgn}(v^-_{z,0}), \tag{3.19}$$

$$|p_0|=\frac{\rho c}{\cos(\theta_0)}|v_{z,0}|. \tag{3.20}$$

FORMULATING POYNTING DECOMPOSITION

From our definition of p as the sum of p^+_z and p^-_z, see Equation 3.8, which we can write mathematically as:

$$p=p^+_z+p^-_z, \tag{3.21}$$

and our definition of v_z, see Equation 3.15, as the sum of v_z^+ and v_z^-, it follows using our single-angle assumption, using Equations 3.18–3.20, that:

$$v_z = v_z^+ + v_z^- = \frac{\cos(\theta)}{\rho c}\left(p_z^+ - p_z^-\right), \tag{3.22}$$

where θ now represents the local unique travel-direction angle. Solving Equations 3.21 and 3.22 for p_z^+ and p_z^- in matrix-vector we find:

$$\begin{pmatrix} p_z^+ \\ p_z^- \end{pmatrix} = \frac{1}{2}\begin{pmatrix} 1 & 1 \\ 1 & -1 \end{pmatrix}\begin{pmatrix} p \\ \frac{\rho c}{\cos(\theta)} v_z \end{pmatrix}. \tag{3.23}$$

We can use Equations 3.18–3.20 to rewrite Equation 3.23 as:

$$\begin{pmatrix} p_z^+ \\ p_z^- \end{pmatrix} = \frac{1}{2}\begin{pmatrix} \mathrm{sgn}(p) + \mathrm{sgn}(v_z) \\ \mathrm{sgn}(p) - \mathrm{sgn}(v_z) \end{pmatrix} |p|, \tag{3.24}$$

$$= \frac{1}{2}\begin{pmatrix} 1 + \frac{\mathrm{sgn}(v_z)}{\mathrm{sgn}(p)} \\ 1 - \frac{\mathrm{sgn}(v_z)}{\mathrm{sgn}(p)} \end{pmatrix} p. \tag{3.25}$$

To further simplify this we need to additionally assume that the wavefields are all real in the space domain, an acceptable assumption as all physical acoustic wavefields are real in the space-time domain. This allows us to use:

$$\frac{1}{2}\left(1 \pm \frac{\mathrm{sgn}(a)}{\mathrm{sgn}(b)}\right) = h(\pm ab) \quad \text{for } b \neq 0, \tag{3.26}$$

where a, b are real, to write Equation 3.24 as Equation 3.1, completing the derivation.

We have now derived Equation 3.1 in the context of acoustic snapshot directional wavefield decomposition. In order to get there, we needed the two assumptions stated before. If either of these assumptions are invalidated the decomposition is no longer guaranteed to be exact. The method nevertheless often works correctly for labelling the wavefield according to the travel direction of the locally dominant wavefield. In acoustics this is often the direct wave close to the source when it is present.

Note that this decomposition can be formulated in terms of piecewise-continuous media allowing this decomposition to still be valid in heterogeneous media, something that is not properly treated in the current formulation of snapshot acoustic directional wavefield decomposition.

3.3. PLANE-WAVE DECOMPOSITION

Plane-wave decomposition is a significant improvement over Poynting decomposition, however, this comes at the cost that the decomposition is no longer local as it has to be computed in the wavenumber-frequency domain. It was originally developed as contour-slicing by Suprajitno and Greenhalgh (1985) to decompose vertical borehole data from Vertical Seismic Profiles (VSP). Given a vertical array of receivers one can transform the recorded wavefield to the vertical wavenumber-angular frequency domain. Although technically only a vertical Fourier transform is necessary for this directional decomposition technique the following derivation will be in the full wavenumber domain for consistent notation.

As this directional decomposition occurs in the frequency domain, it is pertinent to define the forward temporal Fourier transform from the time domain (t) to the angular-frequency domain (ω):

$$\hat{f}(\boldsymbol{x},\omega) = \int_{\mathbb{R}} f(\boldsymbol{x},t)e^{-i\omega t}\mathrm{d}t, \tag{3.27}$$

where quantities in the angular-frequency domain are indicated by caret, or circumflex, hats. The corresponding inverse temporal Fourier transform is defined as:

$$f(\boldsymbol{x},t) = \frac{1}{2\pi}\int_{\mathbb{R}} \hat{f}(\boldsymbol{x},\omega)e^{i\omega t}\mathrm{d}\omega. \tag{3.28}$$

Suprajitno and Greenhalgh (1985) found for a homogeneous medium that waves that travelled in the positive vertical direction mapped to the quadrants where $\omega k_z > 0$ and waves travelling in the opposite direction mapped to $\omega k_z < 0$. Waves travelling orthogonally to the recording surface map to where $\omega k_z = 0$.

Suprajitno and Greenhalgh (1985) then proposed to decompose interfering waves inside a homogeneous medium by muting the undesired quadrants as follows:

$$\begin{pmatrix}\hat{\hat{f}}^{+}\\ \hat{\hat{f}}^{-}\end{pmatrix} = \begin{pmatrix}h(\ \omega k_z)\\ h(-\omega k_z)\end{pmatrix}\hat{\hat{f}}, \tag{3.29}$$

where f is a wavefield, not necessarily the pressure, as this method works for any wave equation. Note that orthogonally travelling waves are again separated in equal parts between the + and − fields. To extend this to directional decomposition one simply rotates the recording surface to record along the desired decomposition direction.

The major advantage of plane-wave decomposition is that it only requires one component of a wavefield. Furthermore, this method can decompose interfering wavefields according to their direction of propagation along a given flat surface. However, due to the involved Fourier transforms, it is more complex than Poynting decomposition and is still only strictly valid for homogeneous media, although it also works reasonably well for heterogeneous media.

We now want to derive this decomposition technique in terms of acoustic snapshot directional wavefield decomposition. To do this we return to Equation 2.7 and transform it to the angular-frequency domain:

$$\omega^2\hat{\hat{p}} = c^2\boldsymbol{k}\cdot\boldsymbol{k}\hat{\hat{p}}. \tag{3.30}$$

A non-trivial solution for ω to this equation is the acoustic dispersion relation:

$$|\omega| = c|\boldsymbol{k}|. \tag{3.31}$$

We judicially choose here to use the positive version of this equation. If the negative version is used then the decomposition directions would be negated, i.e. + would become − and vice versa for −. We now insert the positive version of Equation 3.31 into the temporal Fourier transforms of Equations 2.15 and 2.16 to find:

$$\begin{pmatrix}\hat{\hat{p}}_z^{+}\\ \hat{\hat{p}}_z^{-}\end{pmatrix} = \frac{1}{2}\begin{pmatrix}1 & \rho\frac{|\omega|}{|k_z|}\\ 1 & -\rho\frac{|\omega|}{|k_z|}\end{pmatrix}\begin{pmatrix}\hat{\hat{p}}\\ \hat{\hat{v}}_z\end{pmatrix}. \tag{3.32}$$

Noting that we can write the magnitude of a quantity in terms of its sign times the quantity itself we can rearrange Equation 3.32 to find:

$$\begin{pmatrix}\hat{\hat{p}}_z^+\\ \hat{\hat{p}}_z^-\end{pmatrix} = \frac{1}{2}\begin{pmatrix}1 & \frac{\mathrm{sgn}(\omega)}{\mathrm{sgn}(k_z)}\\ 1 & -\frac{\mathrm{sgn}(\omega)}{\mathrm{sgn}(k_z)}\end{pmatrix}\begin{pmatrix}\hat{\hat{p}}\\ \rho\frac{\omega}{k_z}\hat{\hat{v}}_z\end{pmatrix}. \tag{3.33}$$

To rewrite this we transform Equation 2.5 to the frequency domain and solve for the pressure in terms of the vertical particle velocity:

$$\hat{\hat{p}} = \rho\frac{\omega}{k_z}\hat{\hat{v}}_z, \tag{3.34}$$

where again horizontally travelling waves, corresponding to $k_z = 0$, are not treated properly.

Inserting Equation 3.34 into 3.33 and multiplying the denominators and numerators by their corresponding denominators, noting that we do not properly treat the case where the denominator is zero, we find:

$$\begin{pmatrix}\hat{\hat{p}}_z^+\\ \hat{\hat{p}}_z^-\end{pmatrix} = \frac{1}{2}\begin{pmatrix}1 & \mathrm{sgn}(\omega)\,\mathrm{sgn}(k_z)\\ 1 & -\mathrm{sgn}(\omega)\,\mathrm{sgn}(k_z)\end{pmatrix}\begin{pmatrix}1\\ 1\end{pmatrix}\hat{\hat{p}} = \frac{1}{2}\begin{pmatrix}1 & \mathrm{sgn}(\omega k_z)\\ 1 & -\mathrm{sgn}(\omega k_z)\end{pmatrix}\begin{pmatrix}1\\ 1\end{pmatrix}\hat{\hat{p}}. \tag{3.35}$$

Solving the vector matrix multiplication and using Equation 3.26 we then find:

$$\begin{pmatrix}\hat{\hat{p}}_z^+\\ \hat{\hat{p}}_z^-\end{pmatrix} = \frac{1}{2}\begin{pmatrix}1+\mathrm{sgn}(\omega k_z)\\ 1-\mathrm{sgn}(\omega k_z)\end{pmatrix}\hat{\hat{p}} = \begin{pmatrix}h(\ \omega k_z)\\ h(-\omega k_z)\end{pmatrix}\hat{\hat{p}}. \tag{3.36}$$

We have now derived plane-wave decomposition in the context of acoustic snapshot directional wavefield decomposition and have shown that they are the same, except for waves travelling orthogonally to the z direction. These two decomposition schemes achieve the same result but in different domains. Plane-wave decomposition works in the (ω, k_z) domain while snapshot decomposition works in the wavenumber domain. Note that the derivation in terms of particle-velocity normalized directional wavefield decomposition is nearly identical and will not be repeated here.

Finally note that this method can only decompose wavefields according to the direction in which the Fourier transform is taken. If the Fourier transform is taken in the z direction, decomposition can only be in the z direction. If decomposition in another direction is desired, either the spatial Fourier transform has to be taken in that direction or additional wavefield components, like a component of the particle velocity vector, are necessary.

3.4. ANALYTIC DECOMPOSITION

An inherent limitation of plane-wave decomposition is the fact that it operates in the frequency domain. This is a major problem for decomposition while modelling using time-stepping operators. To accomodate for this, alternatives were sought that would work on snapshots of a wavefield. An effective option for real wavefields is to use analytic sources, as was originally proposed by Shen and Albertin (2015). The basic idea is to

rewrite Equation 3.35 as:

$$\begin{pmatrix} \hat{\hat{p}}_z^+ \\ \hat{\hat{p}}_z^- \end{pmatrix} = \frac{1}{2}\begin{pmatrix} 1 & i\,\mathrm{sgn}(k_z) \\ 1 & -i\,\mathrm{sgn}(k_z) \end{pmatrix}\begin{pmatrix} 1 \\ -i\,\mathrm{sgn}(\omega) \end{pmatrix}\hat{\hat{p}}. \tag{3.37}$$

The $-i\,\mathrm{sgn}(\omega)\,\hat{\hat{p}}$ corresponds to the temporal Hilbert transform of the pressure. This can be computed by forward modelling the Hilbert transform of the source signature. Multiplying with $i\,\mathrm{sgn}(k_z)$ in the wavenumber domain corresponds to the z Hilbert transform in the space domain. This allows us to write Equation 3.37 in the space-time domain as:

$$\begin{pmatrix} p_z^+ \\ p_z^- \end{pmatrix} = \frac{1}{2}\begin{pmatrix} 1 & \mathscr{H}_z \\ 1 & -\mathscr{H}_z \end{pmatrix}\begin{pmatrix} 1 \\ \mathscr{H}_t \end{pmatrix} p, \tag{3.38}$$

where $\mathscr{H}_z$ and $\mathscr{H}_t$ are the z and temporal Hilbert transform operators respectively. This decomposition operation can be made to work on snapshots of wavefields as $\mathscr{H}_t p$ can be computed by forward modelling the temporal Hilbert transforms of the source signatures.

We are, however, not yet talking about analytic wavefields. We now assume that the wavefields are real. Knowing that the acoustic wave equation also supports complex wavefields and does so by independently treating the real and imaginary components, we are left with a zero imaginary component of the wavefield at our disposal. If we use the zero imaginary component to store the temporal Hilbert transform of our wavefield, which is always real given a real source signature, we construct analytic wavefields, denoted with a bar over the symbol:

$$\bar{p} = p + i\mathscr{H}_t p. \tag{3.39}$$

$\bar{p}$ is now an analytic wavefield that can be found using analytic sources. Casting Equation 3.38 in terms of it we find:

$$\begin{pmatrix} p_z^+ \\ p_z^- \end{pmatrix} = \frac{1}{2}\begin{pmatrix} 1 & \mathscr{H}_z \\ 1 & -\mathscr{H}_z \end{pmatrix}\begin{pmatrix} \Re \\ \Im \end{pmatrix}\bar{p}, \tag{3.40}$$

where $\Re$ and $\Im$ are the real and imaginary operators that return the real and imaginary components of a complex number respectively.

We have now established an alternative method to decompose wavefields at an instance in time based on analytic wavefields, due to analytic sources. The disadvantage with this method is that it only works for purely real, or purely imaginary, original wavefields. Furthermore the analytic wavefield must be modelled based on analytic sources. As the acoustic wave equation can be used to forward model the real and imaginary components of a wavefield independently, this effectively corresponds to twice the amount of work as modelling a real wavefield. Computing two wavefields, or a complex wavefield, requires twice the amount of memory required to forward model one real, or one imaginray, component of a wavefield. The z Hilbert transform, however, is more compute time efficient when compared to snapshot directional wavefield decomposition as it is faster than a full wavenumber domain Fourier transform. This advantage is lost if the directional decomposition occurs in many different directions as one Hilbert transform per direction of interest is then necessary. At this point computing the transform to the full wavenumber domain is often faster. When numerically implementing complex acoustic

wave-equation modelling software on current compute hardware, care needs to be taken to ensure that the modelling is as fast, if not faster, than modelling the real and imaginary components separately.

This type of decomposition is also less flexible than snapshot directional wavefield decomposition when decomposing snapshots during acoustic modelling, as the choice has to be made at the start of modelling whether to compute the analytic wavefield. Snapshot directional wavefield decomposition can be used at any time, even after a modelling job is finished, given sufficient wavefield snapshots.

3.5. SURFACE-NORMAL DIRECTIONAL WAVEFIELD DECOMPOSITION

Surface-normal decomposition is a direct alternative to snapshot directional wavefield decomposition. It is intended for decomposing wavefields recorded on a surface, generally horizontal, into waves leaving this surface and waves entering this surface. It is the prototype decomposition on which snapshot directional wavefield decomposition is based. For a good overview of the technique see Ursin (1983).

Like snapshot directional wavefield decomposition this method is effectuated by the scaled addition of wavefield components. The difference is the form the acoustic wave equation takes after decomposition. For acoustic snapshot wavefield decomposition we rewrite the acoustic wave equation in terms of the time derivative of the wavefields on the left-hand side, see Equation 2.17. For surface-normal directional wavefield decomposition the acoustic wave equation is written in terms of the derivative in the decomposition direction. Furthermore the decomposition occurs in the domain defined by the frequency and the wavenumbers orthogonal to the decomposition direction, not the full wavenumber domain.

To interrelate acoustic snapshot directional wavefield decomposition and surface-normal directional wavefield decomposition we need to invoke the square of the acoustic dispersion relation, Equation 3.31:

$$\omega^2 = c^2 \boldsymbol{k} \cdot \boldsymbol{k}. \tag{3.41}$$

Solving this for $|k_z|$ we find:

$$|k_z| = \left| \sqrt{\left(\frac{\omega}{c}\right)^2 - \boldsymbol{k}_O \cdot \boldsymbol{k}_O} \right| = |\mathscr{K}_z|. \tag{3.42}$$

where $\mathscr{K}_z$ is the square root of the Helmholtz operator in the $\boldsymbol{k}_O$-plane. It is defined according to Wapenaar and Berkhout (1989) as:

$$\mathscr{K}_z = \begin{cases} \operatorname{sgn}(\omega) \sqrt[+]{\left(\frac{\omega}{c}\right)^2 - \boldsymbol{k}_O \cdot \boldsymbol{k}_O} & \text{if } \left(\frac{\omega}{c}\right)^2 \geq \boldsymbol{k}_O \cdot \boldsymbol{k}_O \text{ and } \omega, c, \boldsymbol{k}_O \cdot \boldsymbol{k}_O \in \mathbb{R}, \\ -i \sqrt[+]{\boldsymbol{k}_O \cdot \boldsymbol{k}_O - \left(\frac{\omega}{c}\right)^2} & \text{if } \left(\frac{\omega}{c}\right)^2 < \boldsymbol{k}_O \cdot \boldsymbol{k}_O \text{ and } \omega, c, \boldsymbol{k}_O \cdot \boldsymbol{k}_O \in \mathbb{R}. \end{cases} \tag{3.43}$$

where $\boldsymbol{k}_O$ is the vector of orthogonal wavenumbers to k_z and the + superscript of the square root indicates that the positive branch of the square root is chosen, i.e. the positive

root. Note that in Wapenaar and Berkhout (1989) only postive angular frequencies are considered, hence in their expressions the $\text{sgn}(\omega)$ is omitted.

We must now note that the derivations in Chapter 2 only hold for propagating waves, they are not correct for evanescent waves. To properly account for evanescent waves we need to realize that Chapter 2 only considered real values of k_z. As such, all the $|k_z|$ in Chapter 2 should be mathematically rigorously written as:

$$|k_z| \Rightarrow \sqrt{k_z^2} \tag{3.44}$$

The dispersion relation, Equation 3.41, however, also admits complex values of k_z. Equation 3.43 restricts itself to real and imaginary values of k_z. More generally, if the quantity under the square root is complex then the root should be chosen to lie in the negative k_z complex plane.

With the correct extension of $|k_z|$ to the complex k_z plane in the frequency-wavenumber domain we find:

$$|k_z| \Rightarrow \sqrt{k_z^2} \Rightarrow \text{sgn}(\omega)\mathcal{K}_z. \tag{3.45}$$

Inserting Equation 3.45 into 3.32 we find:

$$\begin{pmatrix} \hat{\hat{p}}_z^+ \\ \hat{\hat{p}}_z^- \end{pmatrix} = \frac{1}{2}\begin{pmatrix} 1 & \rho\frac{\omega}{\mathcal{K}_z} \\ 1 & -\rho\frac{\omega}{\mathcal{K}_z} \end{pmatrix}\begin{pmatrix} \hat{\hat{p}} \\ \hat{\hat{v}}_z \end{pmatrix}, \tag{3.46}$$

which is the expression given in Wapenaar and Berkhout (1989).

As the matrix in Equation 3.46 is now independent of k_z the equation can be inverse Fourier transformed along the k_z direction to find a decomposition operator that works in the z domain. This is why this type of decomposition is used to directionally decompose recorded data on a horizontal surface into up- and down-going waves.

Like plane-wave decomposition this method is suboptimal for decomposing acoustic wavefields at a given instance in time. It is, however, ideal for decomposing recorded data due to the common practice of acquiring data using arrays of recording instruments on a surface that record a wavefield over time. Furthermore, it is very mature and standard practice in the seismic industry when directionally decomposing recorded data. It is also exact for media with variations in medium parameters in the z direction, and can be extended to take into account laterally varying media, see Grimbergen et al. (1998).

As a final note recall that Equation 3.46 correctly decomposes both propagating and evanescent waves. Snapshot wavefield decomposition, like the other presented methods, does not, it only correctly decomposes propagating waves. More generally, snapshot decomposition needs to be extended to properly take into account evanescent waves. This is done in Chapter 4 for a theoretical example. Snapshot wavefield decomposition, however, is the only method to properly handle propagating waves travelling orthogonally to the z direction.

3.6. TWO LAYER MODEL: COMPARISON OF METHODS

To illustrate snapshot wavefield decomposition in the context of the other snapshot decomposition schemes consider a medium with one interface, with a source above it, as shown in Figure 3.1. Figure 3.1 compares the various decomposition schemes for

down-going waves. Figure 3.1c) shows four summed pressure snapshots at 0.1 to 0.4 s of an acoustic wavefield due to a 50 Hz-peak-frequency Ricker-wavelet volume-injection source at the surface, 250 m above an interface at which the velocity increases from 1 to 2 km s^{-1}, in a 500 by 500 m acoustic model, discretized every meter, with absorbing boundaries on all sides. The wavefield corresponding to Figure 3.1c) was decomposed using Poynting decomposition (a), plane wave decomposition (b), surface-normal (d) and snapshot decomposition (e).

Figure 3.1a) shows that Poynting decomposition fails for the interfering waves just above the interface, visible inside the green spyglass. Figure 3.1b), corresponding to plane wave decomposition (Suprajitno and Greenhalgh, 1985), is not completely correct either. Where the wavefield interacts with the interface or model boundaries, vertical stripes form over the entire panel with diminishing amplitudes. These are due to aliasing in the wavenumber domain as the employed discrete Fourier transform is circular and the wavefield is not sufficiently well sampled to resolve the resultant sharp contrasts in pressure amplitude. This necessitated double sided tapering in time and the vertical space dimension using a 51-point sine-squared taper from 0 to 1, before applying the necessary two-dimensional Fourier transforms. Figure 3.1d) shows the surface-normal decomposed result, which is a considerable improvement over plane-wave decomposition. There is some visible leakage of the up-going wavefield above the interface though and as the wavefield operates in the Fourier domain it also required tapering. Figure 3.1e) shows the snapshot decomposed result, which features improved event continuity, compare especially the green spyglasses, at the cost of slightly anomalous amplitudes just below the interface, the difference to the exact amplitudes however is so small that it cannot be perceivably captured by the employed colourmap. The additional cyan spyglass in Figures 3.1b), 3.1d) and 3.1e) shows that decomposition methods do not perfectly decompose interfering waves, but that they also do not suffer from the plane-wave striping artefacts in the plane-wave decomposed result, Figure 3.1b). Overall snapshot decomposition performs the best in this example.

3.7. DISCUSSION & CONCLUSIONS

We have related acoustic snapshot directional wavefield decomposition to common wavefield decomposition schemes and derived them in the context of snapshot directional wavefield decomposition. As all of these schemes can be derived in terms of each other and are thus mutually related. They are just different ways of expressing the same operation. This is important as it allows us to choose the scheme tailored to our problem, see Table 3.1. If we only have the pressure and the particle velocity in our desired decomposition direction, then we can use Poynting decomposition to approximately determine the travel direction of the wavefield. If we had an array of time recordings in our desired decomposition direction we would use plane-wave decomposition. If instead the array of recordings was normal to our desired recording direction then we would use surface-normal decomposition. And finally snapshot directional wavefield decomposition can be used for any decomposition direction as long as the wavefield is known everywhere in space. We have now demonstrated acoustic snapshot directional wavefield decomposition in the context of existing directional wavefield decomposition schemes and its ability to surpass other schemes in its ideal area of application, i.e., on snapshots.

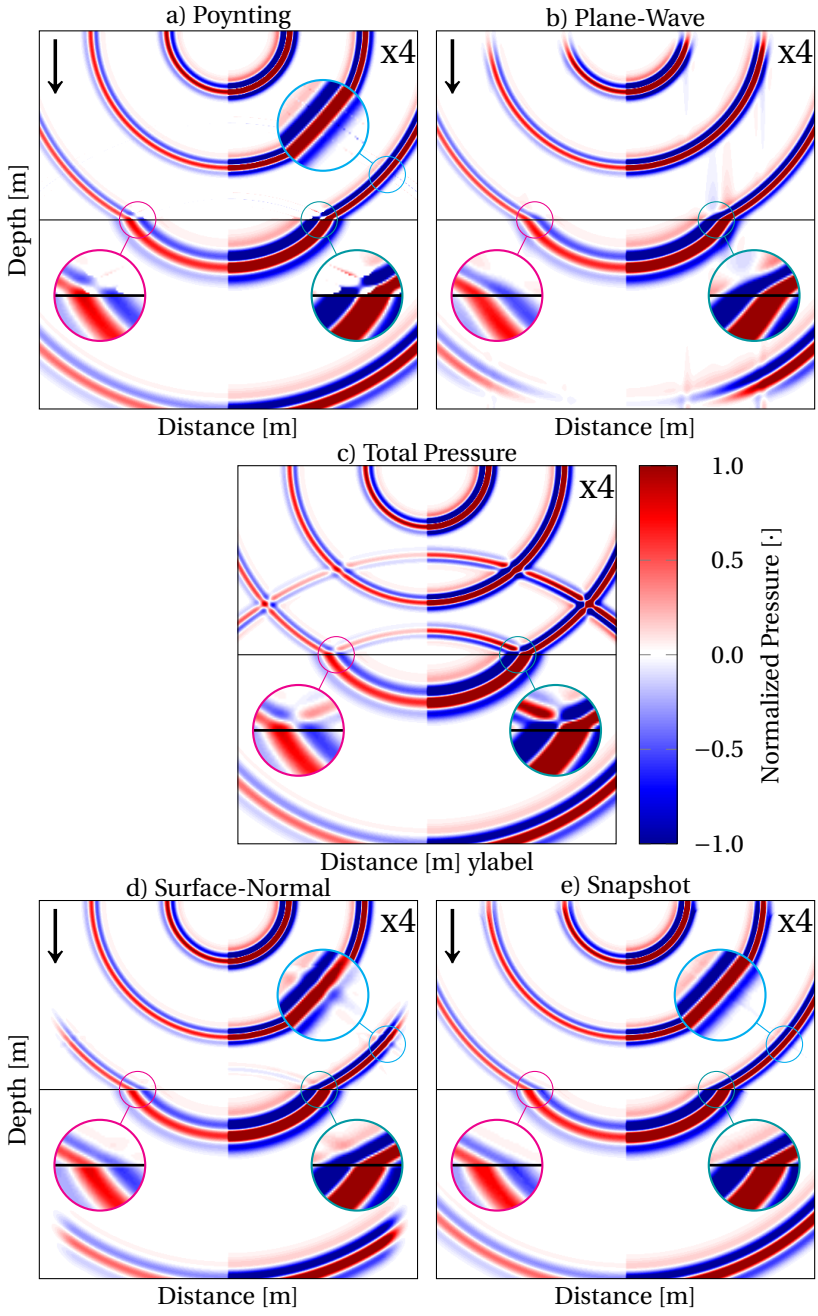

Figure 3.1: Comparison of different wavefield decomposition techniques applicable to RTM for the down-going wavefield. The right-hand-side amplitudes of each figure are exaggerated by a factor of four.

Decomposition Method	Poynting	Plane-Wave	Analytic	Snapshot	Surface Normal
Decomposition	no, labelling	yes	yes	yes	yes
Domain	(x, y, z, t)	(x, y, k_z, ω)	(x, y, k_z, t)	(k_x, k_y, k_z, t)	(k_x, k_y, z, ω)
Decomposition direction	arbitrary	z direction	z direction	arbitrary	z direction
Required components	p and v_z	only p	p and $\mathscr{H}_t\{p\}$	p and v_z or $\partial_t p$	p and v_z or $\partial_z p$
Additional wavefield	no	no	yes	no	no
Medium assumption	t–$\boldsymbol{x}$ invariant	t–$\boldsymbol{x}$ invariant	$\boldsymbol{x}$ invariant	$\boldsymbol{x}$ invariant	t invariant
Classical seismic applications	RTM	VSP	RTM	RTM	de-ghosting, redatuming, migration

Table 3.1: Comparison of the different decomposition techniques according to: (1) whether they actually directionally decompose the wavefield, (2) their domain of operation, (3) the decomposition direction, (4) which wavefield components are needed, (5) whether additional wavefields need to be modelled, (6) assumptions about the medium and (7) what are the classical domains of application in seismology. Note VSP stands for Vertical Seismic Profile and de-ghosting is a processing step by which wavefields that enter a medium of interest from outside are removed from the data.

It should be noted that this is not a complete discussion of the various decomposition techniques in the literature. A noteworthy space-time technique that is explicitly designed for wavefields modelled using finite-difference techniques is presented in Amundsen and Robertsson (2014) and Robertsson et al. (2015). Through the use or absence of perfectly reflecting surfaces above recording depth levels in conjunction with the injection of recorded wavefields at the depth the directional separation of wavefields at the injection surface can be achieved achieved. Under the right configurations this allows for the injection of a purely down-going wavefields that, for example, either include or exclude sea-surface–related multiple reflections.

This technique is very interesting as it is the only technique to properly decompose wavefields in the time-space domain in a finite-difference sense. This makes it relevant for many imaging applications, like reverse time migration, see Amundsen and Robertsson (2014), or the decomposition of elastic wavefields, Robertsson et al. (2015). A more thorough investigation of this technique, however, was beyond the scope of this work.

4

Directional Decomposition Applied To Plane Waves

Here we will demonstrate with two simple plane-wave examples how the snapsot directional wavefield decomposition proposed in Chapter 2 behaves for propagating and evanescent waves, where the decomposition breaks down for evanescent waves without the proper extension of the decomposition operator into the complex wavenumber plane. This chapter differs from the previous two in that concrete examples will be considered here. We will begin by looking at two interfering propagating waves that travel in opposite z directions and use directional wavefield decomposition to separate them. Then we consider an evanescent wavefield due to a flat source plane, which exhibits exponentially decaying amplitudes normal to the source plane. We decompose the wavefield according to the direction of amplitude decay by correctly accounting for its non-analytic behaviour in the complex wavenumber domain. This wavefield in the context of the acoustic dispersion relation has complex wavenumbers.

4.1. INTRODUCTION TO PLANE WAVES

Before directionally decomposing plane waves we will first formally introduce them. We consider how unit-amplitude plane-wave solutions to the acoustic wave equation in a homogeneous medium in three spatial dimensions, (x, y, z) and one temporal dimension (t) behave. For convenience we insert the linearised equation of motion, Equation 2.2, into the linearised equation of continuity, Equation 2.1, and assume that the medium is lossless, isotropic and homogeneous to find the pressure acoustic wave equation:

$$\partial_t^2 p = c^2 \Delta p. \tag{4.1}$$

where $\Delta = \boldsymbol{\nabla} \cdot \boldsymbol{\nabla}$ denotes the Laplacian. Monochromatic plane-wave pressure solutions to the acoustic wave equation, Equation 4.1, can be written as:

$$p(x, y, z, t) = e^{i\omega_0 (t - \boldsymbol{s} \cdot \boldsymbol{x})}, \tag{4.2}$$

where ω_0 is the real time- and space-invariant scalar angular frequency of the wave and $\boldsymbol{s}$ is the vector of time- and space-invariant scalar slowness of the plane wave in the x, y, and z directions:

$$\boldsymbol{s} = \begin{pmatrix} s_x \\ s_y \\ s_z \end{pmatrix}. \tag{4.3}$$

Inserting Equation 4.2 into 4.1 and solving for the pressure on the left-hand side we find:

$$p = c^2 (\boldsymbol{s} \cdot \boldsymbol{s}) p. \tag{4.4}$$

The non-trivial solution to this states:

$$\boldsymbol{s} \cdot \boldsymbol{s} = \frac{1}{c^2} = s_x^2 + s_y^2 + s_z^2. \tag{4.5}$$

This equation is satisfied for both real and imaginary values of $\boldsymbol{s}$. Since we only consider real values for ω_0, as complex values of ω_0 lead to temporal evanescence, which is not considered, $\boldsymbol{s}$ cannot be purely imaginary.

Purely propagating waves occur when $\boldsymbol{s}$ is purely real, while spatially evanescent waves occur when one or more components of $\boldsymbol{s}$ are imaginary. The wavefield is then said to be evanescent in these components. Propagating and evanescent waves behave fundamentally different. The amplitude of propagating plane waves in a homogeneous medium is constant, while the amplitudes of evanescent waves in the evanescent directions decay exponentially.

4.2. DECOMPOSITION OF TWO PROPAGATING PLANE WAVES

In this section we aim to directionally separate two real propagating and interfering pressure plane waves along the z axis in the wavenumber-frequency domain. For this we transform the decomposition operator, Equation 2.22, to the wavenumber-frequency domain:

$$\begin{pmatrix} \hat{\hat{p}}_z^+ \\ \hat{\hat{p}}_z^- \end{pmatrix} = \frac{1}{2} \begin{pmatrix} 1 & \rho c \frac{|\boldsymbol{k}|}{|k_z|} \\ 1 & -\rho c \frac{|\boldsymbol{k}|}{|k_z|} \end{pmatrix} \begin{pmatrix} \hat{\hat{p}} \\ \hat{\hat{v}}_z \end{pmatrix}. \tag{4.6}$$

Note that this expression was derived assuming real wavenumbers.

The first plane wave we consider, denoted p_1, has an amplitude a_1, positive angular frequency ω_0, and travels in the direction of $\boldsymbol{s}$, which points in the positive z direction. This means that the s_z component is positive. The second plane wave, p_2 with amplitude a_2 travels in the opposite direction. The sum of these two plane waves gives the total pressure, p:

$$p = \underbrace{a_1 \cos\left(\omega_0 \left[t - \boldsymbol{s}\cdot\boldsymbol{x}\right]\right)}_{p_1} + \underbrace{a_2 \cos\left(\omega_0 \left[t + \boldsymbol{s}\cdot\boldsymbol{x}\right]\right)}_{p_2}. \tag{4.7}$$

We now wish to separate p_1 and p_2, which travel in opposite z directions, using acoustic directional wavefield decomposition.

We can do this in the wavenumber frequency domain using Equation 4.6. For that, though, we need the particle velocity in the z direction, which we can find using the linearised equation of motion, Equation 2.2, and Equation 4.2:

$$v_z = \frac{s_z}{\rho}(p_1 - p_2). \tag{4.8}$$

To be able to use Equation 4.6 in conjunction with Equations 4.7 and 4.8 to separate p_1 and p_2 we need to transform Equations 4.7 and 4.8 to the wavenumber frequency domain. Transforming Equation 4.7 to the wavenumber frequency-domain we find:

$$\hat{\tilde{p}} = \hat{\tilde{p}}_1 + \hat{\tilde{p}}_2, \tag{4.9}$$

where:

$$\hat{\tilde{p}}_1 = \frac{(2\pi)^4}{2} a_1 \left[\delta(\omega + \omega_0, \boldsymbol{k} + \omega_0\boldsymbol{s}) + \delta(\omega - \omega_0, \boldsymbol{k} - \omega_0\boldsymbol{s})\right], \tag{4.10}$$

$$\hat{\tilde{p}}_2 = \frac{(2\pi)^4}{2} a_2 \left[\delta(\omega + \omega_0, \boldsymbol{k} - \omega_0\boldsymbol{s}) + \delta(\omega - \omega_0, \boldsymbol{k} + \omega_0\boldsymbol{s})\right], \tag{4.11}$$

where in this case the multidimensional Dirac delta functions are defined as:

$$\delta(\omega \pm \omega_0, \boldsymbol{k} \pm \omega_0\boldsymbol{s}) = \delta(\omega \pm \omega_0)\delta(k_x \pm \omega_0 s_x)\delta(k_y \pm \omega_0 s_y)\delta(k_z \pm \omega_0 s_z), \tag{4.12}$$

where the signs associated with ω_0 and $\omega_0\boldsymbol{s}$ on the left- and right-hand sides correspond to each other. The corresponding transform of the particle velocity in the z direction is:

$$\hat{\tilde{v}}_z = \frac{s_z}{\rho}\left(\hat{\tilde{p}}_1 - \hat{\tilde{p}}_2\right). \tag{4.13}$$

In preparation for inserting Equations 4.9 and 4.13 into Equation 4.6 we scale Equation 4.13 with the particle-velocity scale factor in Equation 4.6:

$$\rho c \frac{|\boldsymbol{k}|}{|k_z|}\hat{\tilde{v}}_z = s_z c \frac{|\boldsymbol{k}|}{|k_z|}\left(\hat{\tilde{p}}_1 - \hat{\tilde{p}}_2\right). \tag{4.14}$$

Noting that where Equation 4.14 is non-zero the following properties hold:

$$c|\boldsymbol{k}| = |\omega_0|, \tag{4.15}$$

$$|k_z| = |\omega_0 s_z|. \tag{4.16}$$

Equation 4.15 follows from the acoustic dispersion relation $\omega^2 = c^2 \boldsymbol{k} \cdot \boldsymbol{k}$, Equation 3.31. Equation 4.16 is consequence of the fact that k_z is only non-zero at $\pm\omega_0 s_z$, see Equations 4.10–4.12. Since s_z is real and positive, we can use Equations 4.15 and 4.16 to simplify the right-hand side of Equation 4.14 to:

$$\rho c \frac{|\boldsymbol{k}|}{|k_z|} \hat{\hat{v}}_z = \hat{\hat{p}}_1 - \hat{\hat{p}}_2. \tag{4.17}$$

Inserting Equations 4.9 and 4.17 into Equation 4.6 we are able to separate $\hat{\hat{p}}_1$ and $\hat{\hat{p}}_2$ as $\hat{\hat{p}}_z^+$ and $\hat{\hat{p}}_z^-$ respectively:

$$\begin{pmatrix} \hat{\hat{p}}_z^+ \\ \hat{\hat{p}}_z^- \end{pmatrix} = \frac{1}{2} \begin{pmatrix} 1 & 1 \\ 1 & -1 \end{pmatrix} \begin{pmatrix} \hat{\hat{p}}_1 + \hat{\hat{p}}_2 \\ \hat{\hat{p}}_1 - \hat{\hat{p}}_2 \end{pmatrix} = \begin{pmatrix} \hat{\hat{p}}_1 \\ \hat{\hat{p}}_2 \end{pmatrix}. \tag{4.18}$$

Transforming the above back to the space-time domain we find p_1 and p_2, see Equation 4.7. We have now succeeded in separating the plane waves p_1 and p_2 using directional wavefield decomposition in the wavenumber-frequency domain. In the following, we wish to do the same for spatially evanescent waves.

4.3. DECOMPOSITION OF TWO SPATIALLY EVANESCENT WAVES

For spatially evanescent waves, the components of $\boldsymbol{s}$ in Equation 4.2 are complex. For simplicity we assume that only the z component of the slowness vector $\boldsymbol{s}$ is imaginary:

$$s_z = -i\sigma_z, \tag{4.19}$$

where $\sigma_z > 0$ is defined according to:

$$\sigma_z = \sqrt[+]{\boldsymbol{s}_O \cdot \boldsymbol{s}_O - \frac{1}{c^2}} \quad \text{for } \boldsymbol{s}_O \cdot \boldsymbol{s}_O > \frac{1}{c^2}, \tag{4.20}$$

where $\boldsymbol{s}_O$ is the vector of slownesses orthogonal to the z direction:

$$\boldsymbol{s}_O = \begin{pmatrix} s_x \\ s_y \end{pmatrix}. \tag{4.21}$$

We consider the following evanescent plane wave whose amplitude decays exponentially in the evanescent direction but is unitary in the orthogonal directions:

$$p = \cos\left(\omega_0 [\, t - \boldsymbol{s}_O \cdot \boldsymbol{x}_O \,]\right) e^{-\omega_0 \sigma_z |z|}, \tag{4.22}$$

where ω_0 is the real positive angular frequency of the wave and $\boldsymbol{x}_O$ is the location vector orthogonal to the z direction, similar to $\boldsymbol{s}_O$. Furthermore we restrict ourselves to real s_x and s_y. It is also worth mentioning that formally Equation 4.22 is a solution to the acoustic wave equation including sources, see Appendix B.

For $z > 0$ Equation 4.22 is decaying in the positive z direction, while for $z < 0$ it is decaying in the negative z direction. Following Wapenaar and Berkhout (1989), where evanescent waves are decomposed according to the direction they decay in, we can already identify the directionally decomposed wavefields we seek:

$$p_z^+ = h(\ \ z)\, p, \tag{4.23}$$

$$p_z^- = h(-z)\, p. \tag{4.24}$$

Although we can already identify the directionally decomposed wavefields, we want to show that when we substitute the evanescent plane-wave solution, Equation 4.22, into the decomposition equation, Equation 4.6, that these results will come out. So we aim to derive this, which we will do in the following.

For the decomposition we additionally need the z-component of the particle velocity. Inserting the vertically evanescent pressure plane wave, Equation 4.22, into the linearised equation of motion, Equation 2.2, and solving for v_z by integrating in time we find:

$$v_z = \frac{\sigma_z}{\rho}\,[\partial_z|z|]\,\sin\left(\omega_0[\,t - \boldsymbol{s}_O \cdot \boldsymbol{x}_O\,]\right) e^{-\omega_0 \sigma_z |z|}, \tag{4.25}$$

where $\partial_z|z|$, which is undefined at $z = 0$, is to be considered in terms of the theory of distributions.

There is something important to realize concerning Equation 4.25. When comparing Equations 4.22 and 4.25 one can notice that they are out of phase in time and the orthogonal spatial dimensions. In the absence of interfering wavefields this is a common property of evanescent wavefields. For non-interfering propagating wavefields the propagating components of the particle velocity are in phase with each other and the pressure. For evanescent waves the particle-velocity component in the evanescent direction(s) is/are out of phase with respect to the other propagating component(s) of the particle velocity.

Since the decomposition operation, Equation 4.6, is in the wavenumber-frequency domain we need to transform p and v_z, Equations 4.22 and 4.25 respectively, also to that domain:

$$\hat{\tilde{p}} = -\frac{(2\pi)^3}{2}\, i \quad \delta_1(\omega, \boldsymbol{k}_O)\left(\frac{1}{k_z - i\omega_0\sigma_z} - \frac{1}{k_z + i\omega_0\sigma_z}\right), \tag{4.26}$$

$$\hat{\tilde{v}}_z = -\frac{(2\pi)^3}{2}\ \frac{\sigma_z}{\rho}\delta_2(\omega, \boldsymbol{k}_O)\left(\frac{1}{k_z - i\omega_0\sigma_z} + \frac{1}{k_z + i\omega_0\sigma_z}\right), \tag{4.27}$$

where for succinctness we defined:

$$\begin{aligned}\delta_1(\omega, \boldsymbol{k}_O) = \quad & \delta(\omega + \omega_0)\delta(k_x + \omega_0 s_x)\delta(k_y + \omega_0 s_y) \\ & + \delta(\omega - \omega_0)\delta(k_x - \omega_0 s_x)\delta(k_y - \omega_0 s_y),\end{aligned} \tag{4.28}$$

$$\begin{aligned}\delta_2(\omega, \boldsymbol{k}_O) = \quad & \delta(\omega - \omega_0)\delta(k_x - \omega_0 s_x)\delta(k_y - \omega_0 s_y) \\ & - \delta(\omega + \omega_0)\delta(k_x + \omega_0 s_x)\delta(k_y + \omega_0 s_y).\end{aligned} \tag{4.29}$$

We now want to directionally decompose the pressure wavefield, Equation 4.26, to find the following Cauchy principle-value Fourier transforms of of Equations 4.23 and

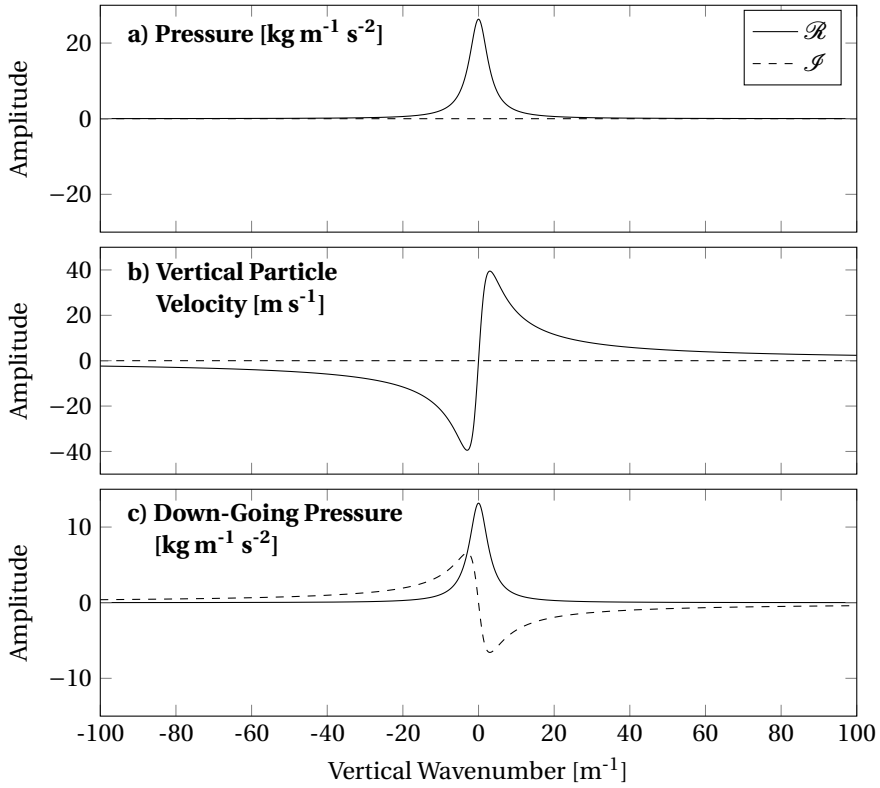

Figure 4.1: Plots of Equations 4.26, 4.27 and 4.30, (a–c) respectively, for $\omega = \omega_0$ and $\boldsymbol{k}_O = \omega_0 \boldsymbol{s}_O$ for $\omega_0 = 1$, $s_x = 5$, $\sigma_z = 3$ and $c = 1/4$. The solid lines denote the real parts while the dashed lines denote the imaginary parts of the plotted functions. The units of the amplitude are included in the subfigure titles.

4.24 to the wavenumber-frequency domain:

$$\hat{\tilde{p}}_z^+ = \frac{(2\pi)^3}{2} i \frac{\delta_1(\omega, \boldsymbol{k}_O)}{k_z + i\omega_0\sigma_z}, \tag{4.30}$$

$$\hat{\tilde{p}}_z^- = -\frac{(2\pi)^3}{2} i \frac{\delta_1(\omega, \boldsymbol{k}_O)}{k_z - i\omega_0\sigma_z}. \tag{4.31}$$

If we now plot $\hat{\tilde{p}}$, $\hat{\tilde{v}}_z$ and $\hat{\tilde{p}}_z^+$, we see a problem. Both the pressure and the z component of the particle velocity are real while the down-going pressue $\hat{\tilde{p}}_z^+$ is complex. With the real particle-velocity scaling operations as presented in Chapter 2 it is impossible to add a real pressure wavefield to a real scaled particle-velocity wavefield and get a complex expression. Evidently snapshot directional wavefield decomposition as presented in Chapter 2 breaks down for evanescent waves.

4.4. NUMERICAL EXAMPLES

We can also numerically show that snapshot directional wavefield decomposition works for evanescent waves. Figure 4.2 shows on the left a propagating wavefield, while on the right it shows a vertically evanescent wavefield that is propagating in the positive horizontal direction. The propagating wave on the left, like the evanescent wave in the previous example, is due to a source plane at $z = 0$. The resultant propagating wavefield can be described using:

$$p = \cos(\omega_0[t - \boldsymbol{s}_O \cdot \boldsymbol{x}_O - s_z|z|]). \tag{4.32}$$

The evanescent wavefield on the right of the figure is defined as in the preceding example.

Figures 4.2a and 4.2b show pressure and associated vertical particle-velocity wavefields. Of special interest here is that for the propagating wavefield the pressure and vertical particle velocity are in phase, while for the evanescent wavefield they are out of phase by a factor of $\pi/2$ in the horizontal direction. This is important because it affects the scaling.

If we now scale the vertical particle velocity, Figure 4.2b, to the pressure, Figure 4.2a, using the operators as presented in Chapter 2 then we find Figure 4.2c. For the propagating wave it is trivial to see that if one adds the scaled particle velocity to the pressure that the top half, i.e. z<0, of the pressure wavefield will cancel out, see Figure 4.2d1. For the evanescent wave this is not the case. Figure 4.2d2 shows the desired result. However, the addition of the pressure, Figure 4.2a2 and the scaled particle velocity, Figure 4.2c2 for the evanescent wave could never result in this wavefield. For the evanescent wave the waves do not properly destructively interfere and the wavefield is non-zero for $z < 0$, demonstrating that snapshot directional wavefield decomposition as presented in Chapter 2 does not work for evanescent waves. We need to take the horizontal phase shift between the pressure and vertical particle velocity into account.

4.5. SUMMARY

The operators as presented in Chapter 2 do not properly directionally decompose evanescent waves. They are only valid for propagating plane waves. In this chapter we have shown that to properly extend the decomposition to work for evanescent waves the phase shift between the pressure and particle velocity needs to be taken into account. How to do this is not understood yet. For that reason in the remainder of this work we will not take evanescent waves into account when decomposing.

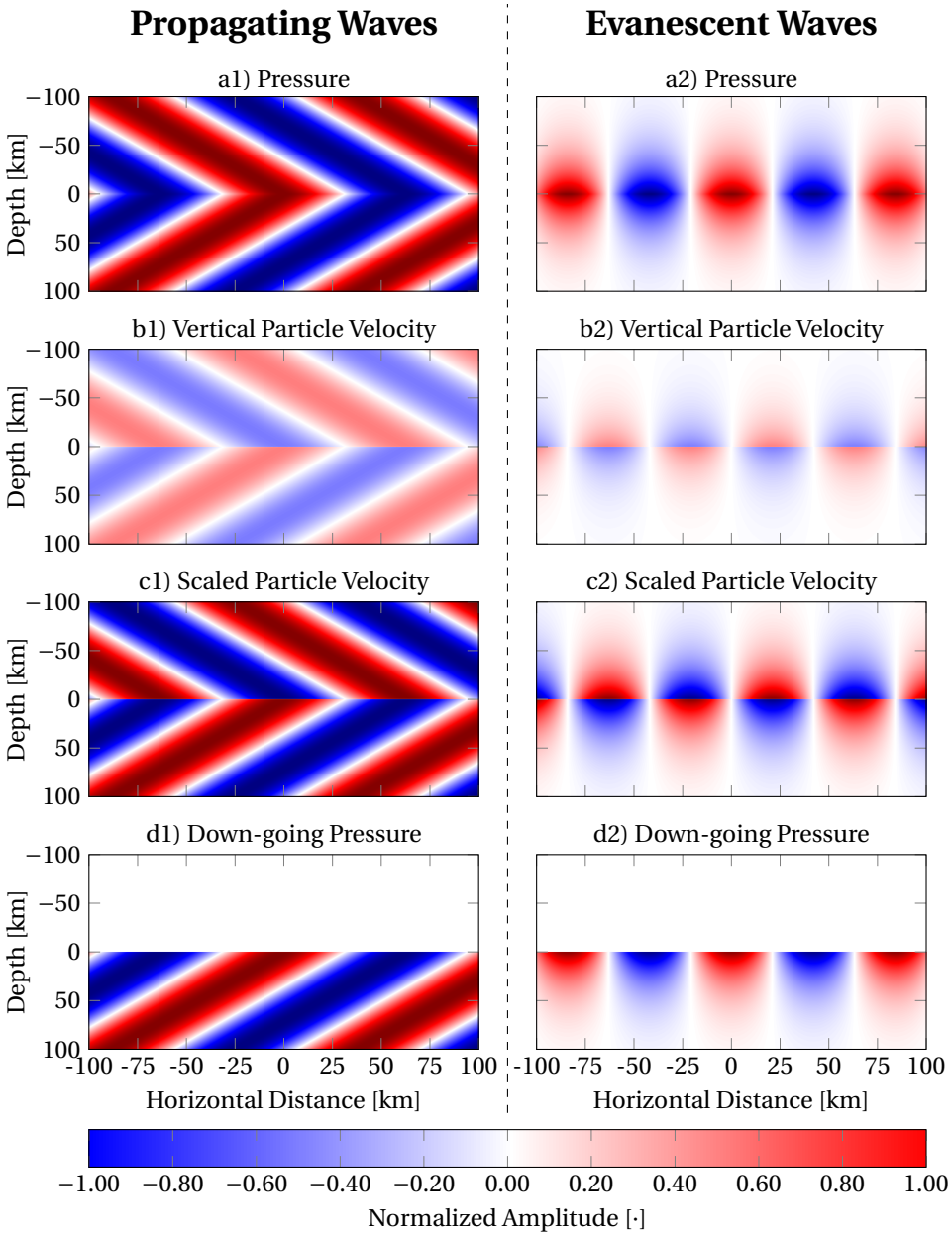

Figure 4.2: Propagating (left column) and evanescent (right column) 2D pressure wavefields (a) and their decomposed wavefields. a) shows the pressure wavefields and (b) shows the associated vertical component of the particle velocity. c) shows the vertical particle velocity scaled to the pressure as used in directional decomposition. d) shows the down-going pressure wavefield constructed from adding (a) to (c) and dividing by two. The wavefields are constructed from the posed pressure solutions in Equations 4.32 and 4.22 using $\omega_0 = 0.1$ s^{-1}, $t = 0$ s, $c = 1.5$ km s^{-1} and $\rho = 1$ g cm^{-3}. For the propagating waves $s_x = 0.5$ s km^{-1} and $s_y = 0$ s km^{-1}, while for the evanescent waves $s_x = 0.75$ s km^{-1} and $s_y = 0$ s km^{-1}. s_z and σ_z are based on c and s_x.

5

SNAPSHOT WAVEFIELD DECOMPOSITION FOR REVERSE TIME MIGRATION

Reverse Time Migration (RTM) is a two-way imaging algorithm that can handle all propagation directions, including the imaging of overturned structures and imaging from below based on multiple reflections. However, the created RTM images are not true reflection images, but rather a combination of reflection and transmission images. This manifests itself in low-wavenumber events in the image that obfuscate images of reflectors. As such, these transmission images are generally considered as artefacts. By directionally decomposing the wavefields during imaging it is possible to decompose the RTM image into its constituent reflection and transmission images, of which the reflection images generally constitute the desired image. Various techniques exist to decompose wavefields, and recent efforts have focused on directionally decomposing snapshots of a wavefield. In Chapter 2 we proposed a novel acoustic snapshot decomposition scheme to directionally decompose snapshots based on the pressure and its time derivative. We will now apply it to decomposing wavefields in the context of reverse time migration. The advantage of using this scheme in the context of RTM is that the method can account for horizontally travelling waves when up-down decomposing and it works, as the name implies, on snapshots, the native wavefield storage format of many time-stepping RTM schemes. We will illustrate and compare the suggested method to the current state of the art on a single-interface model, a complicated model and demonstrate it on real data.

5.1. INTRODUCTION

Reverse Time Migration (RTM) is a wave-equation based imaging scheme, that is commonly implemented using two-way propagators, and hence is capable of dealing with multi-path arrivals, the phase changes associated with caustics, and does not suffer from the dip-limitations of one way–extrapolation migration schemes (Hemon, 1978; Baysal et al., 1983; McMechan, 1983; Whitmore, 1983). It works by zero-lag cross-correlating two approximations of the subsurface wavefield during recording, which is the most basic RTM imaging condition. These wavefields are constructed by forward-in-time modelling the real-world source signature and backwards in time injecting and modelling the recorded wavefield in an approximate model of the medium of interest. For large problems with three spatial dimensions and one temporal, referred to hereafter as 3D, this is becoming increasingly feasible on modern compute architectures. As such, finite-difference RTM is a current industry standard for high fidelity images and iterative construction of approximate models of the medium of interest.

The employed zero-lag imaging condition between the forward-in-time modelled source wavefield and the back-propagated receiver wavefield, aside from constructing the subsurface image, also gives rise to what some consider artefacts, see for example Díaz and Sava (2015). As an example, strong early-time source and receiver wavefields traveling along the same ray path, causing their amplitudes during cross-correlation to constructively add up, lead to low wavenumber transmission images, or artefacts in terms of reflection imaging, in the final RTM images. It has been shown, by Fei et al. (2010) and Díaz and Sava (2015) for example, that a large part of these artefacts can be removed by directionally decomposing wavefields before imaging.

Many methods have been developed to decompose wavefields into up- and downgoing wavefields in the context of imaging, as the vertical direction is the dominant direction for variation in subsurface medium parameters for the Earth. Amundsen and Reitan (1995) among others developed a technique to decompose wavefields normal to the sea floor, i.e. the vertical direction, for homogeneous media. This wavefield-decomposition technique, however, is prohibitively expensive in the context of RTM as it cannot work on snapshots of wavefields, see Section 3.5. As such, faster and less resource-intensive schemes were developed. Yoon and Marfurt (2006) introduced the Poynting vector to acoustic imaging as an alternative, cheap and fast local approximation of the decomposition based on the directional energy flux of the wavefield, see Section 3.2. This was followed by Liu et al. (2011) who used plane-wave decomposition (Suprajitno and Greenhalgh, 1985), which is a more resource-intensive, but also a more accurate approximation, see Section 3.3. In the same work Liu et al. (2011) go on to demonstrate that this decomposition can be directly integrated into the imaging condition, making it once again local in time, by zero-lag cross-correlating spatial analytic wavefields. These are found by muting the negative wavenumbers in the desired decomposition direction for imaging. Using wavefields that are analytic along the vertical axis, instead of spatial and temporal Fourier transforms, greatly improves the speed and reduces the memory requirements when compared to conventional plane-wave–decomposition RTM, as only one-dimensional spatial Fourier transforms are needed.

This comes at a cost though, as the wavefields during RTM are no longer truly decomposed, losing some of the flexibility that decomposition offers inside the RTM imaging

condition. Therefore an alternative was sought, leading Shen and Albertin (2015) to decompose wavefields using the analytic-in-time form of wavefields. Analytic wavefields are constructed by forward modelling analytic representations of the source signature. To up-down decompose the real part of an analytic wavefield one simply takes the vertical Hilbert transform of the imaginary part of the data and adds or subtracts it from the real part to decompose the wavefield. However, this comes additional cost, since either the imaginary component of the wavefield must be modelled separately or complex modelling operators are needed to construct the required analytic wavefield.

We propose to use snapshot directional wavefield decomposition, see Chapter 2, to directionally decompose wavefields before imaging as the method can be made to work on wavefield snapshots and their time derivatives. Although snapshot wavefield decomposition only strictly allows for the decomposition of wavefields in homogeneous media, it also performing very well for heterogeneous media.

5.2. REVERSE TIME MIGRATION

Reverse Time Migration (RTM), originally proposed by Hemon (1978), Baysal et al. (1983), McMechan (1983), and Whitmore (1983), is a prestack depth migration scheme that works by zero-lag cross-correlating reconstructions of wavefields inside a medium of interest, like many other acoustic migration schemes, see Claerbout (1985). What differentiates RTM from other methods is the use of two-way scattering propagation operators when constructing these wavefields.

In acoustic RTM, incident and out-going pressure wavefields travelling in opposite directions inside the medium of interest are zero-lag cross-correlated to form a reflection image of the medium of interest. For transmission images, which are often considered to be artefacts when overprinting the desired reflection image (Fei et al., 2010), the incident and out-going wavefields travel in the same direction. To approximately reconstruct these wavefields inside the medium of interest, an approximate model of the medium is required, which is at least kinematically correct.

The governing imaging condition for acoustic RTM is the following zero-lag cross-correlation of the forward propagated[1] wavefield $f(\boldsymbol{x},t)$, also known as the source wavefield, with the backward propagated wavefield $b(\boldsymbol{x},t)$, also known as the receiver wavefield, see Liu et al. (2011) for example:

$$i(\boldsymbol{x}) = \int_{-\infty}^{\infty} f(\boldsymbol{x},t)\,b(\boldsymbol{x},t)\,\mathrm{d}t \tag{5.1}$$

where $i(\boldsymbol{x})$ is the migration image and the wavefield $f(\boldsymbol{x},t)$ and $b(\boldsymbol{x},t)$ are assumed to be real. For an overview of possible RTM imaging conditions we refer to Jones (2014).

The forward propagated wavefield $f(\boldsymbol{x},t)$ is an estimate of the wavefield inside the medium of interest during the time of recording based on the known source field used to excite the wavefield inside the medium of interest. The wavefield is predicted by forward modelling the source field in time using either non-scattering modelling operators,

[1] Note that in this chapter propagation is assumed to also include evanescence as two-way modelling operators are used throughout.

when honouring the single-scattering approximation, or modelling operators that include scattering, from now on referred to as scattering modelling operators. We will be using scattering modelling operators.

The backward propagated wavefield $b(\boldsymbol{x}, t)$ is another estimate of the wavefield inside the medium of interest during the time of recording, but now based on the recorded data. The wavefield is predicted via the back-injection of the recorded data at the receiver locations, causing the wavefield to propagate backwards in time.

Fei et al. (2010) realized that directionally decomposing, or de-blending, the RTM imaging condition, Equation 5.1, allows for the retrieval of the reflection and transmission images in the form of four separate imaging conditions. To do this we need to directionally decompose wavefields, see Chapter 2.

If we now consider that the decomposition of a wavefield p into p^+ and p^-, which travel in opposite directions, occurred along the normal direction to some interface, then p^+ above the interface may correspond to the incident wavefield at the interface, while p^+ below the interface would correspond to the transmitted wavefield. p^- above the interface would then be the reflected wavefield. If we now apply the same concept to the forward and backward modelled wavefields from Equation 5.1 and treat $f(\boldsymbol{x}, t)$ always as the incident wavefield and $b(\boldsymbol{x}, t)$ as the transmitted or reflected wavefield, then we can image the inherent four separate terms in Equation 5.1. Fei et al. (2010) refer to this as de-blending RTM. To better understand this we directionally decompose $f(\boldsymbol{x}, t)$ and $b(\boldsymbol{x}, t)$ in Equation 5.1 to find:

$$i(\boldsymbol{x}) = \tau^+(\boldsymbol{x}) + r^+(\boldsymbol{x}) + r^-(\boldsymbol{x}) + \tau^-(\boldsymbol{x}), \tag{5.2}$$

where the first and last term correspond to the two possible transmission images, τ, and the middle terms correspond to the two possible reflection images r:

$$\tau^+(\boldsymbol{x}) = \int_{-\infty}^{\infty} f^+(\boldsymbol{x}, t) b^+(\boldsymbol{x}, t) \mathrm{d}t, \tag{5.3}$$

$$r^+(\boldsymbol{x}) = \int_{-\infty}^{\infty} f^+(\boldsymbol{x}, t) b^-(\boldsymbol{x}, t) \mathrm{d}t, \tag{5.4}$$

$$r^-(\boldsymbol{x}) = \int_{-\infty}^{\infty} f^-(\boldsymbol{x}, t) b^+(\boldsymbol{x}, t) \mathrm{d}t, \tag{5.5}$$

$$\tau^-(\boldsymbol{x}) = \int_{-\infty}^{\infty} f^-(\boldsymbol{x}, t) b^-(\boldsymbol{x}, t) \mathrm{d}t, \tag{5.6}$$

where the superscript + and − for the images denote the direction in which the incident wavefield $f(\boldsymbol{x}, t)$ travels.

It should be noted here that the efficacy of each of these imaging terms strongly depends on the acquisition geometry used to record the data. For the dominant terms in the reflection images, $r^+(\boldsymbol{x})$ and $r^-(\boldsymbol{x})$ to be related to reflectors and not artefacts, the reflected wavefield needs to be well reconstructed. A perfect reconstruction of these wavefields in an acoustic setting is generally not possible as the underlying acoustic Kirchoff-Helmholtz integrals (Wapenaar and Berkhout, 1989) require a recording surrounding the

medium of interest that records the pressure and normal component of the particle velocity. Furthermore perfect knowledge of the medium of interest and all sources inside is required. In most seismic exploration settings at best approximately kinematically correct velocity models in conjunction with open multicomponent recording surfaces above the medium of interest are available. Back injecting the recorded wavefield under these conditions only approximately reconstructs the traveltime and wavelet shape of primary reflection events at their reflectors. Amplitudes of the reconstructed wavefield at reflectors are wrong due to the inability to reconstruct the transmitted wavefield at the reflectors due to the one-sided acquisition, the incorrect velocity model and an often poor understanding of the density model. This entails that the reflection images are approximately correct with respect to the locations of pronounced reflectors, but the amplitudes of the reflection image are incorrect. This problem is exasperated for the transmission images as the transmitted wavefields generally cannot even be approximately reconstructed in RTM due to the recording surface only being above the medium of interest. Hence, the transmission images tend to be dominated by what are generally considered to be artefacts (Yoon and Marfurt, 2006; Liu et al., 2011). This is nicely demonstrated in Díaz and Sava (2015).

Historically conventional seismic exploration only used sources and receivers above the medium of interest, hence Fei et al. (2010) suggested to use Equation 5.4 as a reflection imaging condition, in the context that plus fields travel in the downwards direction, as the reflection imaging condition. Others, like Yoon and Marfurt (2006), Liu et al. (2011), and Díaz and Sava (2015) for example, have suggested to define the reflection image for real wavefields based on the sum of the two reflection images, Equations 5.4 and 5.5:

$$r(\boldsymbol{x}) = \int_{-\infty}^{\infty} \left[f^+(\boldsymbol{x},t) b^-(\boldsymbol{x},t) + f^-(\boldsymbol{x},t) b^+(\boldsymbol{x},t) \right] \mathrm{d}t, \tag{5.7}$$

This imaging condition has the advantage of being free of the transmission related images, while still accounting for reflections from both sides of an interface. We will now tackle the problem of how to find the directionally decomposed wavefields necessary to formulate the reflection image $r(\boldsymbol{x})$ and the transmission image $\tau(\boldsymbol{x}) = \tau^+(\boldsymbol{x}) + \tau^-(\boldsymbol{x})$.

Historically the directionally decomposed f^+, f^-, b^+ and b^- fields were computed using plane-wave decomposition, which cannot decompose snapshots of a wavefield. This led Liu et al. (2011) to develop an imaging condition that does not require temporal Fourier transforms, allowing it to work on snapshots of a wavefield. This was achieved by rewriting the reflection imaging condition, Equation 5.7, in conjunction with the concept of plane-wave decomposition, see Section 3.3, in terms of spatially analytic signals:

$$i(\boldsymbol{x}) = 2\Re \left\{ \int_{-\infty}^{\infty} f_+^*(\boldsymbol{x},t) b_+(\boldsymbol{x},t) \mathrm{d}t \right\}, \tag{5.8}$$

where $\Re$ denotes the real part and the superscript $*$ denotes the complex conjugation for the cross-correlation of complex signals. The analytic signals f_+ and b_+, which follow the notation of Liu et al. (2011), should not be confused with directionally decomposed wavefields. They are spatially analytic signals and are defined in the wavenumber domain

as follows:

$$\tilde{f}_+ = \begin{cases} \tilde{f} & \text{if } k_z > 0, \\ \frac{\tilde{f}}{2} & \text{if } k_z = 0, \\ 0 & \text{otherwise,} \end{cases} \tag{5.9a}$$

$$\tilde{b}_+ = \begin{cases} \tilde{b} & \text{if } k_z > 0, \\ \frac{\tilde{b}}{2} & \text{if } k_z = 0, \\ 0 & \text{otherwise.} \end{cases} \tag{5.9b}$$

The problem with the above is that we are no longer actually directionally decomposing the wavefield. To rectify this we can use wavefields that are also analytic in time, see Section 3.4, at the cost of twice the modelling work, or snapshot directional wavefield decomposition, which requires more spatial Fourier transforms but is also more flexible.

5.3. MONOCOMPONENT SNAPSHOT WAVEFIELD DECOMPOSITION FOR RTM

In time-stepping RTM we commonly only know one component of the wavefield and its time derivative, such that we can step the wavefield forward in time. Many acoustic RTM schemes are therefore implemented using time-stepping finite-difference or finite-element schemes in which only the pressure, as a scalar quantity, is stepped forward from one time step to the next. As such, the particle velocity, which is necessary to directionally decompose the wavefield using the equations from Chapter 2, is not known.

If we relax the condition of the decomposition having to work on a multicomponent wavefield at a given instance in time to working on a wavefield and its time derivative, then the decomposition can be formulated in terms of a single component of the wavefield. To do this for the pressure we solve Equation 2.32 for the generalized particle velocity $\tilde{v}_z$:

$$\tilde{v}_z = \frac{1}{\rho c^2} \frac{-i k_z}{\boldsymbol{k} \cdot \boldsymbol{k}} \partial_t \tilde{p}. \tag{5.10}$$

The denominator in this equation is only non-zero at the origin of the wavenumber domain, corresponding to the space-invariant component of the time derivative of the pressure. The generalized particle velocity must be zero at the origin in the wavenumber domain due to its definition, hence it is set to zero at the origin in the wavenumber domain for Equation 5.10.

Inserting Equation 5.10 into 2.34 and pulling the term in front of the time derivative of the pressure into the matrix we can write:

$$\begin{pmatrix} \tilde{p}_z^+ \\ \tilde{p}_z^- \end{pmatrix} = \frac{1}{2} \begin{pmatrix} 1 & (ci\,\mathrm{sgn}(\kappa_z)|\boldsymbol{k}|)^{-1} \\ 1 & -(ci\,\mathrm{sgn}(\kappa_z)|\boldsymbol{k}|)^{-1} \end{pmatrix} \begin{pmatrix} 1 \\ \partial_t \end{pmatrix} \tilde{p}, \tag{5.11}$$

where the fraction is set to zero for $|\boldsymbol{k}| = 0$. This is acceptable because the time derivative of the pressure at the origin in the wavenumber domain must be zero for the acoustic wave equation to hold. The effect of doing this is that the static part of the pressure wavefield is equally split up between the decomposed fields.

Appendix C contains an alternative derivation of Equation 5.11 straight from the acoustic wave equation as well as an alternative formulation of the decomposition in terms of the time integral of the pressure for a zero constant of integration, also known

as the temporal primitive of the pressure:

$$\begin{pmatrix} \tilde{p}_z^+ \\ \tilde{p}_z^- \end{pmatrix} = \frac{1}{2}\begin{pmatrix} 1 & ci\,\mathrm{sgn}(\kappa_z)|\boldsymbol{k}| \\ 1 & -ci\,\mathrm{sgn}(\kappa_z)|\boldsymbol{k}| \end{pmatrix}\begin{pmatrix} \tilde{p} \\ \int \tilde{p}\,\mathrm{d}t \end{pmatrix}. \tag{5.12}$$

The difference between Equations 5.11 and 5.12 is that in Equation 5.11 the spatial and temporal operations are inverted with respect to each other.

The generalized particle-velocity-normalized directional decomposition is exactly the same as for the pressure. The only difference is that the pressure has been replaced with the generalized particle velocity in the decomposition direction. This can be found by solving Equation 2.33 for the pressure and using the result to replace the pressure in Equation 2.36 with the time derivative of the generalized particle velocity, followed by a reorganization of the right-hand-side matrix-vector term.

Equation 5.11 has three advantages over the previously discussed snapshot wavefield decompositon schemes. It does not depend on the mass density, which is often neglected in RTM as it is more difficult to accurately estimate than the velocity. Furthermore Equation 5.11 is ideal for decomposing wavefields as they are modelled using time-stepping, as from one time step to the next both the wavefield and its time derivative are known. Additionaly the decomposition direction is not fixed and can vary spatially allowing for the decomposition and imaging normal to expected variations in medium parameters. Therefore snapshot directional wavefield decomposition is the ideal scheme for wavefield decomposition in the context of RTM. This makes it ideal for acoustic imaging schemes like RTM when implemented using time stepping, and it is this equation that is used to generate the results for the remainder of this chapter, including decomposition normal to variations in media.

5.4. NUMERICAL & REAL DATA EXAMPLES

In the following we will illustrate snapshot wavefield decomposition in comparison to conventional RTM without wavefield decomposition, Equation 5.1, using Poynting decomposition (Chen and He, 2014), using plane-wave decomposition according to Suprajitno and Greenhalgh (1985), and using a modified imaging condition based analytic wavefields (Liu et al., 2011). From here on we will refer to RTM without wavefield decomposition as conventional RTM, the other RTM types we will refer to according to their decomposition type or imaging condition, i.e. Poynting, plane-wave, snapshot, and analytic RTM.

We will not compare snapshot RTM to surface-normal decomposition, as it usually operates in the wavenumber-frequency domain, which is not ideal for decomposing snapshots of a wavefield for imaging with the conventional finite difference RTM. We will also not discuss analytic source-signature-based directional-wavefield-decomposition schemes, which are based on additionally injecting the temporal Hilbert transforms of the source signatures and recorded data, as this usually requires additional wavefield modelling steps. The interested reader is referred to Shen and Albertin (2015), or for a recent approach that only requires modelling one wavefield see Revelo and Pestana (2019).

To construct the following RTM images the recorded receiver wavefields were mod-

elled using finite-difference techniques[2] using the exact model. The boundary conditions were 50-element-wide perfectly matched layers (Chew and Liu, 1996) on all sides to avoid boundary-related multiples. The direct wave in the receiver data was removed by modelling it separately in a homogeneous medium and subtracting it from the receiver data modelled using the exact model of the medium to be imaged. This way ideal RTM data, devoid of surface-related multiples and the direct wave, were constructed.

5.4.1. TWO LAYER MODEL

We return to Figure 3.1 and migrate this model using the reflection imaging condition, Equation 5.7, while decomposing with the previously mentioned techniques. The migrated RTM results are due to the same source signature as for Figure 3.1 but placed at increments of 1 m between -200 m and 200 m, while back-injecting only the wavefield recorded at the top of the model, after removing the direct wave. In the conventional migration result, see Figure 5.1c, when compared to the others we see dominant low-wavenumber artefacts, which correspond to the transmitted image. These are introduced, according to Díaz and Sava (2015), by the cross-correlation of the back-scattered fields. Note that the model was not smoothed to avoid back-scatter. The result achieved using Poynting decomposition, see Figure 5.1a, is a clear improvement over Figure 5.1c, however, there are still errors in the interface around the horizontal origin (middle of figure), compare the blue amplitudes above the interfaces in Figures 5.1a and 5.1b. These are absent in the nearly identical Figures 5.1b and 5.1d which were decomposed using plane-wave and snapshot decomposition. Evidently snapshot decomposition is comparable in accuracy to plane-wave decomposition. As expected, analytic imaging (Liu et al., 2011), Figure 5.1e, is equivalent to plane-wave imaging Figure 5.1b.

5.4.2. THREE-LAYER MODEL

To better illustrate the flexibility of actual wavefield decomposition when imaging in RTM over using the analytic imaging condition by Liu et al. (2011), we consider a slightly more complex three-layer model. The same setup as for Figure 3.1 is used, but now with a velocity increase from 1 km/s to 1.5 km/s at a depth of 175 m and another increase to 2 km/s at 350 m. We now wish to image the individual transmission and reflection responses, Equations 5.3–5.6. This is not possible with analytic RTM, demonstrating the superior flexibility of snapshot wavefield decomposition as an actual decomposition.

Figure 5.2 shows the four separate images. The diagonal images, Figures 5.2a and 5.2d, show the transmitted imaging results for the zero-lag cross-correlation of down- with down-going wavefields and up- with up-going wavefields respectively. The off-diagonal images, Figures 5.2b and 5.2c, show the corresponding reflection images. Figure 5.2b is formed by the cross-correlation of a down-going incident wavefield (full red ray) with an up going–out going wavefield (full blue ray), and ideally vice versa for Figure 5.2c. Note that the amplitudes in Figure 5.2c have been exaggerated by a factor of 10. Where the red rays denote the estimated wavefield in the medium of interest based on the forward propagated wavefield $f(\boldsymbol{x}, t)$, while the blue rays denote the predicted wavefield based on the backward propagated wavefield $b(\boldsymbol{x}, t)$. For Figure 5.2b this would only image

[2] A variant of the wavefield modelling code by Thorbecke and Draganov (2011) was used.

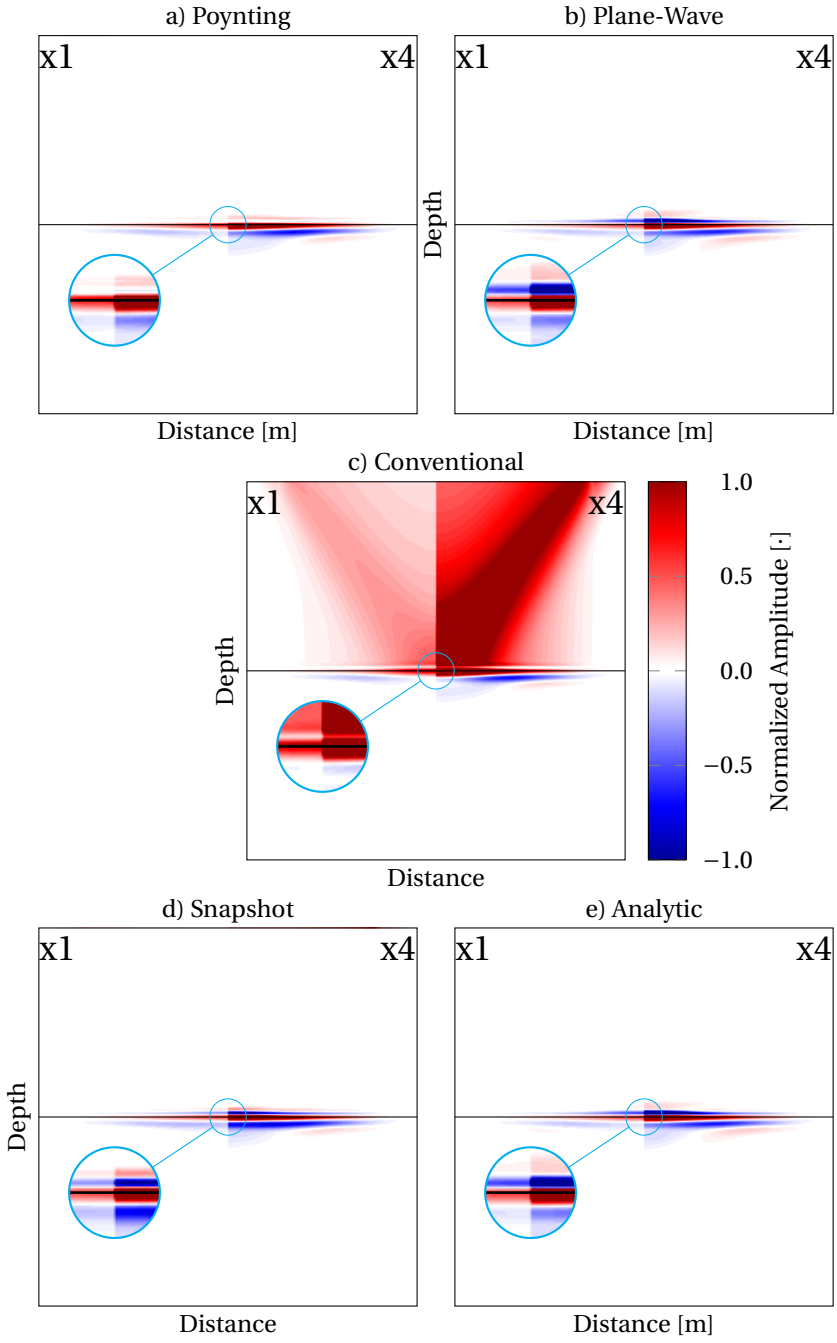

Figure 5.1: Pressure RTM results without decomposition, Equation 5.1, (c) for the same model as in Figure 3.1 compared to the reflection-only imaging condition, Equation 5.7, using various decomposition schemes (a, b, d and e). All amplitudes are normalized with respect to the maximum amplitude in (c) and the right-hand-side amplitudes of each figure are exaggerated by a factor of 4.

above the interface, but we see a contribution below the interface. This stems from the dashed contribution where the backward propagated wavefield below the interface is cross-correlated with the forward propagated wavefield. In this case $b(\boldsymbol{x}, t)$ behaves somewhat like an incident wavefield from below at the interface, while $f(\boldsymbol{x}, t)$ is the out-going wavefield. Both these terms together constitute the reflection image of the reflector. It should be noted that the blue dashed ray in this case is not physical as it is an event arising from the fact that the reconstructed wavefield $b(\boldsymbol{x}, t)$ in this case is based only on recordings at the top of the model. If the wavefield had been recorded everywhere around the model, then after correct back-injection and back-propagation, this transmitted response (dashed blue line) would have been cancelled by the back propagated wavefield from below.

In Figure 5.2c the reflectors appear to be only imaged from above. This is because in this case the dominant term is denoted by the dashed ray paths, where we are cross-correlating the incident wavefield from above, reconstructed using scattering operators from the recordings $b(\boldsymbol{x}, t)$, with the reflected wavefield, reconstructed from the source distribution using scattering operators. If non-scattering operators had been used, this contribution would be zero, hence the dashed ray paths. We, however, also have energy below the reflectors, see the upper spy glass where the amplitudes are exaggerated hundred fold, which is caused by the zero-lag cross-correlation of multiply scattered waves, which corresponds to an incident wavefield from below and an out-going reflected wavefield. This configuration is denoted in the full ray figure. It is this contribution that allows RTM to image interfaces from below. We do not see this feature in the lower spyglass because there is no reflector below that could multiply reflect the necessary waves to construct this image as absorbing boundary conditions were used. Please also note that when using single-sided illumination from above and non-scattering propagation operators, Figure 5.2c cannot be reconstructed.

If we sum Figures 5.2a and 5.2d we would find the transmission image τ, whereas if we sum Figures 5.2b and 5.2c we find the reflection image r. Poynting, plane-wave and snapshot decomposition are able to construct these images, analytic RTM can only construct the sum of Figures 5.2a–d. This demonstrates the flexibility of actual wavefield decomposition in RTM over analytic RTM, which, however, is numerically still the fastest method. Note that in this case snapshot wavefield decomposition was used to construct the image, even though any other directional wavefield decomposition could have been used.

5.4.3. ANNERVEEN MODEL

Let us now consider a more complex model. The Annerveen model, first presented by Almagro Vidal et al. (2014), is based on a vertical cross section near Annerveen, in The Netherlands, and is dominated by salt-domes under which hydrocarbons are trapped. The acoustic velocity model is shown in Figure 5.3a while the density model is shown in Figure 5.3b. To properly image this model, far-offset data is needed to resolve features in near-offset shadow zones, like the hydrocarbon-bearing antiform under the central salt dome at a horizontal distance of 11 km and a depth of 3 km.

To model the recorded receiver wavefield 321 volume-injection sources were placed every 50 m between 2 km and 18 km at the surface in the 5x5 m discretized model. The

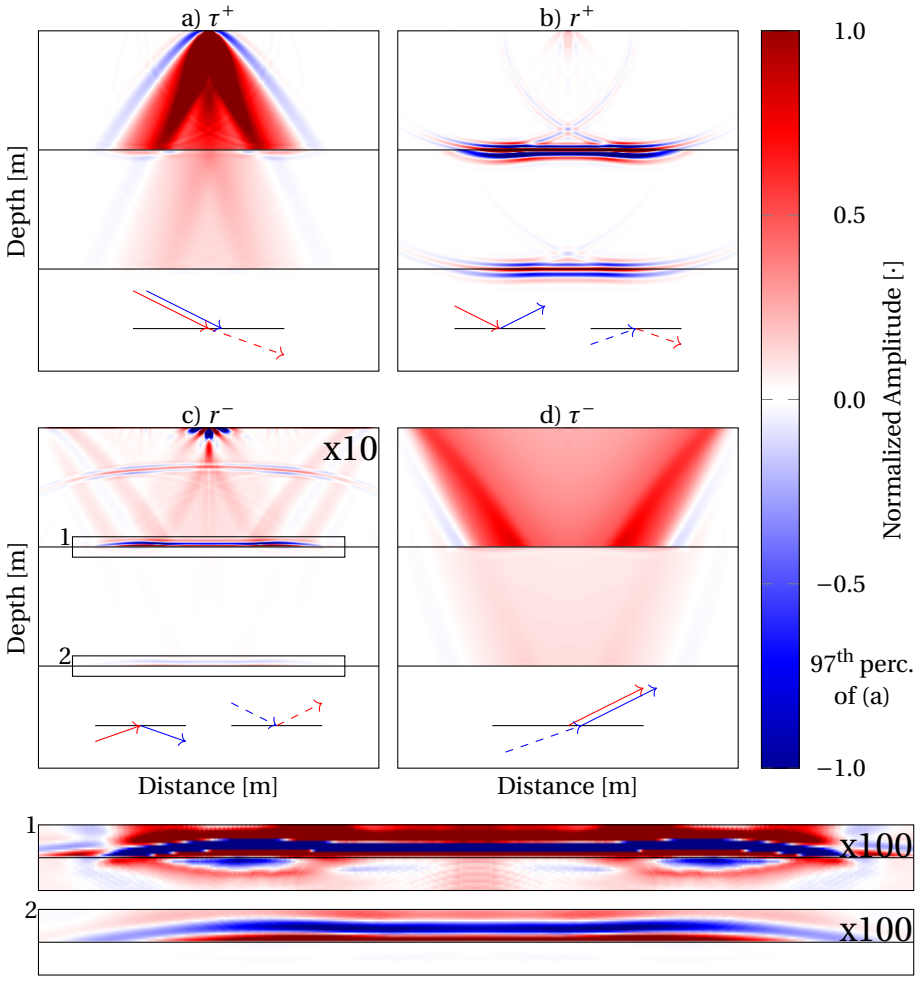

Figure 5.2: Decomposed migration images of a three layer model found by zero-lag cross-correlating wavefields after up-down directional wavefield decomposition for a single volume injection source. All amplitudes have been normalized with respect to the 97$^{\text{th}}$ percentile of (a). The amplitudes of (c) have been further exaggerated by a factor of ten, while the amplitudes in the spy-glasses have been exaggerated by a factor of one hundred.

sources injected 22 Hz peak-frequency Ricker wavelets, linearly high-cut tapered in the frequency domain from 70–75 Hz.

Figure 5.4 shows RTM results for one source at the surface at a lateral distance of two kilometres using the exact subsurface model and source signature. This is not a generally realizable subsurface model for real data but allows us to compare the methods without effects due to an approximate subsurface model. Figure 5.4a shows the conventional RTM image without decomposition with the expected strong low-wavenumber artefacts due to the transmitted component of the image, which also highlights the dendritic ray

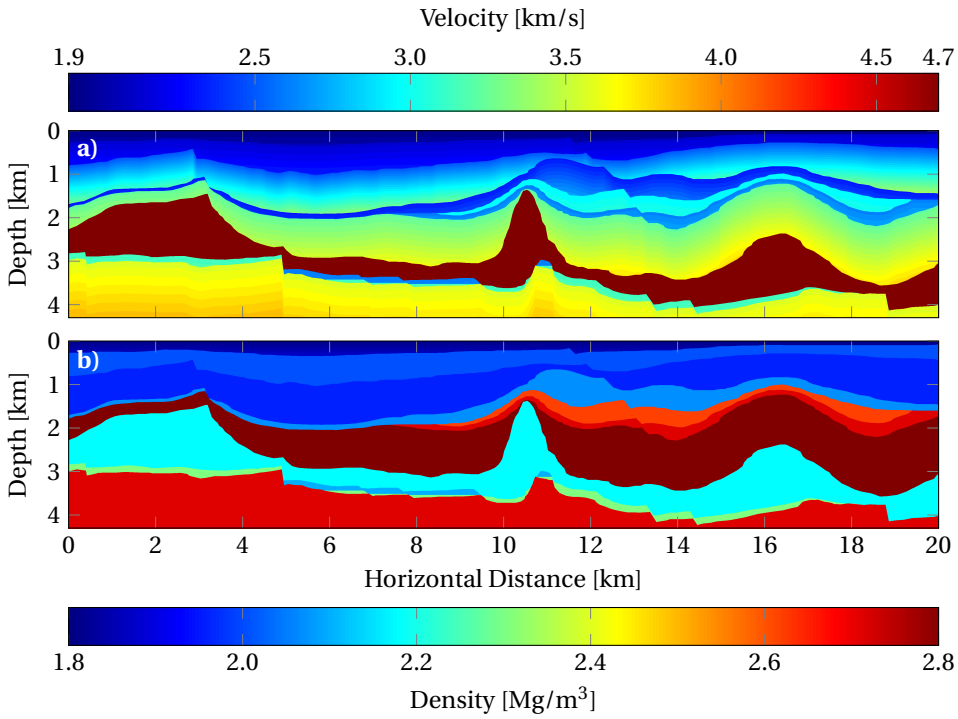

Figure 5.3: Annerveen acoustic velocity (a) and density (b) model.

paths. Interestingly the low-wavenumber artefacts are much stronger in the wave guide at a depth of 2 km between 4 and 12 km horizontal distance. A lot of energy is trapped in this wave guide.

Using Poynting decomposition, Figure 5.4b, greatly improves the result. In the lower-right black spyglass we can see that we have now managed to remove the transmitted image, or red backscattered noise, present in the same spyglass in Figure 5.4a. However, the method suffers from artefacts where wavefields interfere. This is especially evident in the upper left corner, which shows extremely high-wavenumber artefacts due to the interference of waves and associated incorrect wavefield decomposition. These artefacts occur because the employed subsurface model invalidates the assumption that the forward and backward propagation of the source and receiver wavefields is reflection-free. Only when the source and receiver wavefields are nearly free of scattering is it guaranteed that the direct wavefield is the strongest wavefield, ensuring that Poynting decomposition works correctly. These artefacts are also responsible for the serrated look of the upper reflector in the lower-left spyglass. This is especially visible in the magnified portion.

Using analytic or plane-wave RTM smooths out the Poynting decomposition results as can be seen in Figure 5.4c. The results appear to contain more low-frequency noise when compared to the Poynting decomposed results. This is because Poynting decom-

position left out a large portion of the wavefield during imaging because it was not able to decompose properly. Hence the analytic RTM results are actually better. Note though that plane-wave decomposition does not properly decompose wavefields in an inhomogeneous medium, making the decomposed results imperfect in this inhomogeneous setting. This RTM image is also not free of artefacts. At the bottom between 2 and 5 km there are low-wavenumber edge-related artefacts, as can be seen in the bottom-most spyglass. Even though the source and receiver wavefields were tapered before their analytic fields were computed we still find edge-related artefacts where there were strong horizontally scattered waves. These are also responsible for the unexpected artefacts on the right side of the lower right spyglass when compared to the other methods.

Using snapshot decomposition, Figure 5.4d, improves on these results. The edge-related artefacts are strongly diminished for two reasons: 1) because the horizontal Fourier transform necessary to scale the time derivative of the pressure to the pressure in Equation 5.11 is better at separating horizontally travelling waves than a single vertical analytic transform and 2) because the scaled time derivative of the pressure was high-cut tapered to zero from 100% to 120% of the Courant number of the employed finite-difference scheme. This is why there are also no artefacts on the right side of the spyglass when compared to Figure 5.4c. Using snapshot decomposition also better resolves the "sausage-like" effect, green boxes in Figures 5.4c and 5.4d, caused by the quasi point scatterer at the top of the blue velocity layer, above the left salt dome. This effect is also seen in Figure 5.4c, albeit not as pronounced. It should also be noted th that the wavefields used to produce this image were not tapered at the edges before decomposition, hence there are non-zero amplitudes along the surface when compared to Figure 5.4c.

The decomposition direction map used for the directional decomposition of wavefield snapshots in this example is based on smoothing the specific acoustic impedance model using a 100x100 m moving average filter, followed by a normalized direction vector estimation based on the gradient. The direction vector is then converted into an angle. Given the angle map a down sampled list of 101 decomposition angles was established. Based on these decomposition occurred. The results were then interpolated based on the original angle map from the downsampled angle decomposition results.

Stacking all the migrated shots, or images, along the surface between 2 and 18 km allows us to compare the final migrated sections in Figure 5.5. The low-wavenumber back-scatter artefacts are again present in the final conventional image, see Figure 5.5a. These artefacts, however, do significantly help to delineate the central salt dome, whose reflections are relatively weak due to a weak impedance contrast with the surrounding material. Please note that the amplitudes were divided by five for this migration result to better compare the result to the decomposed images.

The Poynting decomposition results, Figure 5.5b, are free from these artefacts, predominantly only near-source artefacts remain near the top of the model, which in this image were not tapered out. Most of the reflectors are now clearly visible, but the central salt dome is nearly invisible; this is due to the aforementioned weak reflections. The image also suffers from Poynting decomposition-induced artefacts, leading to a sometimes jittery behaviour along interfaces for the per-shot images, see spyglasses in Figure 5.4b. During stacking these artefacts often sufficiently stack out such that they can be

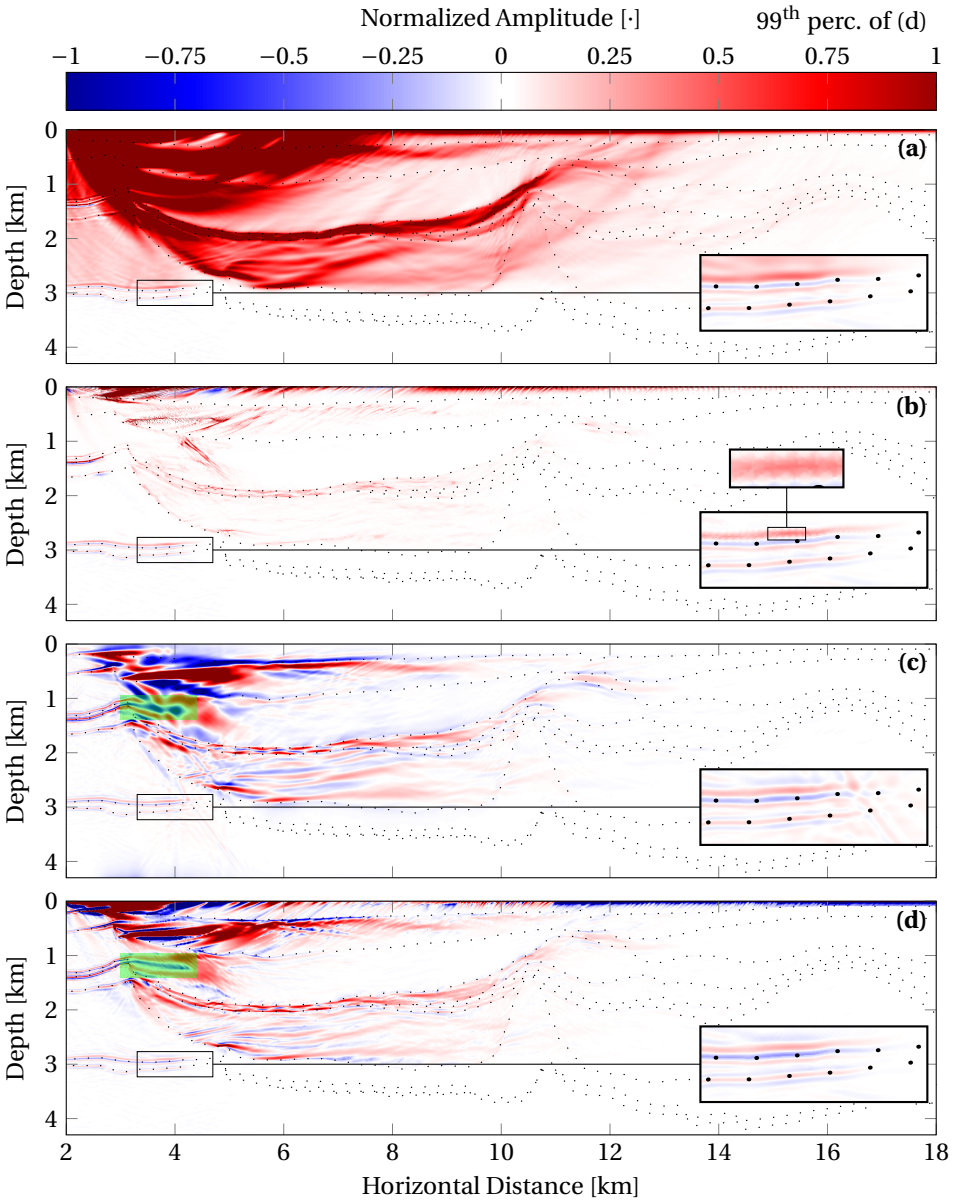

Figure 5.4: Comparison of Annerveen migration results for one shot at the surface at a distance of 2 km using conventional RTM (a), Poynting RTM (b), analytic RTM (c), and snapshot RTM (d). Amplitudes have been normalized to the 99th percentile of (d).

neglected for the purpose of structural interpretation.

Analytic RTM improves on the Poynting results, see Figure 5.5c. The reflector continuity is improved, clearly delineating the hydrocarbons trapped below the central salt dome. The Poynting decomposition results do appear to have a higher resolution along the top salt interface, this is believed to be an artefact of Poynting decomposition. It should be noted that this image is tapered at the top and bottom as the wavefields used to construct this image were tapered at the top and bottom. The taper was necessary in this case to avoid aliasing artefacts due to the circular nature of the employed discrete Fast Fourier Transform (FFT) (Frigo and Johnson, 2005). This leads to artefacts at the top and bottom of the image that manifest as a slightly blue tint.

The snapshot-decomposed results, Figure 5.5d, in which decomposition occurred normal to interfaces, delineate the central salt dome the best and reflectors appear sharper than in the other imaging results. The sharpness is, however, partially due to using the exact velocity model during decomposition which overprints onto the final migrated results. The improved imaging of the salt dome, however, is attributed to decomposition directions normal to its flanks. The snapshot-decomposed results also exhibit better positive amplitude continuity for the large red layers, which is expected as these layers have a positive velocity gradient and as such are reflective throughout. One would also expect that this image should have been tapered at the edges. This, however, was not necessary as it would have only improved results marginally. The suspected reason for this is that both the pressure and scaled time derivative of the pressure had the same or sufficiently similar aliasing. Hence it was found that tapering did not noticeably improve image quality in the non-tapered areas, while the non-tapered image was clearly better than the tapered image in the tapered areas.

As a whole the analytic RTM image is the smoothest image and as a consequence has the best reflector continuity. Whereas the snapshot-decomposed result has the best reflector imaging and structural detail, see the central salt dome, which makes it difficult to discern which is better. It should be noted that during the generation of these images the inverse crime was committed as the same method was used to model the input synthetic wavefields as was used to compute the RTM image.

5.4.4. ANNERVEEN MODEL: IMAGING WITH APPROXIMATE VELOCITY MODEL

As the previous set-up of migrating with the exact velocity and density models is rarely feasible in reality the velocity model was smoothed using a 500x500 m moving average filter, see Figure 5.6, and the density model was set to a homogeneous 1000 kg/m^3, as it is often much more difficult to construct approximate density models as opposed to velocity models. The data were migrated again using the smoothed approximate subsurface model, which resulted in the single shot migrated data in Figure 5.7.

The images are now slightly blurred and reflectors are positioned slightly too deep. The conventional image has lost its dendritic nature, but a large portion of the artefacts related to the transmission image are now gone. Further note that although the model has been significantly smoothed the image of the waveguide between 1 and 2 km remains. In the left parts of Figure 5.7, from 0 to 2 km horizontal distance, there are additional spurious curved events caused by the zero-lag cross-correlation of unrelated events. These

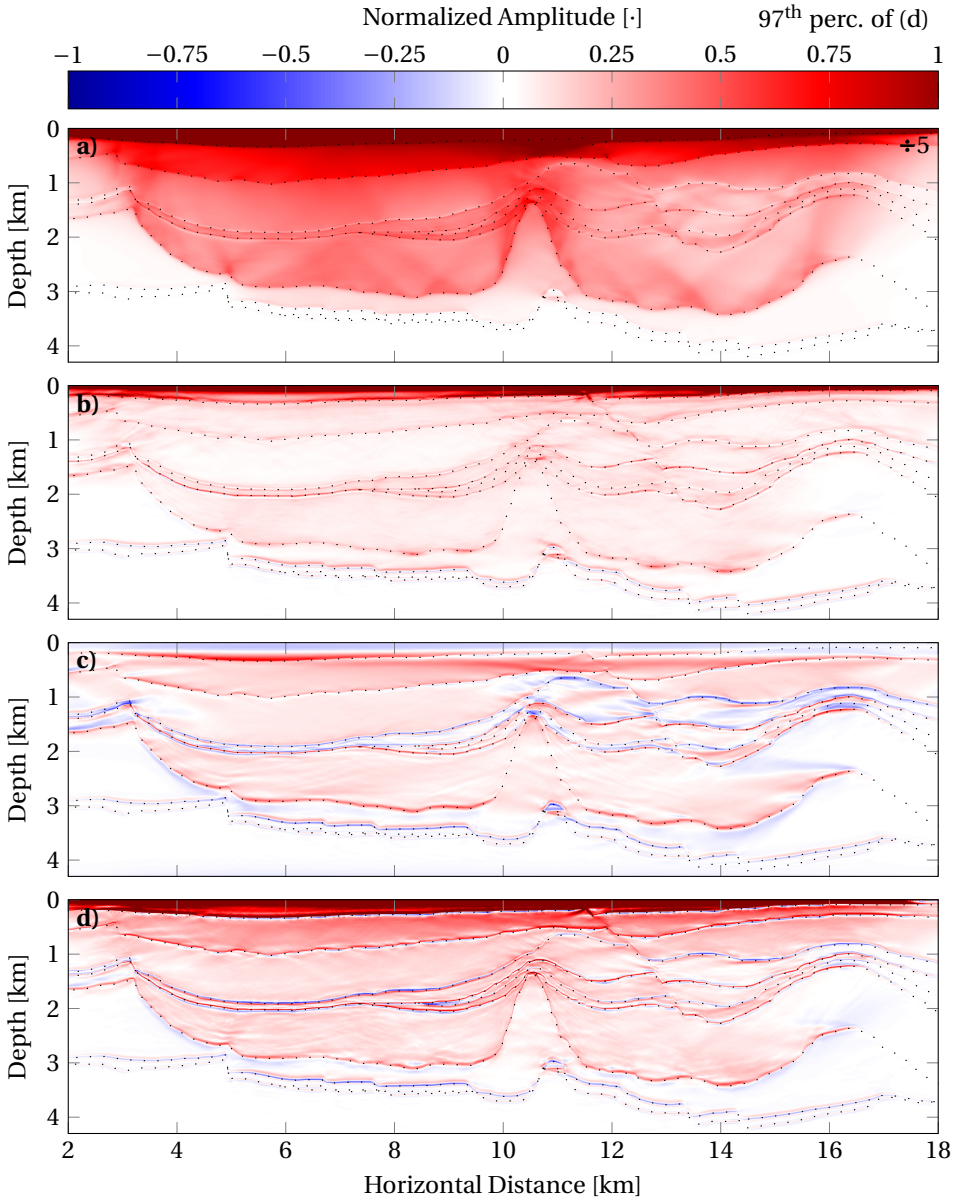

Figure 5.5: Comparison of stacked Annerveen Migration results using conventional RTM (a), Poynting RTM (b), analytic RTM (c), and snapshot RTM (d). Amplitudes have been normalized to the 97th percentile of (d).

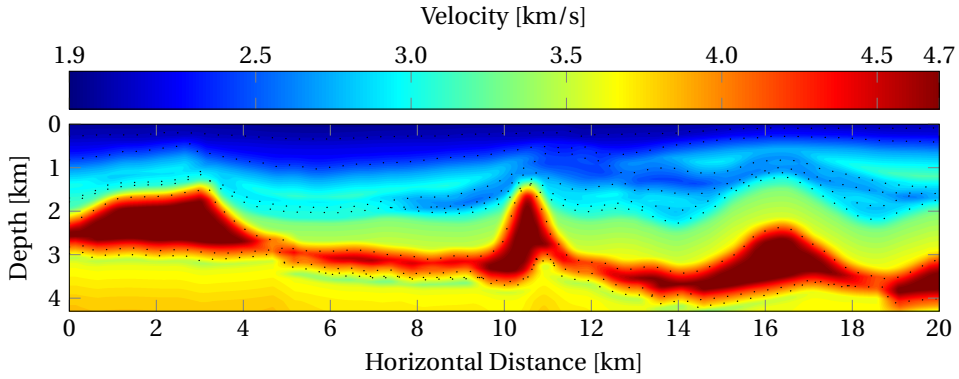

Figure 5.6: Annerveen acoustic velocity model smoothed using a 500x500 m moving average filter. The corresponding density model is 1 kg/m^3.

events will remain in the decomposed results but become weaker where they are nearly vertical. They are due to the incorrect velocity model aligning unrelated events to each other during imaging.

Again decomposing the wavefield removes most of the transmission-image artefacts as can be seen when comparing Figures 5.7b–d to 5.7a. Poynting RTM once more suffers from the extremely inexact nature of the decomposition in the presence of interference, which in this creates a hole in the image, see spyglass in Figure 5.7b. The analytic RTM results, on the other hand, have again edge effects, see the diagonal event in the spyglass in Figure 5.7c. This event is easily recognizable when comparing to the snapshot-decomposed result, see spyglass in Figure 5.7d. Nevertheless the three decompositions produce very comparable results.

Note that the decomposition direction map for snapshot directional wavefield decomposition is in this case only based on the smooth velocity model, see Figure 5.6, as the density model is constant. This also means that it points more dominantly down and that the flanks of the salt dome are now incorrectly estimated. The latter point, however, does not account for why the alt dome is so poorly imaged. This is because the smooth velocity model, compare Figure 5.7d with Figures 5.7b and 5.7c.

The final migrated sections are shown in Figure 5.8. Decomposing the wavefields before imaging also significantly improves the imaging results. Interestingly the hydrocarbon reservoir is more clearly imaged using a smooth model while the central salt dome is not imaged at all, even when decomposing wavefields normal to its flanks based on the smooth velocity model. This is probably due to the weak reflectivity of the salt and that the decomposition directions were not completely correct. Overall, the smoothing has blurred out the interfaces slightly and they are now at incorrect depths with respect to the dotted reference. This makes it very difficult to determine which of the two decomposed results is preferable and also highlights that the strengths of decomposing normal to variations in medium parameters strongly depends on the accuracy of the used velocity model. Only when the velocity model is very good, as in the earlier Annerveen examples,

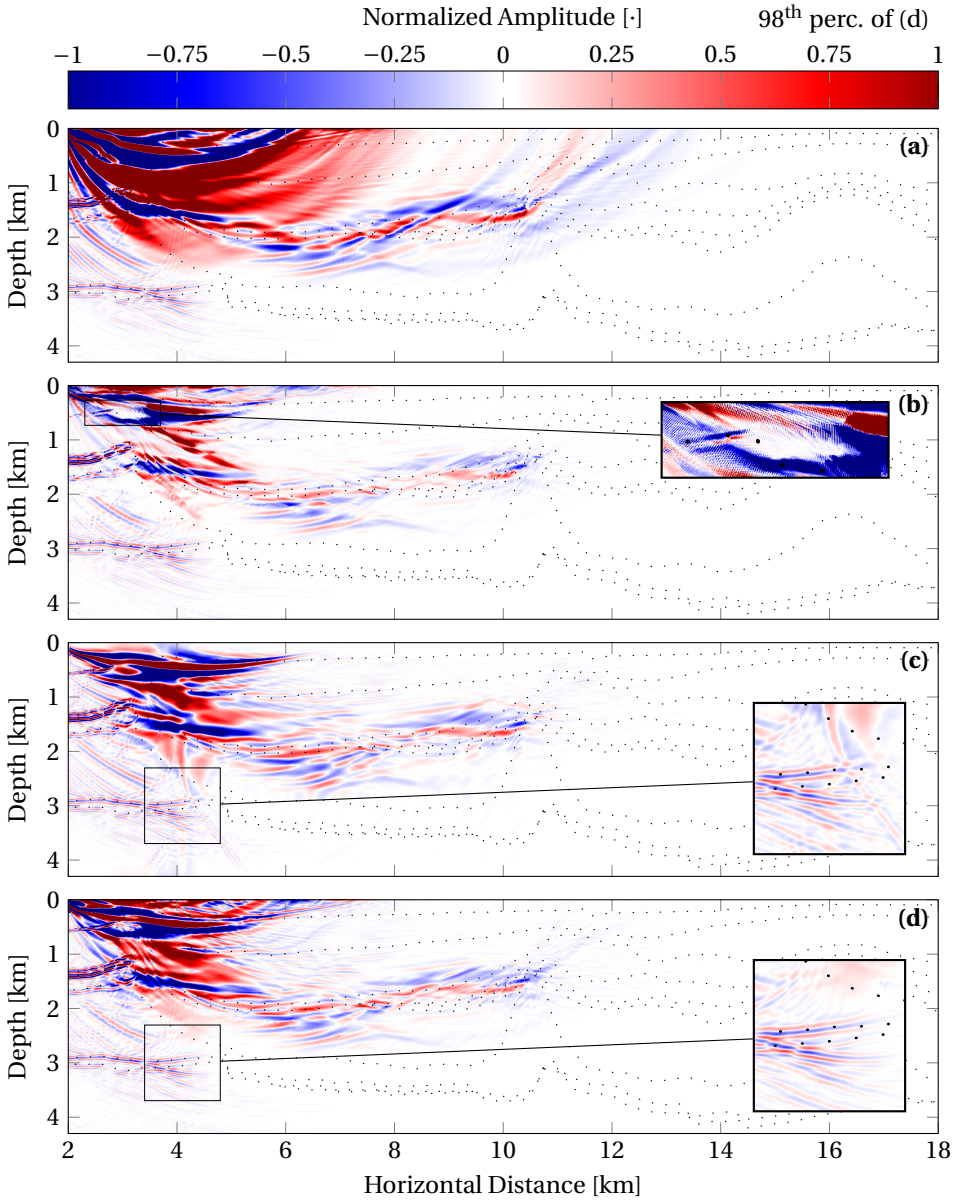

Figure 5.7: Smoothed Annerveen single-shot migration results using conventional RTM (a), Poynting RTM (b), analytic RTM (c), and snapshot RTM (d). Amplitudes have been normalized to the 98th percentile of (d).

can decomposing normal to expected variations in medium parameter help to image interfaces with steep dip.

5.4.5. FIELD DATA EXAMPLE: VØRING AREA

Snapshot decomposition was also applied while reverse time migrating data from the Vøring area in Norway. In this case decomposition only occurred in the vertical direction. The results are compared to conventional RTM in Figure 5.9. Figure 5.9a shows the migrated data without decomposing the wavefield, and as expected it exhibits low-wavenumber artefacts due to dominant back scatter occurring at a depth of 1.25 to 1.75 km. Decomposing the wavefield using snapshot decomposition removes these artefacts, as can be seen in Figure 5.9b. Low vertical wavenumber events, however, remain. They appear to be artefacts as they interfere with other clear reflectors, which they mask. These events can be removed using a 0.0012 to 0.0024 m^{-1} linear vertical low-cut filter, this comes at the expense of losing vertical resolution and damage to surrounding events when it is not certain if these events are actually undesirable. To avoid edge artefacts associated with the filter, the edges were tapered using a 500 m sine squared taper.

5.5. NUMERICAL CONSIDERATIONS

Reverse time migrating data, at the time of writing, is an expensive task, both in computational load as well as storage requirements. As such, much effort is put into optimizing the underlying algorithms. The following analysis directly pertains to the previously discussed images, but is also more broadly valid for finite-difference–based implementations of RTM.

Conventional acoustic RTM zero-lag cross-correlates forward and backward modelled pressure wavefields by multiplying snapshots, see Figure 5.10. To be able to do this often either the forward or backward propagated snapshots are stored in memory, and then multiplied with the backward or forward propagated snapshots in reverse order. As such, memory usage increases during the modelling of the stored wavefield in time and then decreases as the other required wavefield is modelled in time and its snapshots are multiplied with the stored snapshots, after which the stored snapshots are deleted. Figure 5.10 shows this for storing the forward propagated snapshots. Note that the top two processes, top two rounded boxes, on either side of each method can be switched without loss in generality.

When decomposing wavefields it is generally necessary to store additional wavefield information. When decomposing using plane-wave decomposition it is necessary to store snapshots of the pressure wavefield for all times for both the forward and backward modelled wavefields, see Figure 5.10. This effectively means that the entire pressure wavefields have to be stored everywhere in space for all times. After modelling both the forward-modelled and the back-injected wavefields, and storing them, they are plane-wave decomposed. This often involves expensive transposes and memory reordering, hence the additional computation time with respect to conventional RTM in Figure 5.10. This is circumvented using the analytic imaging condition, but comes at the cost of lost decomposition flexibility.

If instead the wavefield is decomposed using snapshot wavefield decomposition, or

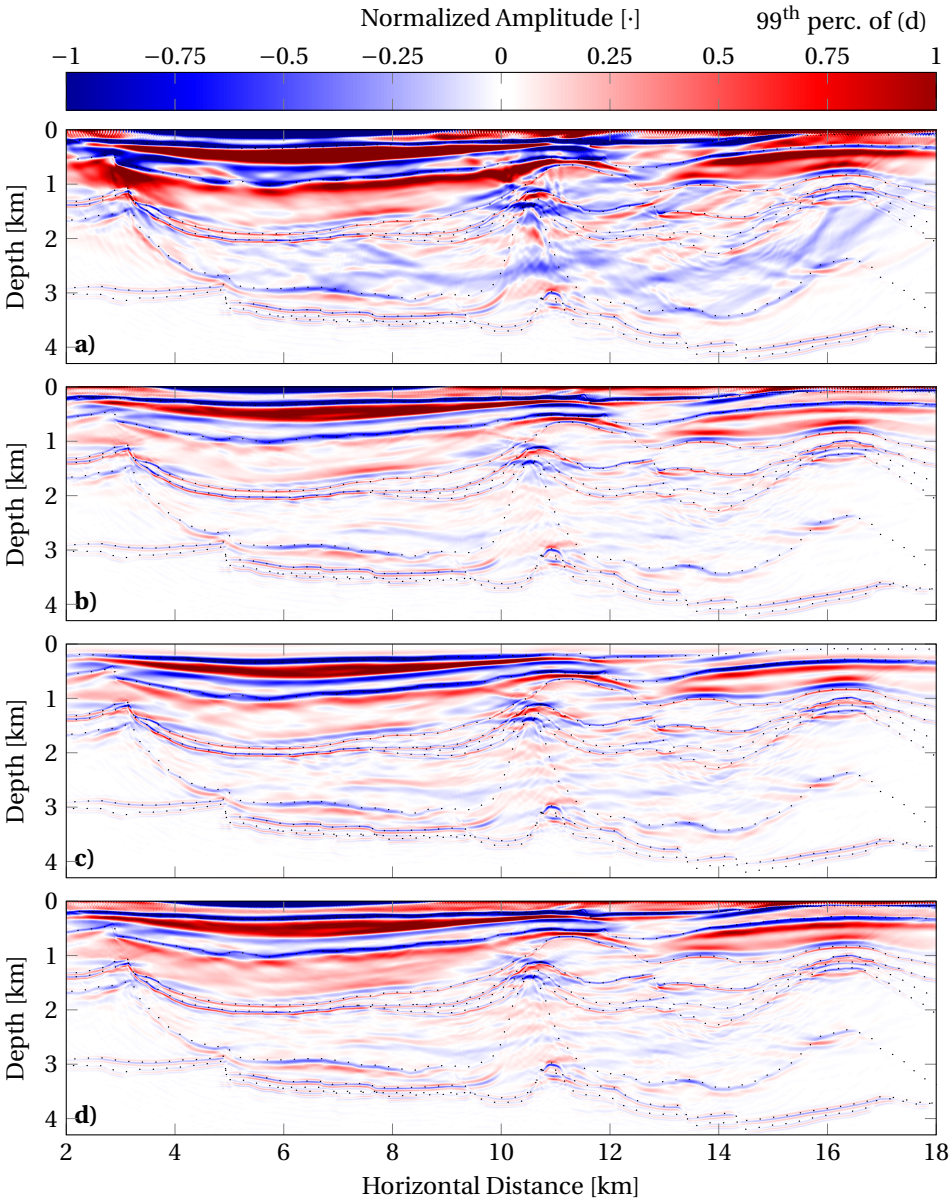

Figure 5.8: Comparison of stacked smoothed Annerveen migration results using conventional RTM (a), Poynting RTM (b), analytic RTM (c), and snapshot decomposition (d). Amplitudes have been normalized to the 99th percentile of (d).

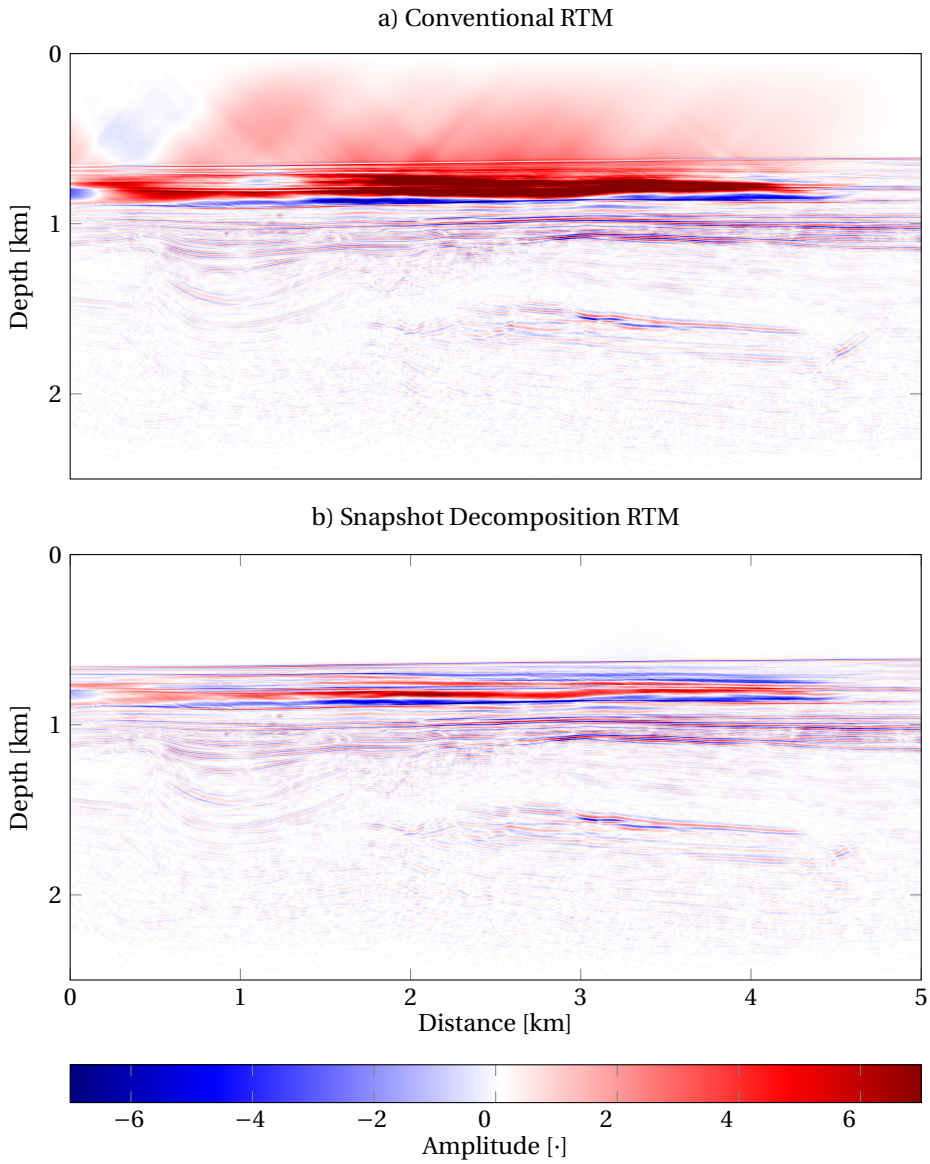

Figure 5.9: Comparison of the Vøring area migration results for an excerpt of the image. a) shows the conventional migration results with the typical back-scatter noise. b) shows the migration results after snapshot decomposition.

crudely using Poynting decomposition, then one must additionally store either the time derivative or the integral of the pressure, or the particle velocity in the direction of decomposition, effectively doubling the acoustic storage cost with respect to conventional acoustic RTM. If the time step between sequential snapshots is small enough then the

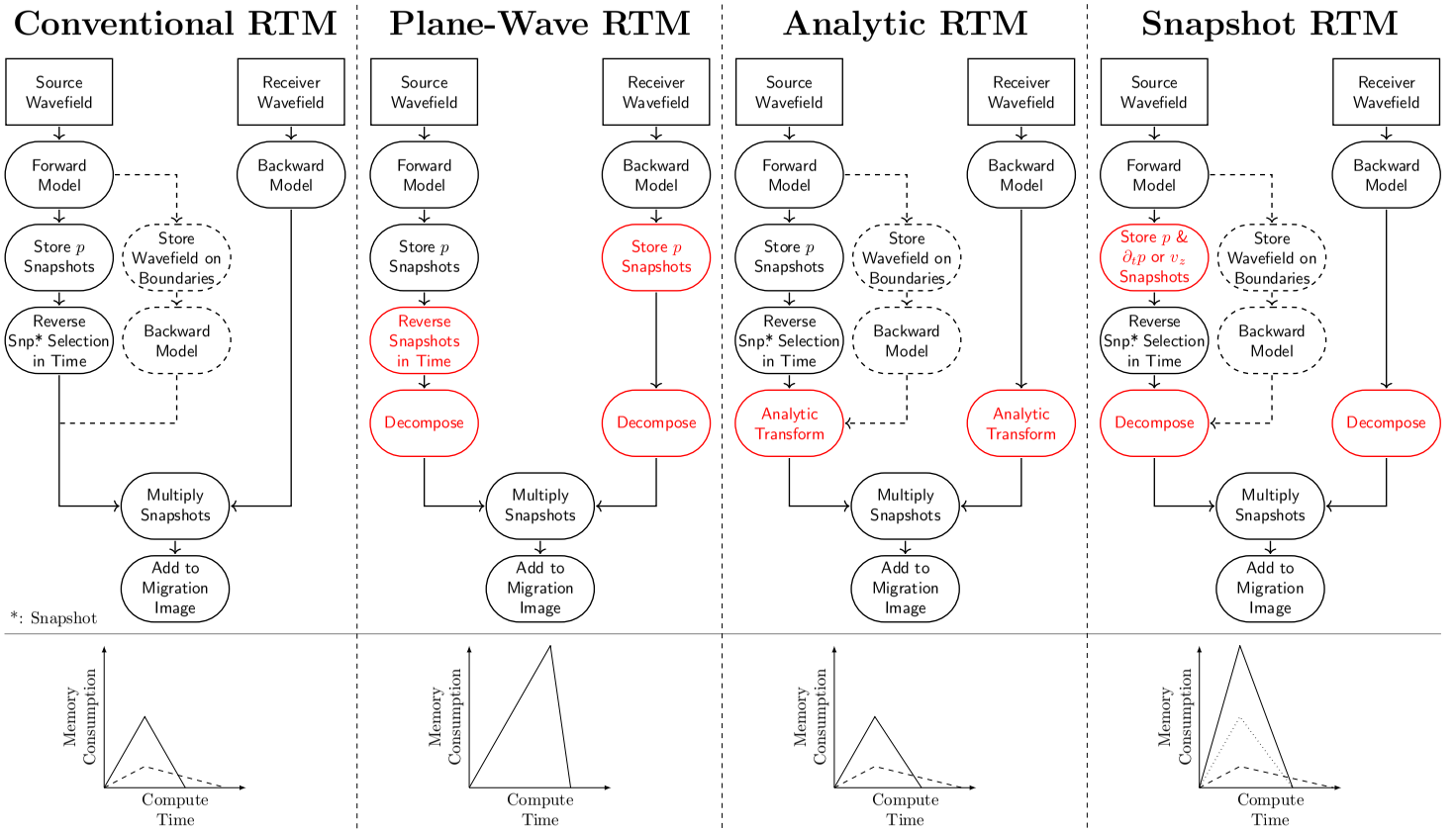

Figure 5.10: Flow charts of the different decomposition RTM schemes as well as indicative sequential memory-versus-time graphs. The solid lines in the bottom graphs denote compute time and memory consumption of the corresponding unbroken flowcharts. The dashed lines correspond to taking the dashed route in the flowchart, while the dotted line under snapshot RTM denote the case where the snapshot time sampling is sufficiently dense to estimate the time derivative of the snapshot from subsequent snapshots.

temporal difference between the snapshots can be used to approximate the necessary derivative. In this case the storage cost does not increase. Furthermore, when back-propagating the wavefield, in comparison to plane-wave decomposition RTM, it is possible to decompose the wavefields while back-propagating, allowing one to multiply decomposed snapshots for imaging while back-propagating wavefields, see Figure 5.10. This can save computation time as expensive memory reorganization is not necessary.

In the previous paragraphs it was assumed that sufficient wavefield snapshots for imaging can be stored in memory, where memory refers to any interfaceable system capable of storing information, like Random Access Memory (RAM), solid-state drives (SSD), Hard-Disk Drives (HDD) and tapes in order of decreasing cost per unit of memory storage. For some problem sizes it is not possible to store all the wavefield snapshots in their native format in RAM, the generally preferred storage medium due to fast access times. In these cases snapshots can be compressed using a variety of techniques, see for example the zfp package by Lindstrom (2014). Note that compressing and decompressing data has a performance penalty and potentially reduces precision due to lossy compression. If the problem size is still too large, data need to be stored using other storage media. There are various techniques beyond the scope of this work to mitigate performance impacts associated with this.

One can further reduce the necessary memory by only storing the forward modelled source wavefield at the boundaries of the modelling domain. When back injecting the recorded data, one back injects the boundary recorded data of the forward modelled wavefield in a different model at the same time, see Figure 5.10. This allows one to multiply the two wavefields to generate the migration image while they are being backward modelled. This greatly reduces memory usage as snapshots no longer need to be stored, however, it comes at the cost of having to model three acoustic wavefields, the forward wavefield, its back injection and the backward-modelled wavefield, which increases computation time by a factor of one and a half. In Figure 5.10 the memory usage for this form of RTM is depicted using dashed lines and is grossly exaggerated for large finite-difference models. The exaggeration is necessary because for growing square models with edge size x, the size required to store snapshots grows with x^2, while the size to store the boundaries only grows with x.

Lastly also note that for very large problem sizes it may be a good idea to distribute the problem over many compute units as RTM is highly parallelisable. In terms of the presented examples, each shot record can be migrated independently using different compute units. This means that total compute time decreases linearly with the available number of identical compute units. Parallelising individual RTM steps is not as fruitful but still can save time, see Amdahl's Law (Amdahl, 1967).

In terms of speed of the algorithms, conventional RTM is the fastest, closely followed by RTM using Poynting decomposition, which predominantly requires additional memory but only very little additional actual compute time. Next fastest is analytic RTM which only requires Fourier transforms in the direction of decomposition. This is significantly slower than conventional RTM due to the Fourier transforms, but it requires nearly no additional memory. Then comes snapshot wavefield decomposition, which is slower but more flexible. This comes at the cost of having to Fourier transform all spatial dimensions. By far the slowest methods are decompositions in the frequency domain, plane-wave de-

compositon for example, as these require expensive numerical transposes to reorganize the data for FFTs along the time axis. This discussion, however, is strongly machine and algorithm dependent. In the future it could well be that higher dimensional Fourier transforms become nearly as fast as one dimensional Fourier transforms due to advances in computational hardware, consider Floating Point Gate Arrays (FPGA) Slade (2013). This would narrow the computation time gap between analytic and snapshot RTM.

5.6. DISCUSSION

Snapshot wavefield decomposition is the ideal decomposition technique when operating on snapshots of a wavefield in time, where the wavefield is known everywhere in space. Snapshot directional wavefield decomposition complements conventional surface-normal wavefield decomposition, which generally works in the horizontal-wavenumber–frequency domain, i.e. one less spatial Fourier transform but an additional temporal Fourier transform. Snapshot directional wavefield decomposition is ideally suited for decomposing wavefields that are being stepped forward in time as they are modelled, as opposed to forward in space when redatuming wavefields. It also allows for the forward and backward directional propagation of wavefields via the eigenvalues of the wave equation.

The snapshot wavefield decomposition operators, which were derived for homogeneous media, also work well for directionally decomposing wavefields in heterogeneous media. Additionally we are free to choose any desired decomposition direction by simply rotating the operation in the wavenumber domain around the origin. This is possible because the method operates in the full wavenumber domain, where the Laplacian is circularly symmetric around the origin. This is not possible for any other decomposition scheme. In the case of conventional surface-normal decomposition, the decomposition direction is restricted to being normal to the surface along which the decomposition occurs. In the case of plane-wave decomposition the axis along which the spatial Fourier transform occurs must be rotated to align it with the desired decomposition direction. For discrete data this may be difficult due to the need for interpolation. If interpolation is done in the wavenumber domain it requires Fourier transforms over all spatial dimensions. In this case one may as well do snapshot wavefield decomposition, which would save the temporal Fourier transform. The same holds for analytic RTM which, for decomposition in a direction that does not correspond to an axis of the coordinate system, should also be done in the full wavenumber domain.

Snapshot decomposition has several important beneficial implications for RTM. It allows for wavefield decomposition on wavefield snapshots, the native wavefield format when time stepping wavefields forward in time in many RTM schemes. This means that for actual wavefield decomposition we no longer have to wait till the modelling of both the forward- and backward-modelled wavefields is finished to decompose the wavefield, or have to additionally model the Hilbert transform of the source and receiver data as in analytic decomposition, see Shen and Albertin (2015). Hence snapshot directional wavefield decomposition has the potential to considerably reduce storage requirements of RTM and compute time, while at the same time keeping the flexibility of an actual decomposition, as opposed to analytic RTM, which does not involve true directional wavefield decomposition.

A further important aspect of snapshot wavefield decomposition was already highlighted in Chapter 2. It can decompose wavefields normal to interfaces, this comes at a much greater numerical cost when naively implemented, but has the potential to greatly improve imaging results as it solves an inherent problem in conventional up-down decomposition RTM. The problem with global up-down decomposition in RTM is the intrinsic assumption that all variations in media of interest are vertical. This is because the reflected wavefields of dipping reflectors may be down-going, which in the case of up-down decomposition would mean that the reflection responses are incorrectly mapped to the transmitted image. When using the reflection-imaging condition these waves would not contribute to the image, even though they should. Snapshot wavefield decomposition has the potential to correct for this by always decomposing normal to interfaces. This allows snapshot-directional-wavefield-decomposition-based imagining to image vertical interfaces, which up-down wavefield-decomposition-based imaging cannot achieve.

Snapshot decomposition, like the other mentioned decomposition schemes, still suffers from the imposed cyclicity of any Fourier transform-based method, as it operates in the wavenumber domain. This causes sharp contrasts in wavefield amplitude, for example due to interfaces, to be aliased, which would lead to incorrect scaling in the wavenumber domain. In the presented figures this effect, however, is very small. We suspect that this is due to the fact that the pressure and its time derivative or integral exhibit the same aliasing, which is similar enough after incorrect scaling to not contribute significant artefacts.

As in Chapter 2 it is imperative that all quantities, like the pressure and particle velocities, are on the same grid in time and space for the decomposition to work properly, otherwise small phase-shifts between signals affect the decomposition results detrimentally. This often requires interpolation of particle velocities onto the same grid as the pressure, which can introduce artefacts. In this work we therefore opt to use the more stable time derivative of the pressure as it is a side product of the forward modelling of the wavefields in RTM. The time integral of the pressure can also be used, and is more stable for the high frequencies, but requires that running integrals of the wavefields during decomposition are stored.

It was noted earlier that the modelling operators commonly used in RTM account for both propagating an evanescent waves. From Chapter 4 it is known that snapshot directional wavefield decomposition does not correctly account for evanescent waves unless their behaviour in the complex wavenumber plane is accounted for. In the presented examples this was not done. As such, evanescent waves were incorrectly accounted for. This is mainly only a problem very near to the source and receivers as the evanescent waves related to deep reflectors are generally recorded below the ambient, in this case numerical, noise floor. Due to the limited numerical precision of the employed modelling operators this means that the RTM scheme cannot take them properly into account, even for the presented examples where the medium was known perfectly. Therefore, the decomposition does not need to be able to take them into account either.

5.7. CONCLUSIONS

We have presented a novel method to decompose wavefield snapshots during RTM imaging. It has been demonstrated that, although it does not give the smoothest images, it

leads to the best reflector imaging and structural detail, see for example the central salt dome in Figure 5.5. In terms of speed it is the third fastest method. Poynting RTM is the fastest by a considerable margin at the cost of also having the lowest image quality. Analytic RTM is the second fastest, only slightly faster than snapshot RTM, while being less flexible. Snapshot-decomposition RTM is the third fastest, being considerably faster than plane-wave RTM, which requires temporal Fourier transforms. Furthermore, snapshot-decomposition RTM under ideal circumstances has the smallest memory footprint as only the wavefield and its time derivative are needed, something naturally computed during modelling. This means that due to its speed and flexibility along with high image quality snapshot-decomposition RTM should be the RTM of choice.

6

CONCLUSIONS & OUTLOOK

6.1. CONCLUSIONS

The main foci of this thesis are (1) the presentation of a novel directional decomposition scheme that works on snapshots of a wavefield and (2) the application of this scheme during Reverse Time Migration (RTM). In Chapter 2 an innovative directional wavefield decomposition method was presented that operates on wavefield snapshots. The novelty here is that the decomposition occurs in the time domain. This makes it unique as the other schemes in the literature work either in the frequency domain (Suprajitno and Greenhalgh, 1985; Wapenaar and Berkhout, 1989) or require the modelling of two related wavefields based on a source and its Hilbert transform in time (Shen and Albertin, 2015). For acoustic wavefields the proposed decomposition, like many of its brethren, is effectuated by the scaled addition of the pressure and the particle-velocity component in the decomposition direction. Unlike the other techniques discussed in this thesis, where the decomposition direction is determined by the problem configuration, the decomposition direction of our method can be chosen freely. This includes varying the decomposition direction spatially, which is made possible by spatially combining the decomposed results from different decomposition directions. Waves travelling orthogonal to the decomposition direction are also accounted for, which is important for correctly accounting for head waves at their generating interfaces. In addition, already decomposed wavefields can be further decomposed, such as decomposing the up-going field into up-left and up-right going wavefields. This corresponds to muting quadrants in the wavenumber domain. The benefit of decomposing wavefields into propagation-direction quadrants is that it allows for finer control of the propagation direction during, for example, imaging.

It should be noted that the snapshot directional wavefield decomposition scheme, as presented in Chapter 2, is in its current numerical implementation only strictly valid for propagating waves in a homogeneous medium. However, it also works very well for heterogeneous media like many of the conventional decomposition techniques. Evanescent waves, however, cannot be taken into account properly yet due to their phase shifts between the pressure and particle velocity in the directions orthogonal to the evanescent directions. In Chapter 4 it was demonstrated that isolated evanescent plane waves

can be correctly accounted for due to their pole behaviour in the complex wavenumber plane, which necessitates the introduction of a phase shift. In more general situations these waves cannot be correctly accounted for and hence the decomposition only yields correct results for propagating waves.

As the decomposition method is to be applied to wavefields during modelling with time-extrapolation operators, which results in theoretically noise-free wavefields (aside from the potential algorithmic and numerical noise inherent in the use of numerical modelling schemes), the decomposition does not suffer from noise in input data. However, noise present in the input data before the data is injected into a model will still result in additional unwanted spurious wavefields during the temporal extrapolation. These spurious wavefields will be correctly directionally decomposed by the scheme, but will still degrade later processing steps that rely on the fact that the input data are noise free, like for example, during the application of an imaging condition.

In Chapter 3 snapshot wavefield decomposition is compared to other techniques. It was found that many schemes are fundamentally similar for propagating waves and only differ in the domains in which they are defined. However, only conventional decomposition, as for example presented by Wapenaar and Berkhout (1989), explicitly accounts for evanescent waves in the vertical direction. To extend snapshot wavefield decomposition to account for evanescent waves it is hypothesized that the non-analytic contributions from the complex wavenumber domain need to be taken into account during the decomposition to allow for the separation of propagating and evanescent waves, such that both can be properly decomposed.

Chapter 4 investigates snapshot directional wavefield decomposition using simple theoretical examples, more precisely the decomposition of propagating and evanescent waves. It is demonstrated that our proposed decomposition breaks down for evanescent waves and needs a special phase rotation to account for these in the wavenumber domain. How to exactly find this phase rotation is not completely understood at this time, it is, however, related to the non-analytic behaviour of the functions in the complex wavenumber plane.

In Chapter 5 snapshot wavefield decomposition is applied to imaging in the context of RTM. RTM is commonly implemented using scattering wavefield modelling operators that advance a wavefield from one time step to the next. Snapshot wavefield decomposition is ideal in this context as it only requires the wavefield and its time derivative everywhere in space at a given instance in time, see Appendix C. These parameters are always present when modelling wavefields using time stepping. Compared to the other decomposition schemes commonly used in the same context it demonstrates similar qualities and often has better performance for nearly vertical structures when decomposing normal to expected contrasts in medium parameters during imaging, see for example the central salt dome in Figure 5.5. For horizontally layered media the performance is equivalent to the conventional schemes used in RTM. It was also demonstrated that snapshot wavefield decomposition during imaging improves RTM results for real data, see Figure 5.9. Snapshot decomposition in this case removed dominant low-wavenumber artefacts. From an implementational point of view snapshot decomposition has memory-requirement advantages and associated compute-time advantages over the other presented decomposition schemes in the context of RTM, see Figure 5.10. This should make

our proposed decomposition scheme the scheme of choice for wavefield decomposition during RTM.

During the work that culminated in this thesis, data were acquired for the imaging of Scholte waves, one of the original goals of this Ph.D. project. Scholte waves, like head waves, are interface bound and have a linear travel-time dependence on the source-receiver distance parallel to the generating interface. It was hoped that some of the head-wave imaging techniques that were to be developed as part of this Ph.D. project could be applied to the recorded Scholte waves. However, they were hardly present in the data. The data were still used for conventional imaging though, including the application of snapshot decomposition during RTM. These results are presented in Appendix A.

6.2. OUTLOOK

The proposed snapshot directional wavefield decomposition scheme, as presented in Chapter 2, does not work for evanescent waves. In Chapter 4 they could have been explicitly accounted for by horizontally phase shifting the data by $\pi/2$ in the wavenumber domain. However, it is still unknown how to generalisably incorporate evanescent waves into the decomposition as evanescent components mix with propagating components for all wavenumbers. It may have to do with the phase alignment between the pressure and the particle velocity. There is still the need to better understand the behaviour of evanescent waves during snapshot decomposition before we can generalize our proposed theory for all types of scalar waves.

Snapshot wavefield decomposition also does not properly take variations in medium parameters into account during decomposition, even when the medium parameters can already be used to define the decomposition direction. Extending the scheme to heterogeneous media would be a big improvement.

Currently the scheme only works for scalar wavefields. It would be interesting to extend it to vectorial wave equations like the elastic or electromagnetic wave equations. For the elastic wave-equation the directional decomposition will most likely be a two step process. First the elastic wavefield is decomposed into pressure and shear potentials, which in an isotropic time- and space-invariant medium satisfy scalar wave equations, followed by a directional decomposition of the potentials akin to the scalar decomposition of acoustic wavefields in Chapter 2. From a purely mathematical point of view it would also be desirable to generalize the concept to arbitrary second-order partial-differential equations. Mathematical examples that may benefit are the Navier-Stokes equations.

During snapshot directional wavefield decomposition the magnitude of the wavenumber vector is used. This term is strongly related to the square root of the Laplacian, or Laplace operator, which is the sum of second order spatial derivatives. Often only the positive principle square root of the Laplacian is considered (Caffarelli and Silvestre, 2007), which results in an integro-differential operator with infinite spatial support. It is, however, suspected that if we choose the signs of the square root similarly to as was done in this work the resulting operator will have quasi-pointwise support, like a conventional differential operator. For our proposed decomposition this would mean that it could be formulated using differential operators and could be done on a local multicomponent receiver basis instead of requiring arrays of receivers for Fourier transforms, as is the case

for traditional wavefield decomposition techniques. This would entail resource savings when one is only interested in directionally decomposing wavefields to understand wavefields at a given location, as imaging and other Fourier domain processing techniques still require dense arrays of receivers. Furthermore, if the decomposition could truly be formulated as a local operation its dependence on medium parameters would simplify to a local dependence, potentially simplifying the decomposition in heterogeneous media.

For wavefield decomposition in RTM the current algorithmic implementation is acceptable, albeit slow, and currently only works for problems with two spatial dimensions. To make the technique truly applicable to real world problems the algorithm has to be extended to three spatial dimensions and sped up. The constraining factors here are the employed Fast Fourier Transforms (FFT), which for sufficiently large problem sizes are still prohibitively slow. A local decomposition operator in the space-time domain should be sought such that the method scales better with increasing problem size and distributed computational resources.

Concerning the original goals of this Ph.D. project, these are still worth chasing. Imaging using head waves still has significant potential, especially because acoustic headwave amplitudes are direct indicators of the density ratios at their generating interfaces. This is a special characteristic of head waves and could in the future aid in better constraining density models, a problematic topic in full waveform inversion for example.

With respect to the Danube survey it would be interesting to return to the site to understand why Scholte waves were hardly present in the recorded data. Shallow coring of the sediments under the Danube could be very revealing as it would inform about the composition of the mud at the bottom of the Danube, which might be responsible for the very weak and slow Scholte waves that were discovered. Coring would also help to better understand the near surface acoustic velocity structure below the Danube. Especially arrays of coring might bring to light why events in the common-midpoint (CMP) gathers often had distinctly non-hyperbolic moveouts. Better understanding the subsurface would allow for an update in the acquisition configuration for a reshoot along the river. Before a reshoot the water depth should be more thoroughly investigated as in some instances acquisition occurred in less than two meters water depth. During a reshoot measures should be put in place to mitigate the generation of tube waves along the streamer and a more robust GPS setup should be sought. The setup in the presented survey generated many tube waves where the streamers were connected and encountered GPS gaps sufficiently large to hamper processing.

All in all this work opens up exciting new possibilities and leaves behind some unanswered questions. We hope that the developed snapshot directional wavefield decomposition scheme will find ample application in better understanding wavefields as they evolve in complex models and in imaging according to expected variations in media, instead of simply in the vertical direction.

ACKNOWLEDGEMENTS

Foremost I would like to sincerely thank the most instrumental people in this Ph.D. project, my two promoters **Guy Drijkoningen** and **Kees Wapenaar**. Acknowledging that my Ph.D. project was an arduous process that evolved over time due to the discovery of snapshot directional wavefield decomposition, I wish to express my deepest gratitude for your ceaseless support throughout, be it through your continuous guidance, Guy's Tuesday meetings, as well as enabling me to go on field work or drawing attention to the limitations of my wavefield decomposition. It has been an honour, privilege and pleasure to work with you.

I am genuinely grateful to my family for standing by me all these years. Your unwavering support was a font of motivation and inspiration. *Liebe Eltern, danke dass ihr immer an mich geglaubt habt und auch zuweilen ein strenges Wort für mich gefunden habt.* My two sisters, Cora and Leonie, also helped to keep me on my path. I wish Cora all the best with her doctorate and Leonie with her architectural career.

Regarding my esteemed professors and post-doctoral colleagues, I would like to thank them for the many interesting discussions we have had. Jan Thorbecke was an immense computational inspiration. Evert was of great mathematical help, especially in complex analysis. Giovanni M., Joost, Kees, Deyan and Dieter, thank you for always being open minded to my convoluted, even baffling queries. I would like to mention Auke, Ranajit and Wim for the many instructive chats we had regarding seismic processing and geophysics in general. I also enjoyed the witty corridor conversations with Karl-Heinz and Läslo and Giovanni B.

The Danube fieldwork was an amazing experience. A special thanks goes here to Marinko, Marco, and Mike for making this fieldwork come to life. Marinko, we could not have done it without you and your students, especially Marko who later did his M.Sc. thesis with me. A special thank you also goes to Deltares for supplying the equipment for the survey and to our wonderful technicians Marco and Mike, or M&M.

I also wish to mention my esteemed Ph.D. committee. Thank you for taking the time and patience to read through this work. Your feedback was instrumental to guaranteeing the quality of this thesis.

Now to my friends and colleagues. Thank you so much for the great last years. We have had many crazy lunchtime discussions, drinks close and near to the faculty and many a fun outing. We have had fun times at conferences and our two company visits in Stavanger, Norway, and Cambridge, The United Kingdom. Now for you individual acknowledgements, and I hope I have not forgotten anybody, otherwise I apologise in advance. Here is the list of names in which you should find yourself: Fill in your forgotten name, Rémi, Carlos, Joeri, Pawan, Boris, Niels, Andreas, Ranjani, Siddarth, Runhai, Iris, Amarjeet, Myrna, Sixue, Musab, Reuben, Apostolos, Jan-Willem, Asiya, Helena, Quinten, Jianhuan, Timothy, Giovanni, Koen, Johno, Shohei, Florencia, Dieter, Navid, Kevin, Joost, Guus, Elmer, Shotaro, Kees, Anne, Pieter, Sara, Abdulrachman, Gil, Rodolfo,

Thais, Mikhail, Lisanne, Ralph, Shahar, Samantha, Xiaoxi, Andrea,Tomohide, Alex, Pierre-Olivier, Barbara, Karim, Faezeh, Axel, Laura, Milad, Olivier, Garbiel, Faezeh, Yohei, Rik, Jingming, Milad, Christian, Atsushi, Iban, Menno, Alex, Jinyu, Cees, Gabrio, Alok, Amerjeet, Nihed, Xander, Lisanne, Billy, Sean, Aydin, Karlien, Amin, Aleks, Menno, Martha, Santosh, Baptiste, Alex, Aulia, Ozkan, Rita, Liang, Christian, Torre, Sian, Maria, Youwei, Yohei, Bingkun, Akil, Emilio, Xu, Junhai, Jianye, Nicolas, Aukje, Lele, Feng, Hamed, Izzy. Thank you so much everyone for being part of my life, especially Rémi who was there for me from the beginning to the end of my Ph.D.

I also want to thank the (board)game crew, for amazing afternoons and nights of intense recovery from work. I will not forget our modified rule set for Heroica, nor the fun Dungeons and Dragons sessions with Jambz, The Captain, Florenzia, Barthandalus and the Dungeon Master. Thank you for these great memories.

To all the friends I have had through the phases of my life I would like to thank the kind souls I met in Stade, Ashwicken, Antwerp, Zürich, Bremen, Delft, Aachen and the world over. My special thanks go to Jacob (thank you for being there from the start, literally), David, Misha, Pieter, Stefano, Alex, Rickmer, Shawn, Ben, Eivind, Niels, Eva, Chabeli, Stefanie, and Jasmine.

I also cannot forget the D.O.G.S. (Delft Organization of Geophysics Students), of which I was president for three years. Thank you Asiya, Andreas, Pawan, Boris and Niels for handing it over to me in 2014. During my presidency I have had the pleasure of working together with various boards. These consisted partially of the aforementioned and additionally of Iris, Ranjani, Sixue, Matteo, Reuben, Myrna, Christian, and Lisanne. Thank you everyone, especially Marko, for helping make the D.O.G.S. a summit level chapter.

I would like to close by thanking those that made this PhD project possible through the provision of funds, data and/or software. I want to thank the Netherlands research centre for Integrated Solid Earth Science (ISES), a now defunct research sponsor, for sponsoring this PhD work. Furthermore I would like to thank Equinor for openly providing the Barents sea dataset and Carlos Almagro Vidal for providing me with the Annerveen model shown in this thesis. I would also like to thank Jan Thorbecke for his acoustic/elastic finite-difference wavefield modelling code, Fdelmodc, without which most of this work would have been less feasible. The same goes for the Seismic Unix processing package, maintained by the Colorado School Of Mines.

Thank you for all your support,

Max Enno Holicki

Appendices

A

P*S- and P-Wave Acquisition and Processing of Riverine (Danube) Data near Fruška Gora

Previous research by Allouche (2011) had demonstrated the presence of surface- and shear-head-wave like waves along fluid-solid boundaries in recordings in the Danube. These mode-converted waves travel along the river bottom due to an evanescent acoustic wavefield, excited by an air-gun, in the flowing river. Their travel time varies linearly with respect to their point of excitation. In the case of the Danube this point is below the airgun on the river bottom where the evanescent acoustic wavefield in the water first mode converts to a propagating wavefield. Due to these promising results an additional survey with more channels, denser receiver spacing and longer offsets was conducted downriver in the region around Fruška Gora, next to Novi Sad, Serbia. The survey had two primary aims, the further investigation of the aforementioned mode-converted waves as well as generating interpretable P-wave migrated sections to better constrain the geology of the area. During the survey, for unknown reasons, hardly any mode-converted waves were recorded. This made the processing of the data in the context of imaging critically refracted S-wave events impossible. The data, however, could still be processed to attain interpretable migrated P-wave sections below the river. In this appendix we show how the P-wave data were processed, including reverse time migration results using snapshot wavefield decomposition, and present final transects for the whole survey. These sections are now available for further geological interpretation.

A

A.1. P*S WAVES & THE FRUŠKA GORA SURVEY

This survey was meant to be a further validation of a method presented in the Ph.D. thesis by Allouche (2011). Allouche worked on elastic mode conversions of evanescent acoustic waves at fluid-solid interfaces, resulting in Scholte waves, a type of surface wave. Allouche et al. (2011) demonstrated and described the existence of P*S waves, a special type of mode converted wave. She also found them in real streamer data during surveys on the Danube, see Drijkoningen et al. (2012). In classical earthquake seismology P-waves correspond to the compressional wavefield after the decomposition of an elastic wavefield into one P-wave and two shear-wave potentials, called SH for horizontal shear and SV for vertical shear. The sum of the shear potentials corresponds to the shearing component of the elastic wavefield and its waves are called shear-waves, or S-waves. With respect to a single interface, PS-waves are used to refer to incident P-waves that mode-convert at the interface to S-waves. Due to classical ray theory, see Aki and Richards (2002) for example, this PS notation is only strictly valid for geometric waves, i.e. waves that obey Snell's law for real angles. The * denotes that the P-wave in question is an evanescent wave, which obeys Snell's law for complex angles, that mode-converts to a propagating shear wave. The different possible conversion modes of a spherical acoustic wavefield, in a homogeneous fluid medium, impinging on a solid medium are shown as wavefronts in Figure A.1.

Of particular interest here are the mode-converted waves, the PS-waves in the lower half of the figure. They can be categorized into three types: 1) head-wave-like geometric PS waves, which propagate with a constant magnitude of the horizontal slowness, and are denoted as fast and slow PS-Waves; 2) the geometric component of the PS-wavefield whose traveltime is not linear with offset is denoted by the geometric wavefront in Figure A.1; and 3) the labelled non-geometric component of the PS-wavefield, drawn as a dashed wavefront. This non-geometric wavefield decays exponentially with distance away from the onset of geometric propagation along the ray path, see for example Allouche et al. (2011). At the interface this wavefield is related to the Scholte wave, drawn approximately since its propagation speed slightly differs from the S-wave velocity, and its associated leaky-wave mode, which is not shown. The Scholte wave is excited along the fluid-solid interface by the incident wavefield, and travels radially away from the source along the interface, similar to other surface waves like the Rayleigh or Stoneley waves. The travel speed of the Scholte waves can be exactly determined for a stratified medium using expressions given by de Hoop and van der Hijden (1984, 1985).

To be able to image with these non-geometric waves and the associated Scholte waves a shallow riverine survey was designed and conducted north of Fruška Gora, Serbia. The survey site was chosen due geological interest in Fruška Gora, one of the scattered island mountains in the Pannonian basin, and because it is downstream of the previous suvery, which was near Kulcs, Hungary. The new survey was therefore expected to occur under similar circumstances, and indeed the river was only slightly wider and the river depth of 5–15 m was similar. The major expected geological difference was that locally near Fruška Gora the rocks are metamorphic which could result in a different sediment composition.

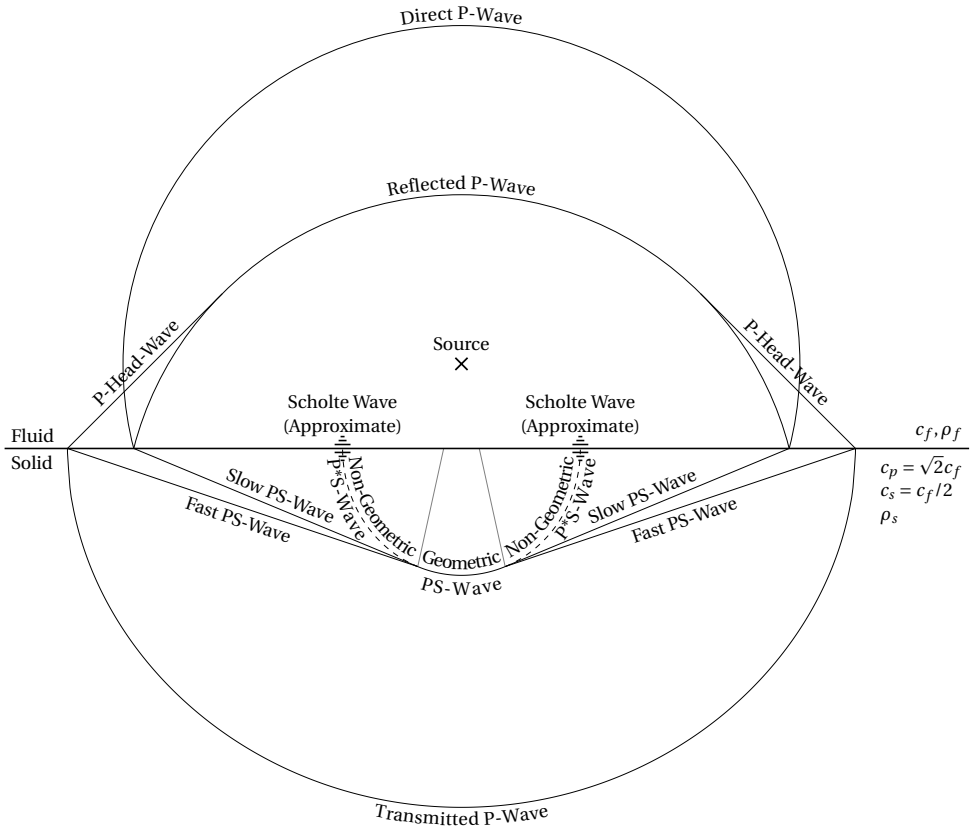

Figure A.1: Wavefronts of expected waves excited by a source, whose location is marked by a cross, in a solid-fluid double half-space model. c_f corresponds to the acoustic propagation speed in the fluid, while c_p and c_s correspond to the P-wave and S-wave propagation speeds in the solid. The fluid and solid mass densities are indicated by ρ_f and ρ_s respectively. Note that the Scholte-wave traveltimes are only approximate in relation to the other traveltimes.

A.1.1. AIMS OF THE P*S SURVEY

The primary aim of the P*S portion of the survey was to acquire mode-converted waves. As these strongly depend on the water depth a shallow river was needed for the survey. After acquisition of these data, the data were to be processed into an image of the subsurface, see for example Drijkoningen et al. (2015), and further analysed.

This survey differed from the earlier Danube survey in Hungary by Allouche (2011) in that a longer streamer configuration as well as a denser streamer configuration were used to acquire mode-converted waves. The longer streamer would be used to find areas with a good P*S/Scholte wave response. Note that both configurations made use of the same three 24-channel 3.125 m-spacing monocomponent acoustic pressure streamers.

P*S- and associated Scholte waves at quasi-horizontal interfaces, when recorded using horizontal acquisition arrays, exhibit quasi-linear moveout on common shot gathers. For this reason it was hoped to apply head-wave based imaging techniques to the

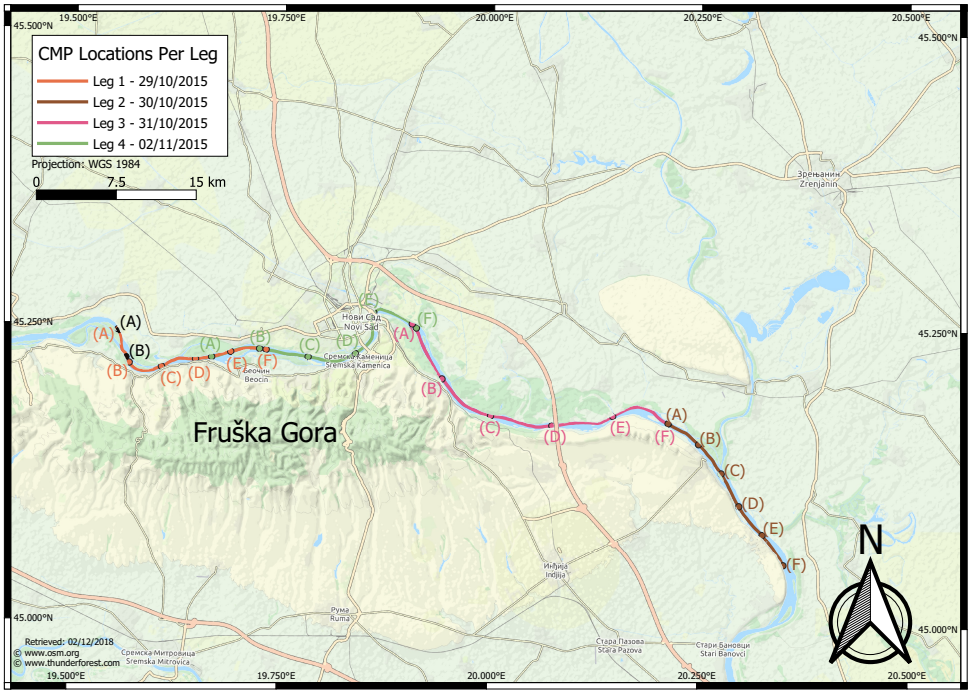

Figure A.2: Map of the Fruška Gora survey area. The coloured lines represent the different seismic legs of the survey. The letters denote the start and endpoints of segments of the legs. The black letters correspond to an echo-sounder leg. The base map, including topography, water bodies and roads, was made by Thunderforest, a project operated by Gravitystorm Limited, based on OpenStreetMap data. The actual map was made using QGIS (QGIS Development Team, 2018).

P*S/Scholte waves, as they exhibit the same quasi-linear moveout, see **Holicki** and Drijkoningen (2016).

A.1.2. AIMS OF THE P-WAVE SURVEY

The P*S survey would naturally also record P-waves, which are ideal for subsurface imaging due to well established processes, see for example Yilmaz (2001).The survey site around Fruška Gora, Serbia, was chosen due to its interesting geological history, see for example Matenco and Radivojević (2012) and Toljić et al. (2013). Fruška Gora is an inselberg, approximately 80 km long and 15 km wide at its widest. It can be seen as the mountain south of Novi Sad, Serbia, south of the Danube as shown in Figure A.2. The structure is oriented West to East, and is bounded on the north and east by the Danube. It appears to extend further east under the Danube, possibly bending to the north-east. This, however, is poorly constrained. As such, the target of the survey was to seismically image under the Danube to better constrain the geology of the area. The final tracks used for the geological part of the survey can be seen in Figure A.2.

A.2. DATA ACQUISITION

The survey was conducted over a fourteen-day period, from 26/10/2015[1] to 08/11/2015. During the first three days acquisition equipment was deployed on a rented vessel and pontoon. The following five days were used to test the equipment and record data for the geological part of the survey as P-wave data acquisition is robust and well understood. The following three days were used to record P*S and associated Scholte waves with a densely sampled streamer array at different offsets. We call this the converted leg of the survey as opposed to the geological leg which was the first five days. The last two survey days were used to acquire simultaneous-source data, where multiple sources fire at different times during the recording of a shot record. On the last day the equipment was disassembled and loaded off the vessel.

The survey acquisition equipment consisted of several 20 in^3 airguns, an airgun controller, a compressor, a generator, three 75 m 24-channel streamers, two Global Positioning System (GPS) recorders, one dual-frequency-band echo-sounder and four acquisition Personal Computers (PC) connected to an Uninterruptible Power Supply (UPS). Three of these PCs were used to record the seismic data while the other was used to record the echo-sounder data and the GPS position. The UPS was there to guarantee computer-side data acquisition in the event of a power loss. An overview of the acquisition pontoon can be seen in Figure A.3.

A.2.1. GPS DATA ACQUISITION

To accurately locate the seismic data the GPS location of the boat was tracked. Figure A.3 shows the relative positions of the two employed GPS recorders on the vessel. The echo-sound GPS was used to calibrate the time of the echo-sound recordings while the seismic GPS was used for positioning and time-synchronisation of the seismic data. The airgun and streamer were towed behind the platform at the back of the pontoon. The back of the platform had a 13m offset along the length of the pontoon with respect to the seismic GPS (red in the figure).

The GPS data were recorded every second using 8-bit American Standard Code for Information Interchange (ASCII, ISO/IEC 8859) via a serial link between the GPS and computer. The recorded data is in the World Geodetic System (WGS) 1984 coordinate system; the standard for many GPS devices that primarily use the GPS satellite network of the United States of America (USA). The horizontal error of the civilian GPS is about 7.8 m at 95% confidence according to the USA government (Department of Defense, 2008). Note that no satellite signal records were kept to later correct the GPS locations using public synthetic base stations to improve accuracy.

A.2.2. ACQUISITION OF THE ECHO-SOUNDER DATA

The echo-sounder used during the survey was a dual-frequency-band KEL (Knudsen Engineering Limited) 120179. Echo-sounders work like zero-offset seismic, i.e. a transducer emits an acoustic wavefield that is scattered back by surrounding reflectors and is recorded by the transducer after a short transducer dead time, where the transducer changes from being a source to being a receiver. The basic idea is that the recorded signal

[1] Date Format: Day/Month/Year (Gregorian Calendar)

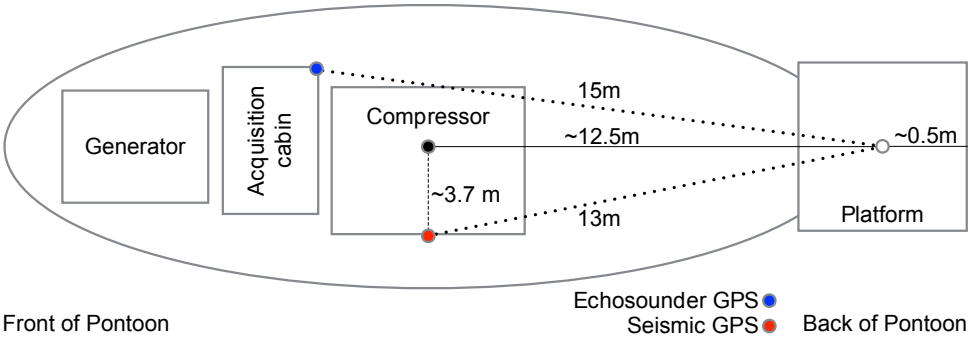

Figure A.3: Photograph of the pontoon and tugboat (top). Diagram of the pontoon (bottom) on which the acquisition equipment was located during the survey. The boat during the survey was at the front of the pontoon, while the streamers were dragged behind the pontoon.

is assumed to only come from the depth direction and, as such, is projected into the vertical and converted to depth using a given acoustic velocity. The first major event per trace is then assumed to be the water bottom, as it is expected to be the strongest reflector.

In this survey a chirp system was used that emits a chirp in two frequency bands with central frequencies of 33 kHz and 210 kHz. This theoretically allows the system to image below the water bottom. During the survey only the 33 kHz channel was used. The chirp was corrected for by the device.

A.2.3. ACQUISITION OF THE SEISMIC DATA

Although three 75 m streamers were used in this survey, these were not dragged next to each other behind the pontoon as is common in large scale 3D seismic surveys. During the geological part of the survey they were placed behind each other to create one effec-

tive streamer with a length of 225 m. This was done as seismic velocity analysis requires larger offsets for longer recording times. These streamers had 24 channels each with a receiver spacing of 3.125 m. For the converted leg of the survey denser streamer spacing was desired, as such, the streamers were dragged directly next to each other and offset by 1 m each in the streamer direction. Ideally this should have been one third of 3.125 m such that an effective streamer is obtained with a length of 77.08 m and a receiver spacing of 1.042 m.

The analogue streamer data were recorded using three 24-channel Geodes^{TM}, each connected to its own PC. The Geode corresponding to the nearest offsets had no gain applied while the other streamers had a 12 dB gain. Recording was triggered in parallel via a signal from the airgun controller, the airgun would then fire a couple of milliseconds later. Computer times were synchronized over an Ethernet-based local area network to within one second.

Data were recorded for 2.5 s at a sampling rate of 0.5 ms, resulting in 5000 recorded time samples for each shot record. The data were recorded using the SEG-D format, see *SEG-D, Rev 3.1* (2015) for the latest revision, to hard drives inside the computers.

A.3. PROCESSING OF THE ACQUIRED DATA

Preliminary data processing occurred in the field. This mostly consisted of quality control of the data. Back in the Netherlands, data processing began in earnest. First the GPS data were processed to locate the acquired seismic data. Then the seismic data were processed. In tandem the echo-sounder data were processed to understand the water depths in the region.

A.3.1. PROCESSING OF THE GPS DATA

During the survey GPS positioning was sometimes intermittent due to recording too few GPS satellite signals. Sometimes only four satellites were available, which is the minimum for GPS positioning on Earth. This led to intermittent GPS tracks which needed post-processing.

The first processing step was to detect where the GPS location remained stationary, as this is unexpected on a moving vessel, and the GPS was sufficiently sensitive to pick up centimetre-scale relative changes in position. The gaps in the data were then corrected in two phases. In the first phase gaps of less than ten seconds, equating to ten gps positions, were algorithmically detected and interpolated. In the second phase larger gaps were interpolated manually.

During the first phase the gaps were interpolated using a five-point weighted orthogonal least-squares fit of the neighbouring five points to either side of the gap. Orthogonal regression is also known as total regression in statistics, or more specifically for the two dimensional case as bilinear or Deming regression (Deming, 1943). The effect this has is that the best fit line minimizes the distance of the line to the fitting points, whereas simple linear regression only minimizes the error in terms of one of the coordinates. As such orthogonal regression is better for the interpolation of GPS coordinates as errors can occur in both latitude and longitude.

The used weights decreased linearly away from the gap, i.e. weight $w = 1 - (i-1)/6$,

where i is the point index starting at one away from the gap. This allowed the fit to perform better at the start and end of turns of the boat.

During the second correction phase the remaining gaps were interpolated using either orthogonal regression, splines or Bezier curves. For bigger gaps the boat speed before and after the gap was additionally estimated to constrain the arc length of the gap for interpolation.

Special attention was given to leg four where the GPS coordinates were missing at the start. This meant that the GPS location could not be interpolated, but had to be extrapolated for this part of the survey. As such, the absolute location data are uncertain by at least tens of meters, but the relative coordinates are certain to within five meters.

After correcting remaining gaps the GPS data were pruned for outliers, these often occurred around gaps. Pruning was done using an iterative approach by moving an eleven-point window over the location data. For each window the best-fit line was estimated using weighted orthogonal least-squares excluding the centre of the window. If the perpendicular distance of the point to the estimated line was at least twice as large as the average perpendicular distance of the other points in the line then the point was flagged as an outlier. In the next step, small groups of outliers with less than ten consecutive members were fitted using the same bilinear regression technique. Larger groups were interpolated using again either least-squares perpendicular offset line fitting, splines or Bezier curves. To smooth out any remaining kinks in the data the same eleven-point-window detection algorithm was used to interpolate their window centres over the entire line. The final result was a smooth GPS track which could be used to interpolate location data and apply geometries to the seismic data.

A.3.2. PROCESSING OF THE ECHO-SOUNDER DATA

The processing of the echo-sounder data began by converting the echo-sounder data, which was stored in the proprietary ".keb" format to SEG-Y Rev. 0 files, see SEG-Y_r2.0: SEG-Y revision 2.0 Data Exchange format (2017) for the latest revision, using the Knudsen conversion tool in the PostSurvey™ software package[2]. The many datasets were then concatenated and erroneous recordings were deleted to create long lines per survey day, which were truncated to match the recorded seismic spatially.

An example of the processed Echo-sounder data can be seen in Figure A.4, which shows the first kilometre of the seismic acquisition line from 29/10/2015. Note that where the data are purely black no river bottom was detected and the data were muted.

A.4. SEISMIC PROCESSING

Workflow A.1 shows the P-wave processing workflow that resulted in geologically interpretable migrated sections.

A.4.1. DATA CONVERSION & EDITING

Processing the seismic data began with converting the seismic data, stored in the SEG-D format, see *SEG-D, Rev 3.1* (2015) for the latest revision, to seismic unix files using the "segdread" function from the seismic unix package (Cohen and Stockwell, 2008). After

[2] https://knudseneng.com/software/postsurvey (Accessed: 04/12/2018)

P-Wave Processing Workflow

1. Data Conversion & Editing
   - Converting SEG-D to SEG-Y to SU
   - Concatenating streamer data sets
   - Pruning for mistriggered and missing shots
   - Approximately time correcting for mistriggered shots on the first streamer
2. Geometry Construction & Assignment
   - Retrieving recorded shot times
   - Constructing distance metric based on boat path
   - Interpolating source, receiver & CMP locations based on shot times
   - Estimating streamer slip and offset correcting data
   - Assigning geometry
3. Polarity Reversal, Trace Kill & Source Trigger-Time Differences
   - Reversing inconsistent trace polarities
   - Removing 50 Hz-dominated traces
   - Sorting to common-offset gathers
   - Picking and aligning first breaks and correcting for mistriggers or delayed triggers
4. Filtering, Gaining & Temporal Truncation
   - Filtering using a $\cos^2$ bandpass filter 50–100–150–200 Hz
   - Gaining in offset and time
   - Truncating Data to 1 s
5. NMO Velocity Analysis & Velocity Model Building
   - Sorting to CMP-Offset
   - Semblance analysis & constant velocity panels
   - NMO velocity picking & model interpolation per CMP
6. NMO Correction, Mute & Stack
   - NMO correction, stretch muting & stacking
   - Alpha trim during stacking for 02/11/2015
7. Pre-Stack Time Migration & Image Stack
   - NMO velocity model interpolation
   - Kirchhoff pre-stack time migration
   - Stacking images
8. Pre-Stack Depth Migration (RTM) with Snapshot Decomposition & Image Stack
   - Converting RMS velocity model to depth (Dix's equation)
   - Smoothing velocity model in time & space
   - Reverse-time migrating with snapshot decomposition
9. Image Post-Processing
   - FK filtering & trace balancing

Workflow A.1: P-wave processing workflow.

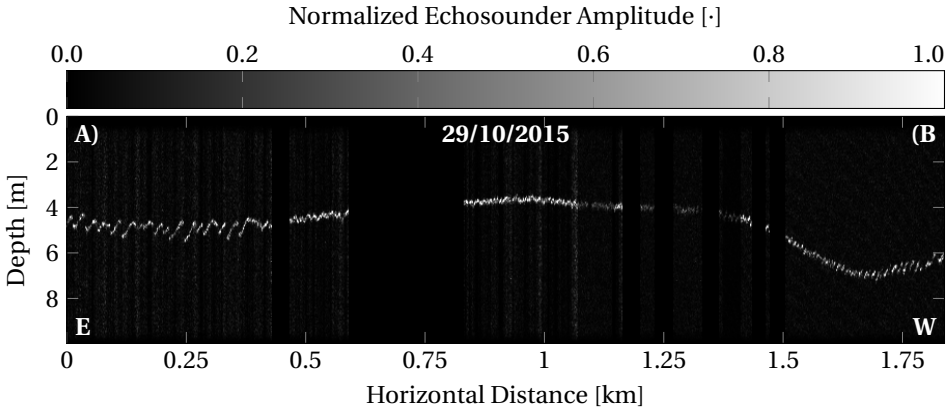

Figure A.4: Example of echo-sounder data from 29/10/2015. For the start and the end of the section see Figure A.2.

that the data were edited for misfired shots. If no data were recorded, i.e. only noise was recorded, the data pertaining to that field record number were deleted. Because of the fact that the survey used three streamers, hooked up to three different computers for data recording, mismatches in field record number were frequent. These were accounted for based on the trigger time. After editing the data the three datasets were concatenated into one effective streamer.

A.4.2. GEOMETRY CONSTRUCTION & ASSIGNMENT

The next processing step was to set the location information in the trace headers of the data. To this end the shot times of the trace headers needed to be extracted. These were then used to interpolate the source location based on the known source offset with respect to the back of the boat, whose GPS location was known. As this survey was 2D and the boat was moving up-stream it is acceptable to assume that the airgun, the source for this survey, was dragged behind in the wake of the boat, and thus followed the same GPS track. Given the source location, and the known offsets of the start of the streamers it was then also possible to interpolate the individual receiver locations inside the streamer, which had a receiver spacing of 3.125 m. Based on the interpolated source and receiver locations Common-Mid Points (CMPs) were calculated.

Having computed the acquisition geometry it was assigned to the seismic metadata, the SEG-Y trace headers. During this process it was noticed that some of the streamer offsets with respect to the pontoon were inconsistent with recorded shots. The actual offsets were determined by Linear MoveOut (LMO) correcting the data with a constant velocity of 1,500 m/s. It was found that the error was generally around a multiple of 3.1 m, which is approximately the streamer spacing. For the third leg this meant that four offsets were duplicated, see Figure A.5.

It was also found out later during processing that during the third leg the streamer started to slip at some point as common offset traveltimes started to increase from shot to shot. This streamer slip was manually corrected for earlier in the processing flow, Step

2.

A.4.3. POLARITY REVERSAL, TRACE KILL & SOURCE TRIGGER-TIME DIFFERENCES

Another acquisition-related processing step was to correct source timing for individual shots as the airgun firing time was inconsistent with respect to the trigger time. Figure A.6a shows a Common-Offset Gather (COG) with inconsistent direct-wave arrival times. Correcting for this was a two-step process. First the traveltime differences were corrected in the following way. The waveform of the direct wave was estimated for each trace, under the constraint that the waveform is not allowed to vary significantly from one trace to another in the nearest-offset COG to the source. This allowed for automatic time shifting of the traces. The method, however, was not perfect and sometimes the picked times were not accurate, requiring manual adjustment as the second step. Correcting for the variable airgun firing delay in Figure A.6a) resulted in Figure A.6b).

Figure A.6 clearly shows a multiple with a period of 0.05 s, corresponding to a one-way distance of 37.5 m in water with an acoustic velocity of 1,500 m s^{-1}. This is unlikely to be a river bottom multiple, as the river bottom depth ranged from 4 to 16 m, nor is it riverbank multiple, as the river was about 600 m wide. This is further corroborated by the fact that the source-to-riverbank distance was not constant, which would have resulted in multiples with a non-constant first arrival and period. The most likely candidate to explain this phenomenon is the inherent bubble pulse of airguns, with common periods in the order of 10–100 ms (Zhang et al., 2017), which fits the 50 ms period of the multiple. The 50 ms period does seem too long for the high-frequency airgun used in this survey though. Another possible option is a resonance induced inside the streamer.

As this event did not seem to contaminate the later produced stacks it was not removed. Initially attempts were made to remove it using gapped Wiener filtering, which due to the lower-frequency content of the event did not work well. Multiple estimation and removal was also attempted but did not work well for the same reason.

Figure A.6 shows that the first event arrived at about 0.026 s. Since the panels are approximately zero-offset there is a 0.026 s trigger time delay before the airgun fires. This was accounted for later in the processing flow, just before velocity analysis, by time shifting all traces by 0.026 s.

A.4.4. NOISE & ABSENT P*S / SCHOLTE WAVES

The data were now essentially ready for P- and P*S-wave processing. Sadly though, P*S-waves were scarce. We do not know why this was the case. A part of the reason could be due to the strong low-frequency noise in the data. Figure A.7 shows a low-pass filtered record using a $\cos^2$ taper from 50–100 Hz. The low frequency wave, indicated as a Scholte wave, exhibits the typical dispersive behaviour of surface waves while travelling at a speed of 60 to 70 m s^{-1}. For our data near Fruška Gora it is only clearly visible on the second streamer and only in this frequency band. It is much weaker at higher frequencies. On the first streamer it is obscured by noise, while it is only partially recorded at the end of the section on the third streamer.

The absence of P*S waves and associated Scholte waves from practically all shots in the survey came as quite a surprise. An earlier survey further up the Danube in Hungary

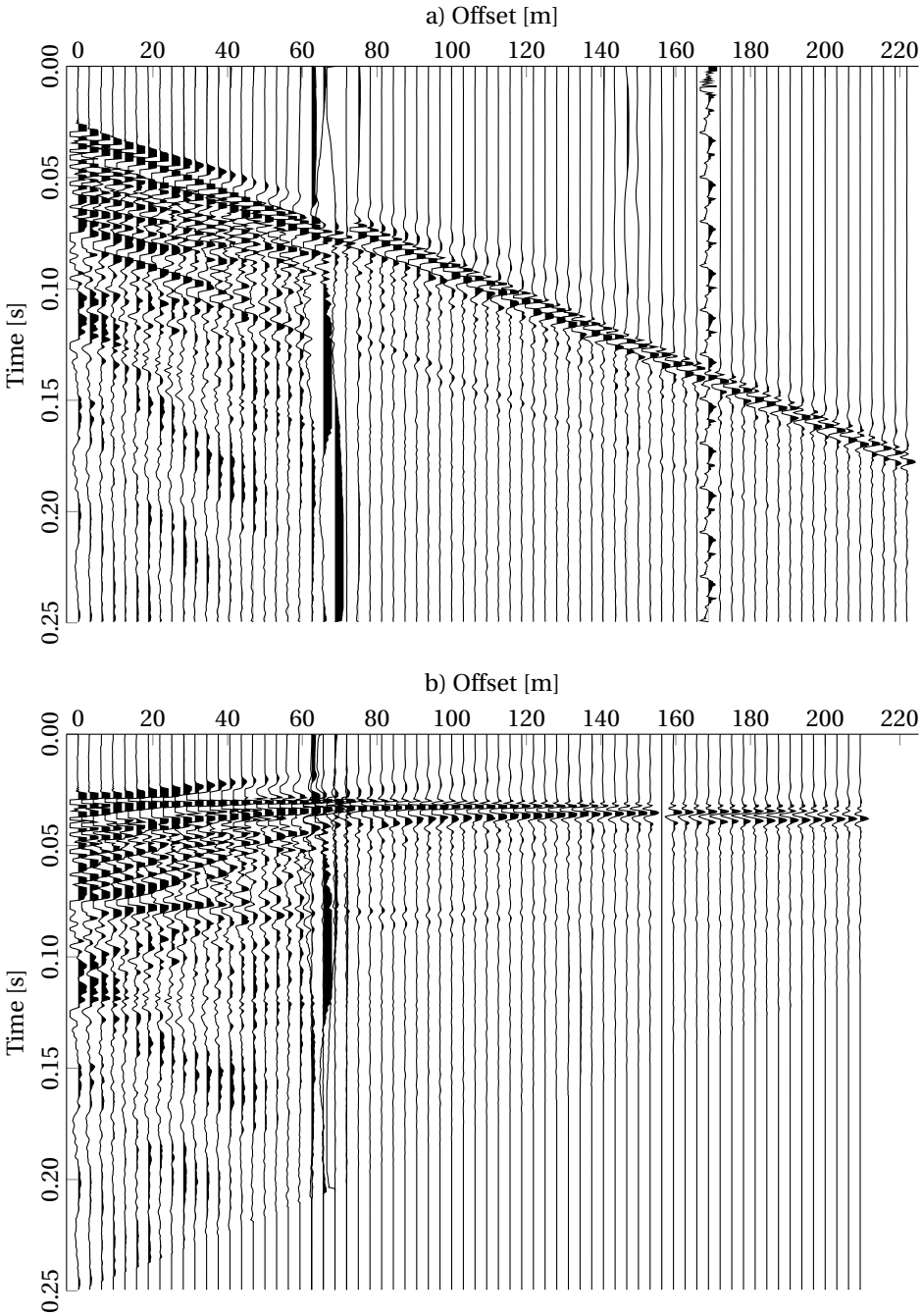

Figure A.5: Common shot gathers of the first shot from the third leg (31/10/2015). A) shows an uncorrected gather while B) shows the same gather after offset, polarity and LMO correction.

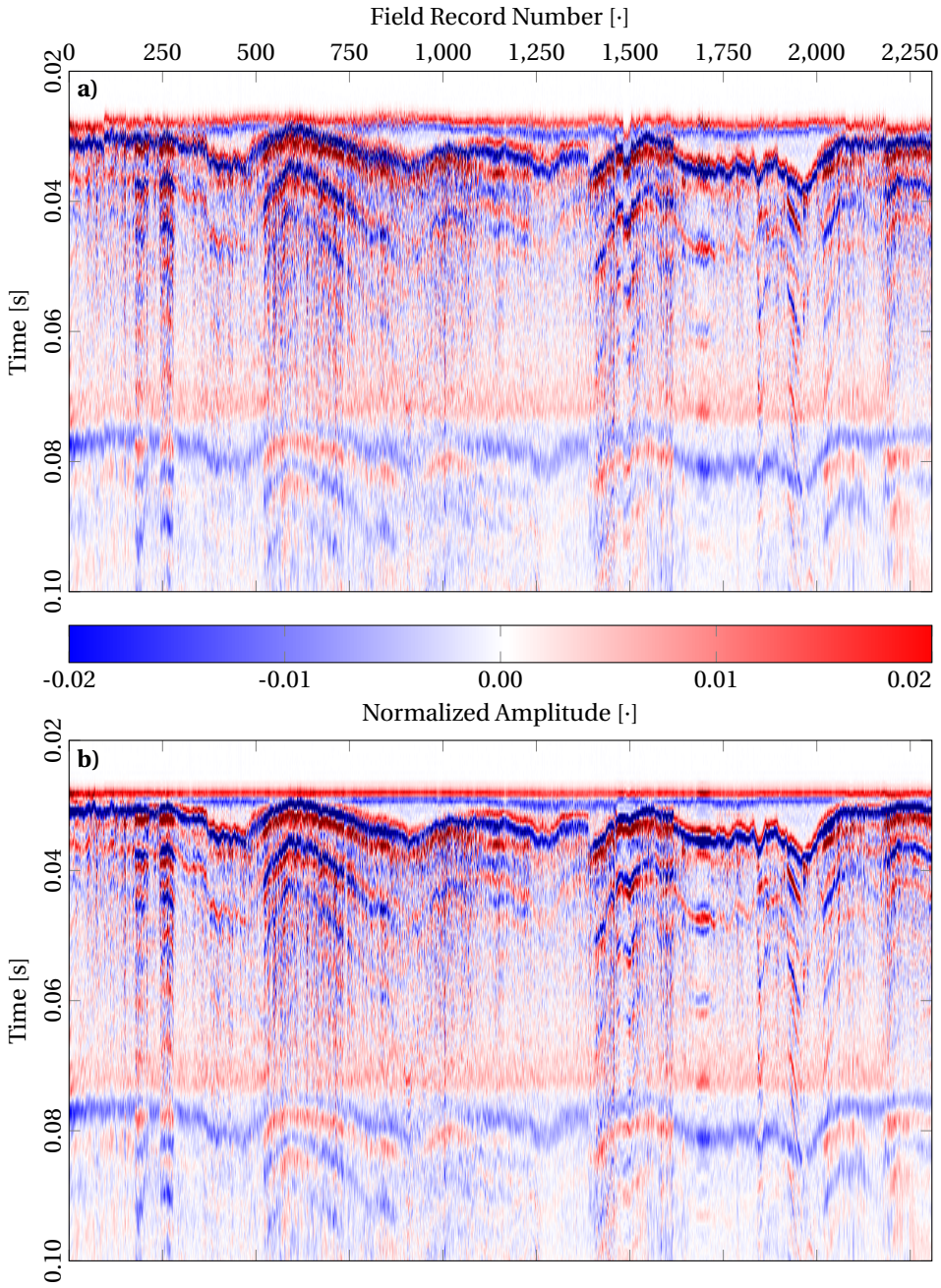

Figure A.6: Nearest common-offset gather from 31/10/2015 with uncorrected (a) and corrected (b) direct-wave arrival times.

had very clear records of Scholte waves (Drijkoningen et al., 2012). They were directly visible and dominant on the raw records, as can be seen in Figure A.8. Apart from the greatly diminished amplitudes in the newer survey, the Scholte waves in the newer survey has a much stronger dispersive behaviour than the Scholte waves recorded in the past.

The dominant noise source in Figure A.7 below 50 Hz is also indicated in the figure as a tube wave. Tube waves are waves that travel along cylindrical bodies, like streamers. They have a linear moveout. On the first streamer they generally travelled towards the source, as seen in Figure A.7, while on the third streamer they tended to travel away from the source. On the second streamer they travelled in both directions. During the survey it was noted these were predominantly generated where, due to water drag, the streamers were slapping against each other.

Tube-wave removal was attempted by filtering individual streamers in the wavenumber-frequency domain, but 24 channels per streamer were not sufficient to do this well. For this reason, and the difficulty of finding good Scholte-wave recordings, P*S-wave imaging as a processing goal was abandoned. The data were further P-wave processed into geologically relevant sections.

A.4.5. FILTERING, GAINING & TEMPORAL TRUNCATION

As most of the noise sources were dominant in the low-frequency band, see Figure A.7, the data were low-cut filtered using a cosine-squared taper from 50 Hz to 100 Hz. This filter removed a lot of the noise while not affecting the P-wave signal too harshly. The desired S-waves and/or Scholte waves, should they have been present, would have been filtered out by such a filter. In Figure A.9 are the frequency spectra of ten consecutive shots, suggesting that the airgun did not produce significant energy above 500 Hz. This is in line with the rest of the dataset and, as such, the data were high-cut filtered using a cosine-squared taper from 500 Hz to 600 Hz. Additionally for the final stacks it was found that a frequency range of 50–100–150–200 Hz produced the best results. Higher frequencies did not stack well after NMO.

Beyond tube-wave removal, the horizontal-wavenumber-frequency domain was also investigated for the removal of shear waves, like Scholte waves, based on their apparent velocity. Due to the limited number of channels and irregular receiver spacing between streamers, this was not further pursued.

Before velocity analysis of the binned data the data were gained. An offset-dependent amplitude gain was applied to approximately account for geometrical spreading while an exponential gain, $\exp(at)$, with a being the gain constant, was applied to account for amplitude decay due to absorption over time. Finally the traces were trace balanced based on the RMS of their amplitudes for better event detection in the upcoming semblance analysis. Then the data were reduced to 1 second as no primary reflections were seen beyond this time in the data.

A.4.6. NMO VELOCITY ANALYSIS & VELOCITY MODEL BUILDING

The data were now binned into 6.25 m CMP bins. 6.25 m bin spacing ensured that there were generally at least 48 traces per bin and more than 100 m offset for the first three legs, which improved the stacking power of the CMPs. For the fourth leg only one streamer

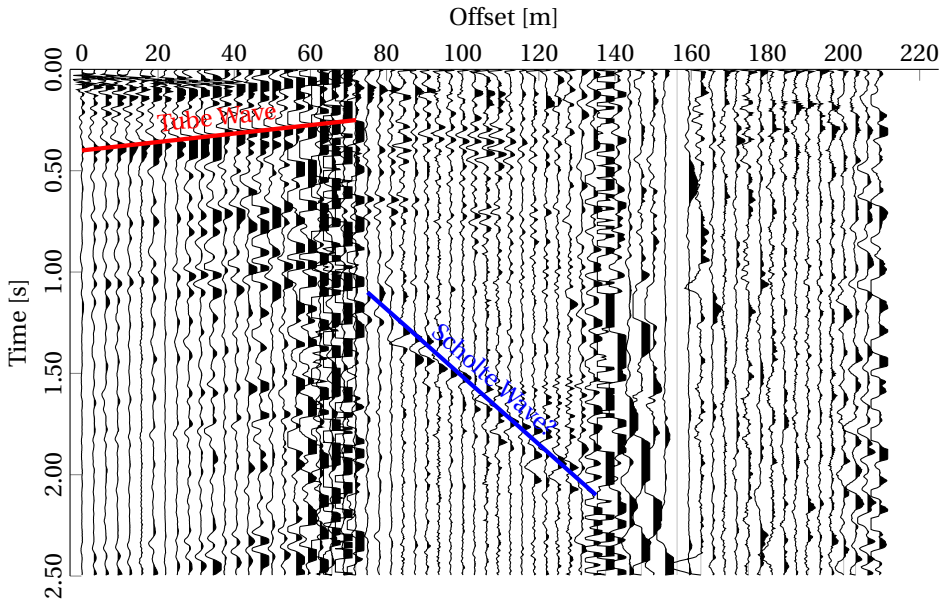

Figure A.7: High-cut filtered (50 Hz to 100 Hz) shot record showing tube-wave noise (one event marked in red) especially observable on the first streamer, channels 1 to 24. Additionally there is an event (marked in blue) travelling at about 60-70 m s−1 which is interpreted as a Scholte wave.

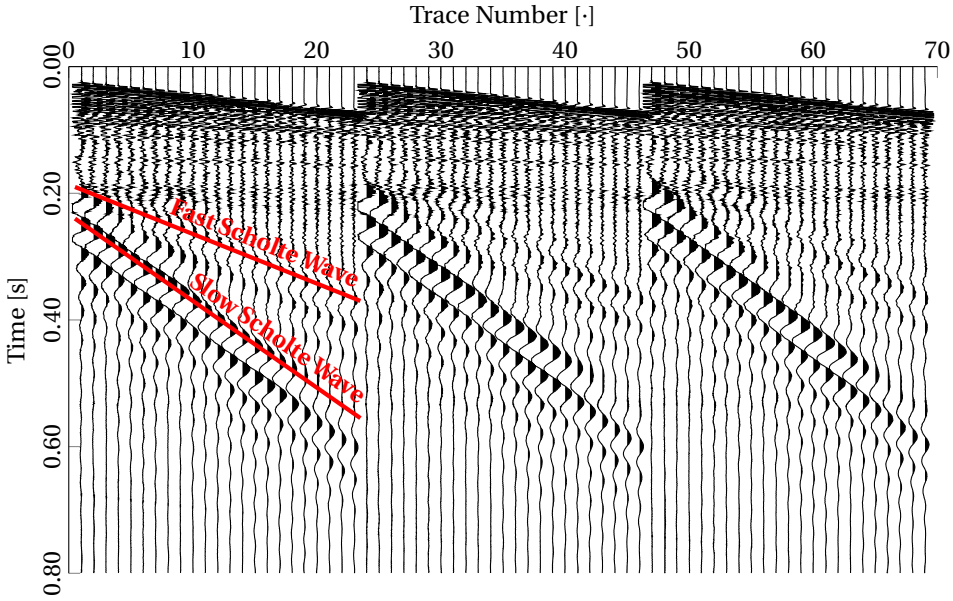

Figure A.8: Example of clear Scholte waves on three consecutive raw shot records from an earlier survey further up the Danube in Hungary (Drijkoningen et al., 2012).They are the two visible low-frequency events on the section (marked in red), one faster than the other.

was used due to waterway regulations. However, the bin size of 6.25 m was retained even though this meant that NMO velocity analysis was severely limited.

NMO velocity analysis was now performed on the CMP-binned data. It was found that best results were obtained using very simple velocity models and only with offsets less than 75 m. Figure A.10 shows a typical CMP gather and associated weighted semblance. The weighted semblance was computed according to Luo and Hale (2012). In the CMP gather on the left it is very difficult to discern individual reflections. There are weak reflections with an acoustic water velocity of 1,500 m s^{-1} around 0.25 s. These are suspected to be two out-of-plane riverside reflections, with a rough riverside-to-boat distance of 150 m to 200 m. As can be seen for this CMP gather, picking velocities was very difficult due to the significant amount of undesired non-inline events on the panels, as well as the fact that many of the P-wave events did not seem to have a hyperbolic moveout.

A.4.7. NMO CORRECTION, MUTE & STACK

After picking smooth RMS velocity models for the legs the data were NMO corrected, stretch muted and stacked to generate geologically interpretable quasi-zero-offset sections. NMO stacking was done using a cosine-squared NMO-stretch mute window based on the stretch factor of NMO times. Here the stretch factor S is defined as:

$$S = \frac{\sqrt{t_0^2 + \left(\frac{x_{\text{cmp}}}{c_{\text{rms}}(t_0)}\right)^2}}{t_0} - 1 \tag{A.1}$$

where t_0 is the zero-offset arrival time, x_{cmp} is the source-receiver distance inside the CMP gather and $c_{\text{rms}}(t_0)$ is the RMS velocity as a function of the zero-offset arrival time. Tapering began for stretch factors greater than 0.45 and ended for stretch factors greater than 0.55, past which all events were muted. For the data from 29/10/2015 an alpha trim of 0.2 was additionally used during stacking to remove outliers. To denoise the resultant stacks the data were again filtered using the same 50-100-150-200 Hz cosine-squared taper and trace-balanced over the entire stack.

A.4.8. PRE-STACK TIME MIGRATION & IMAGE STACK

Stacking NMO-corrected traces is only approximately correct. More correct is to migrate the data. As such, the picked velocity model was used to apply pre-stack Kirchhoff time migration to the data. This was done using the CREWES Matlab™ function "kirkshot" (Margrave and Lamoureux, 2019). After migration the image gathers were stacked with an alpha trim of 0.2. The resultant images were filtered using the same 50-100-150-200 Hz taper and trace balanced.

A.4.9. PRE-STACK DEPTH MIGRATION (RTM) WITH SNAPSHOT DECOMPOSITION & IMAGE STACK

In order to see whether the wavefield decomposition as developed in Chapter 5 would improve the imaging, the data were also reverse-time migrated. The picked NMO velocity model, however, is in time. To convert it into a depth velocity model Dix's equation (Yilmaz, 2001) was used to first compute interval velocities.

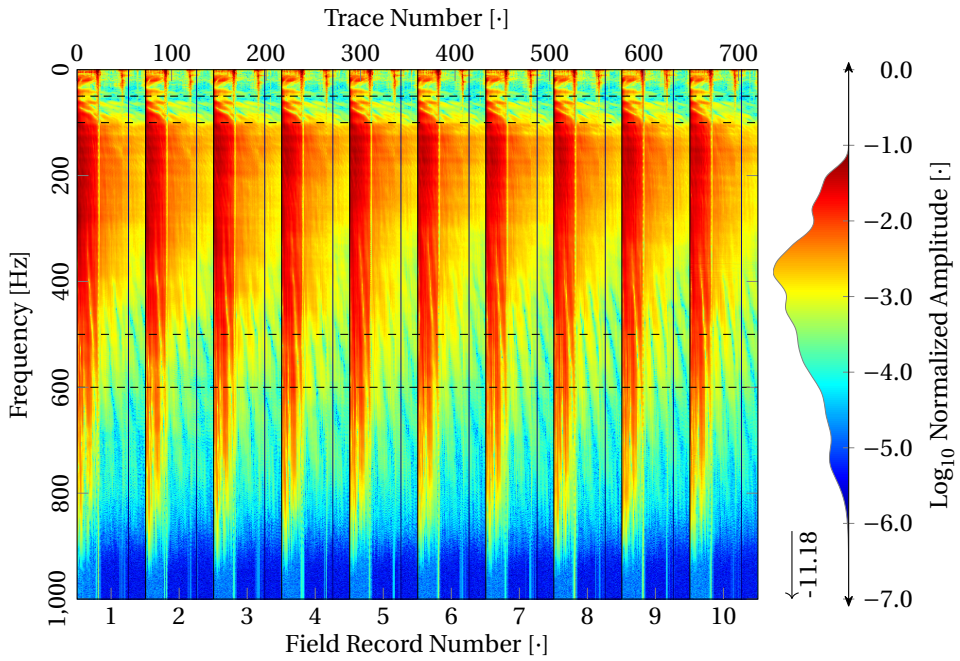

Figure A.9: Amplitude spectra of the first ten shots from the third leg. The densely dashed lines indicate the the outer bounds of the applied $\cos^2$ taper, while the coarsely dashed lines indicate the inner bounds.

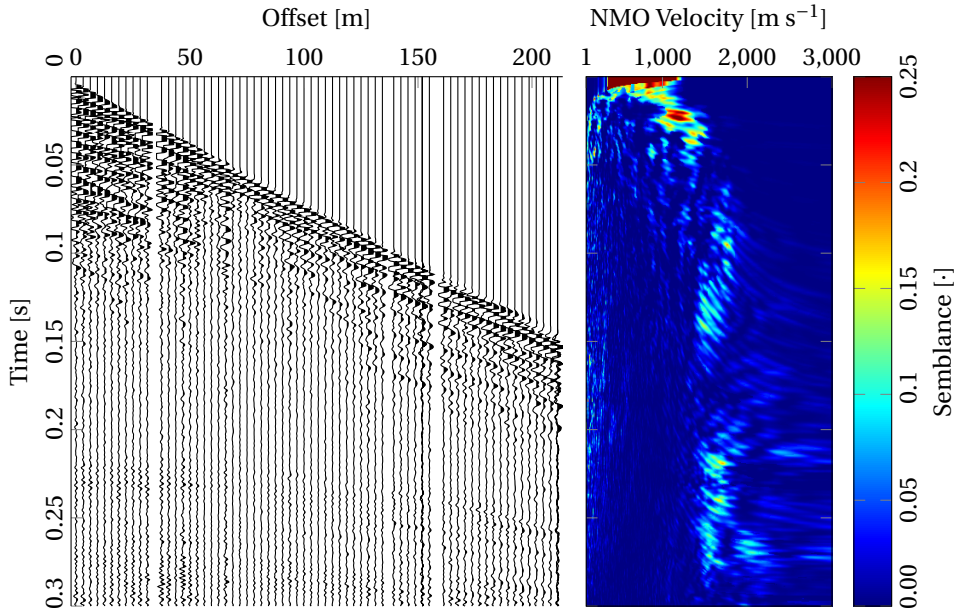

Figure A.10: CMP gather from 31/10/2015 (left) and its NMO semblance (right). The two reflections below 0.2 s are probably two cross-line reflections from the riversides, roughly 150 m to 200 m to either side of the boat.

A point of attention with Dix's equation is that where the RMS velocity gradient decreases the interval velocity also decreases, leading to possibly unintentional low velocities. To convert the interpolated RMS velocity model to interval velocities, each time sample was individually converted. The resultant interval velocity model in time was smoothed before it was converted, in a one dimensional sense, to a depth velocity model. The resultant model was smoothed again and was then interpolated to a one-meter spacing for reverse-time migration with snapshot wavefield decomposition as described in Chapter 5.

A.5. RESULTS

In Figure A.11 the resultant sections from the processing described above are shown. It compares a generated NMO stack to its time and depth migrated images respectively. The Kirchoff Pre-Stack Time Migrated (PSTM) image and the NMO stack in this figure have qualitatively similar event continuity and slightly out perform each other in different parts of the sections. For example event continuity is superior on the NMO stack between 0.1–0.2 s and 3.0–4.5 km. The RTM image has generally worse event continuity and overall slightly more noise due to the aliased source sampling. Its vertical axis, however, is depth, not time.

In the end the NMO stacks were chosen to be the best for structural interpretation. They have the best overall event continuity and more distinct events can be seen on the NMO stacks than in the migrated images. Therefore we will only give the NMO stacks for all the other tracks for geological interpretation. Due to the less coherent nature of the depth image we do not consider it to be the best for structural interpretation, the Kirchoff images on the other hand are acceptable.

For a comparison on whether snapshot directional wavefield decomposition, as discussed in Chapters 2 and 5, improved imaging we consider Figure A.12. It shows in the left panel the RTM image for the shot without snapshot decomposition before imaging. The centre panel shows the RTM with snapshot decomposition and the right panel shows the difference between the two. Note that the data were gained using a linear gain from zero to one hundred at the bottom. We can see that the two RTM images are very similar. Wavefield decomposition did not significantly improve the image in this case. The difference panel shows that there is a difference resulting in a possible improvement of the image. Note though that amplitudes were further boosted by a factor of three to make them comparable. The same structures are visible in all three panels, suggesting that the decomposition mostly affected amplitudes, although some phase effects are present. This makes sense considering the smoothness of the velocity model in Figure A.11. The only back-scattered events that could occur were diving waves. For the very-near-offset data these would predominantly occur at the top of the panels. This is also where we see the largest difference in results. Hence these panels show that for the interpretability of the sections the decomposition in this instance made little difference.

We now present the other legs beginning with the first NMO stacked section from 29/10/2015. This section was processed by Vanić (2016) as part of his M.Sc. thesis, as such the processing flow deviates slightly from the one described here. Note that the data were not further pre-stack time migrated nor depth migrated.

Figure A.13 represents the best generated stacks, based on the best quality data from

the survey. Initially the same processing flow as for this stack was applied to the rest of the data. The results, however, were not comparable in quality. As such, adjustments were made to the processing flow. The NMO stacked result for 30/10/2015 can be seen in Figure A.14. The stack has overall a lower quality than the former stacked section, Figure A.13. The stacked sections for the other tracks can be seen in Figures A.15 and A.16.

A.6. DISCUSSION

This survey was fraught with many challenges. Originally it was designed for detecting and recording P*S/Scholte waves, but for unknown reasons these are hardly present in the data. They were either masked by the strong low-frequency noise in the data, although the noise was not as strong for all channels, or the P*S/Scholte waves were not sufficiently generated in the subsurface. A possible explanation, see Vanić (2016), is a thick mud layer on top of the river bottom with a very low S-wave velocity. Very slowly travelling waves, interpreted as P*S-waves were found during the survey, see Figure A.7, however, no direct proof of a thick mud layer was found. Evidence of dragging the streamer through the mud at the bottom of the river was found though, suggesting the presence of a mud layer at the bottom of the river for a part of the survey. This is not conclusive though, and as such we do not know why P*S/Scholte waves were not consistently recorded during the survey. They were present every day during an earlier 200 km Danube survey in Hungary (Drijkoningen et al., 2012), as can be seen in Figure A.8. The interpreted Scholte waves for this survey travelled considerably faster than those found in the current survey.

The aforementioned low-frequency noise below 100 Hz, like the tube waves, was also a challenge for processing the P-wave data. Seismic energy was clearly present in this frequency range, however, it was not possible to separate it from other coherent noise. A plausible cause for the noise is a potential flaw with the streamer design, in which the three streamers were towed next to each other at different offsets in the streamer direction with the idea to combine them into one effective streamer later. To keep offsets consistent the streamers were right next to each other at the back of the acquisition pontoon. This close proximity caused the streamers to slap against each other everywhere along the streamers during acquisition. This was observed directly behind the platform on the pontoon and also supported by the tube waves generated where the streamers were attached to each other. This effect started nearly immediately after the first shots were fired. The streamers slapping against each other around channels 24 and 48 predominantly caused tube waves to propagate along the streamer. For the first streamer they propagated towards the acquisition vessel, a direction which could have been muted in the frequency-wavenumber domain; however, 24 channels per streamer were not sufficient for good filtering in such a way.

A challenge with this dataset was the boat speed. On average the boat travelled at 4.5 m s^{-1} upstream along the Danube. Due to regulations, vessels are not allowed to manoeuvre so slowly as to appear stationary. The Danube flow speed during the survey was about 1.5–2.0 m s^{-1}. This caused drag along the streamers, pulling them off the end of the boat. This resulted in offsets of the far-offset streamers to slowly increase from shot to shot. This could only be approximately accounted for during later processing.

A related issue was that the source spacing was quite large due to the boat speed

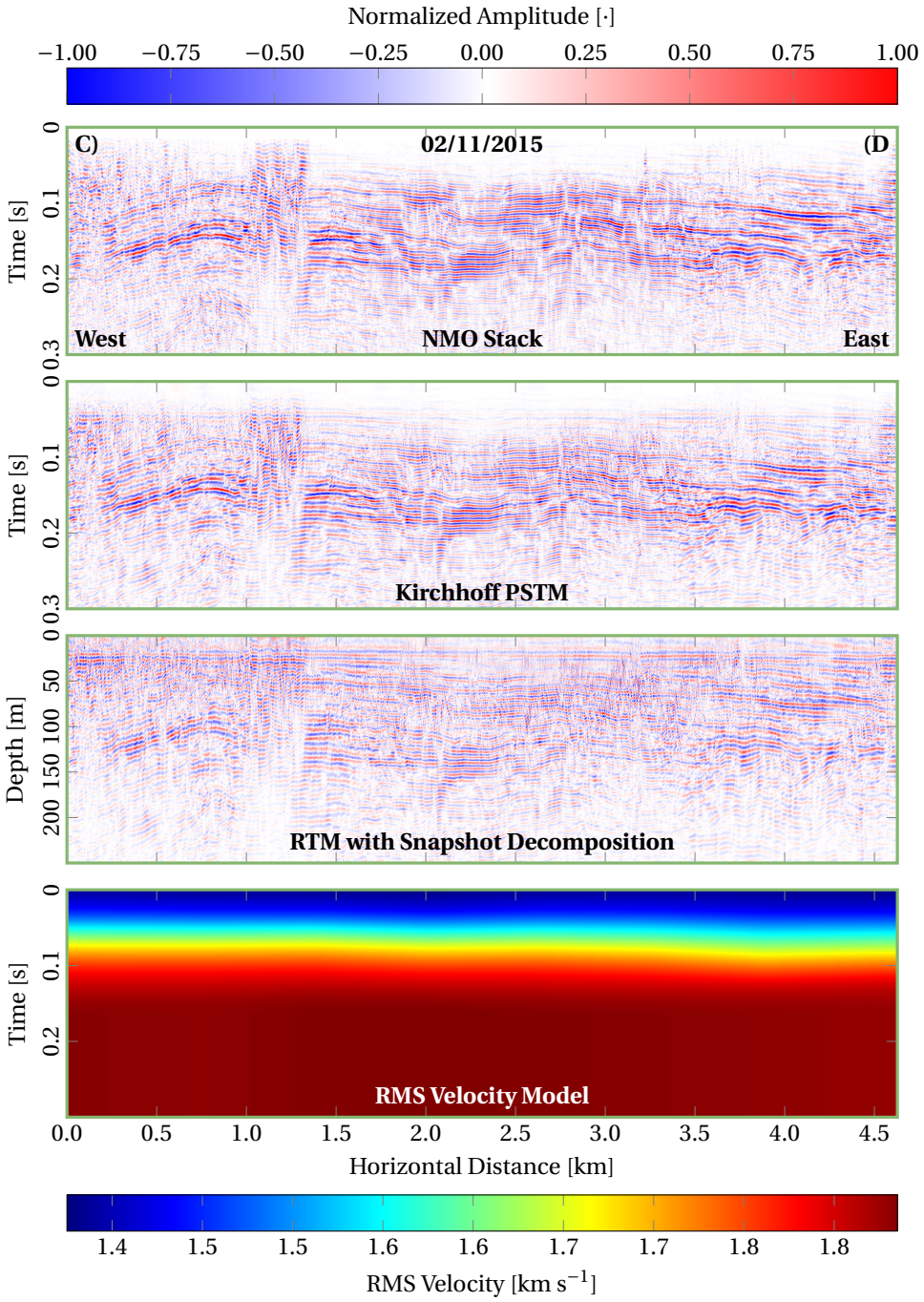

Figure A.11: Comparison of subsurface images from 02/11/2015. For the location of the cross-sections see Figure A.2; axis-border colour corresponds to track colour.

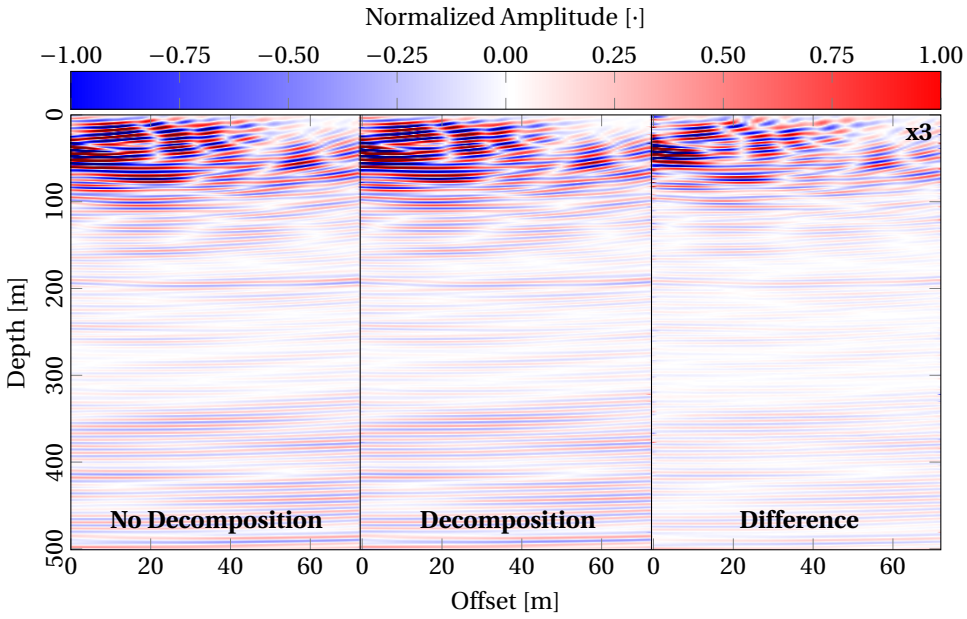

Figure A.12: Comparison of single-shot reverse time migrated data without (a) and with (b) snapshot decomposition before imaging. c) shows the difference between (a) and (b).

and airgun-recharge time, ~4 s. This led to near-surface artefacts during reverse-time migration where insufficient source and receiver sampling could not cancel out artefacts. As such, the near surface image looks the best on the NMO stacks.

If this survey were to be repeated a couple of things should be changed. First a single streamer should be used, the setup of three different streamers combined into one, in the way that it was implemented, did not work well. If the streamers were kept further apart and were not connected to each other at 75 m and 150 m, respectively, some of the tube waves might have been avoidable. The challenge then would be to ensure correct offsets of the streamers with respect to each other. Alternatively the streamers could have been attached everywhere along their length; this would not give parts of the streamers sufficient space to generate a lot of slapping momentum, and, as such, would hopefully reduce tube-wave noise. It should be noted though that the concept of using multiple streamers does allow for unprecedented flexibility with respect to receiver spacing. It also allows for having the streamers in parallel, as in 3D surveys. This is limited by river width, but would allow for the detection of cross-line events from the river sides.

With respect to the absent P*S/Scholte-waves, it might have been an idea to extend the survey further South, better spots for P*S/Scholte-waves may have been found there (although the seismic may have been less geologically relevant). Going further west was not possible due to the border between Serbia and Croatia. It would also be interesting to go back and sample the mud at the bottom of the river, as a possible cause for the absent P*S and associated Scholte waves is a very viscous mud layer at the bottom of the river,

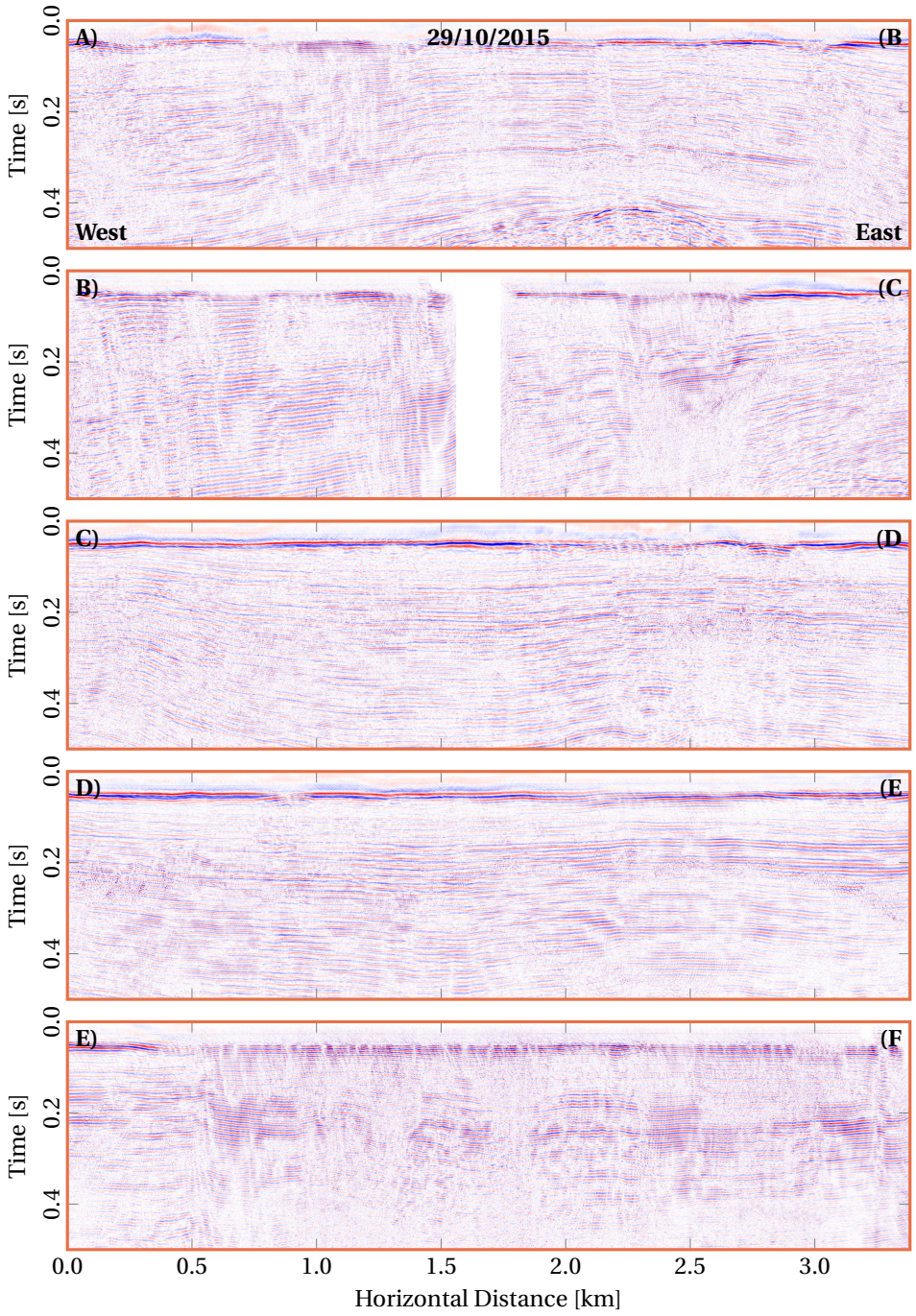

Figure A.13: RMS-amplitude-trace-balanced NMO stacks for 29/10/2015 by Vanić (2016). Same colour bar as in Figure A.11. For the location of the cross-sections see Figure A.2; axis-border colour indicates track.

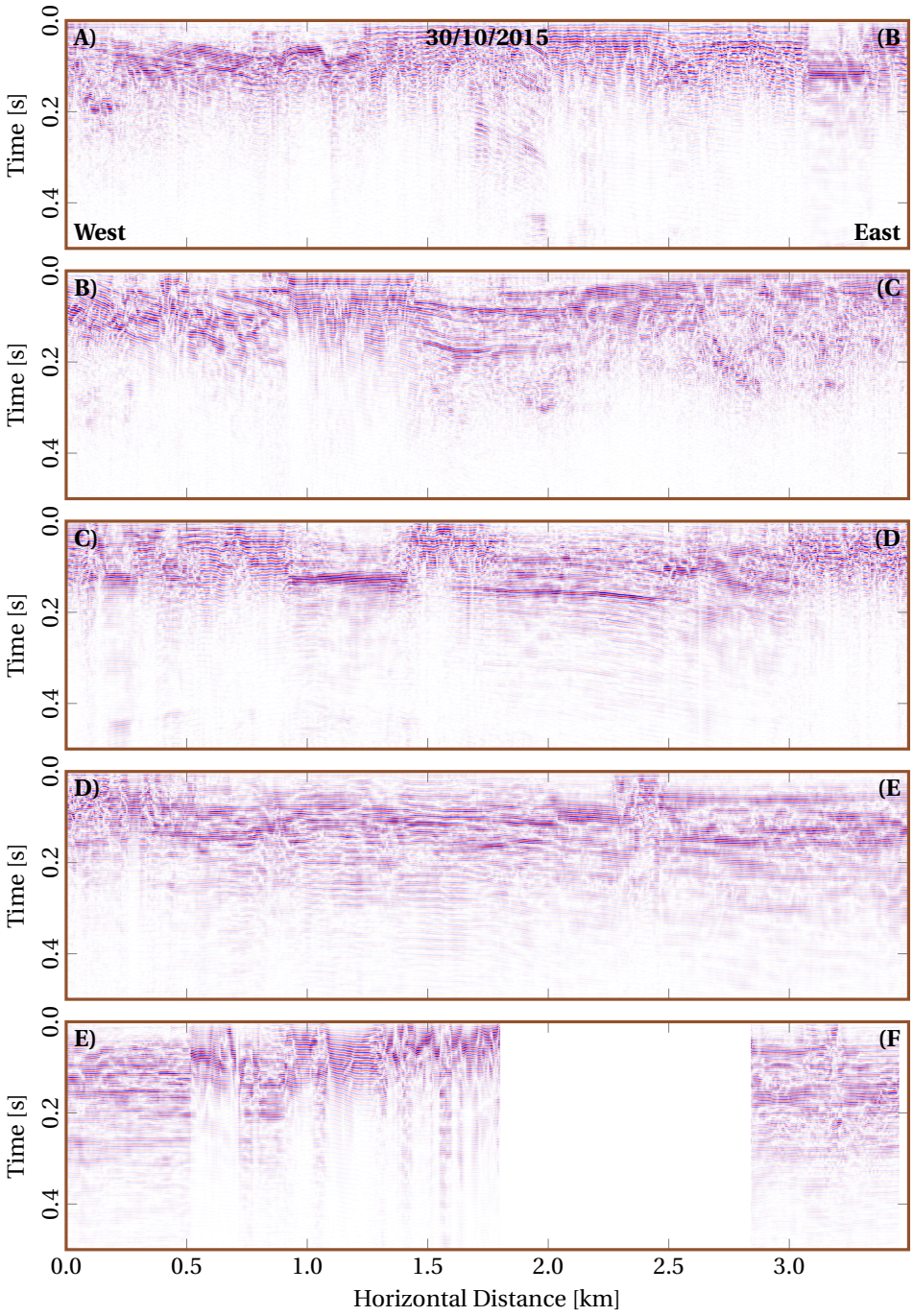

Figure A.14: RMS-amplitude-trace-balanced NMO stacks for 30/10/2015. Same colour bar as in Figure A.11. For the location of the cross-sections see Figure A.2; axis-border colour corresponds to track colour.

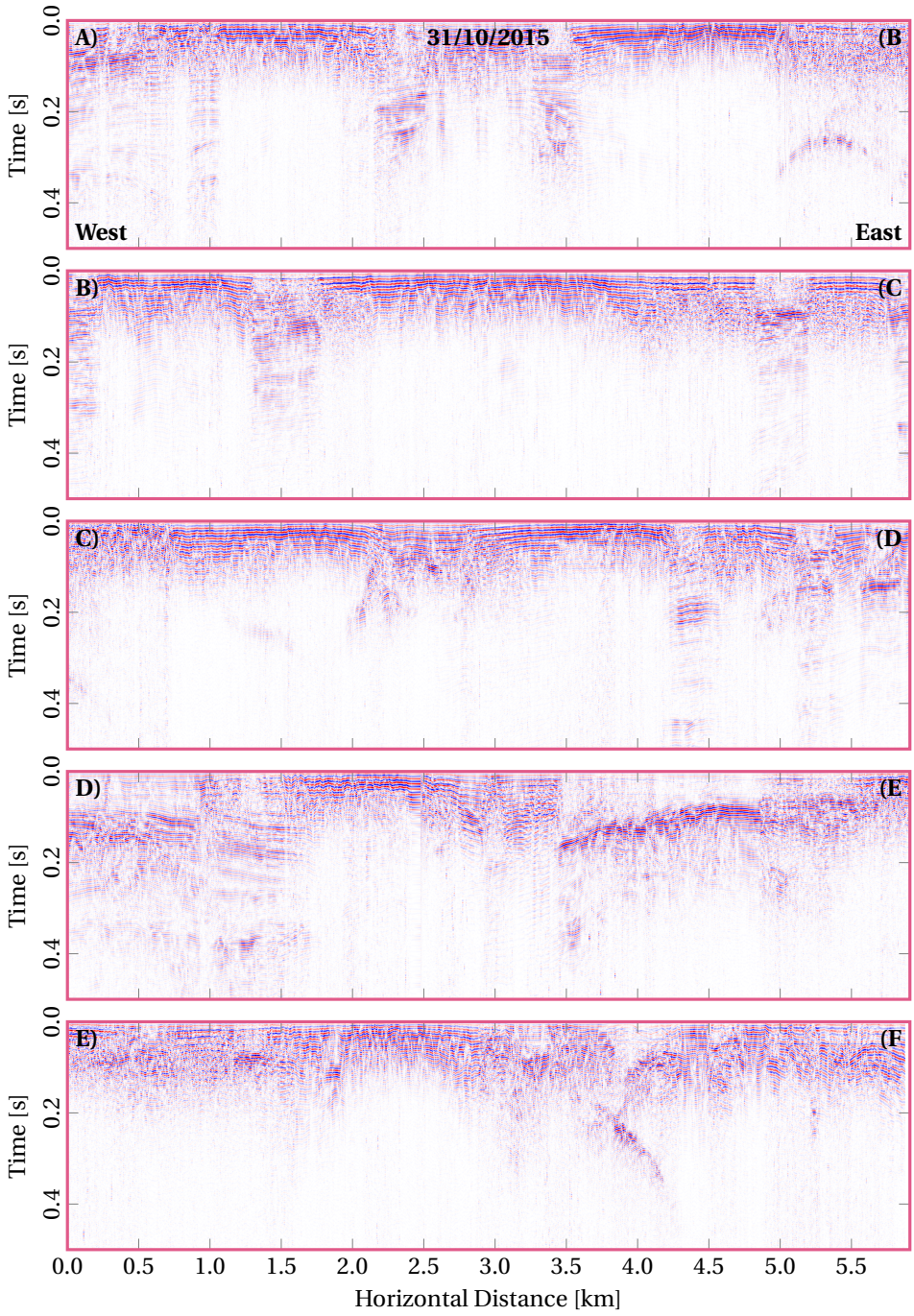

Figure A.15: RMS-amplitude-trace-balanced NMO stacks for 31/10/2015. Same colour bar as in Figure A.11. For the location of the cross-sections see Figure A.2; axis-border colour corresponds to track colour.

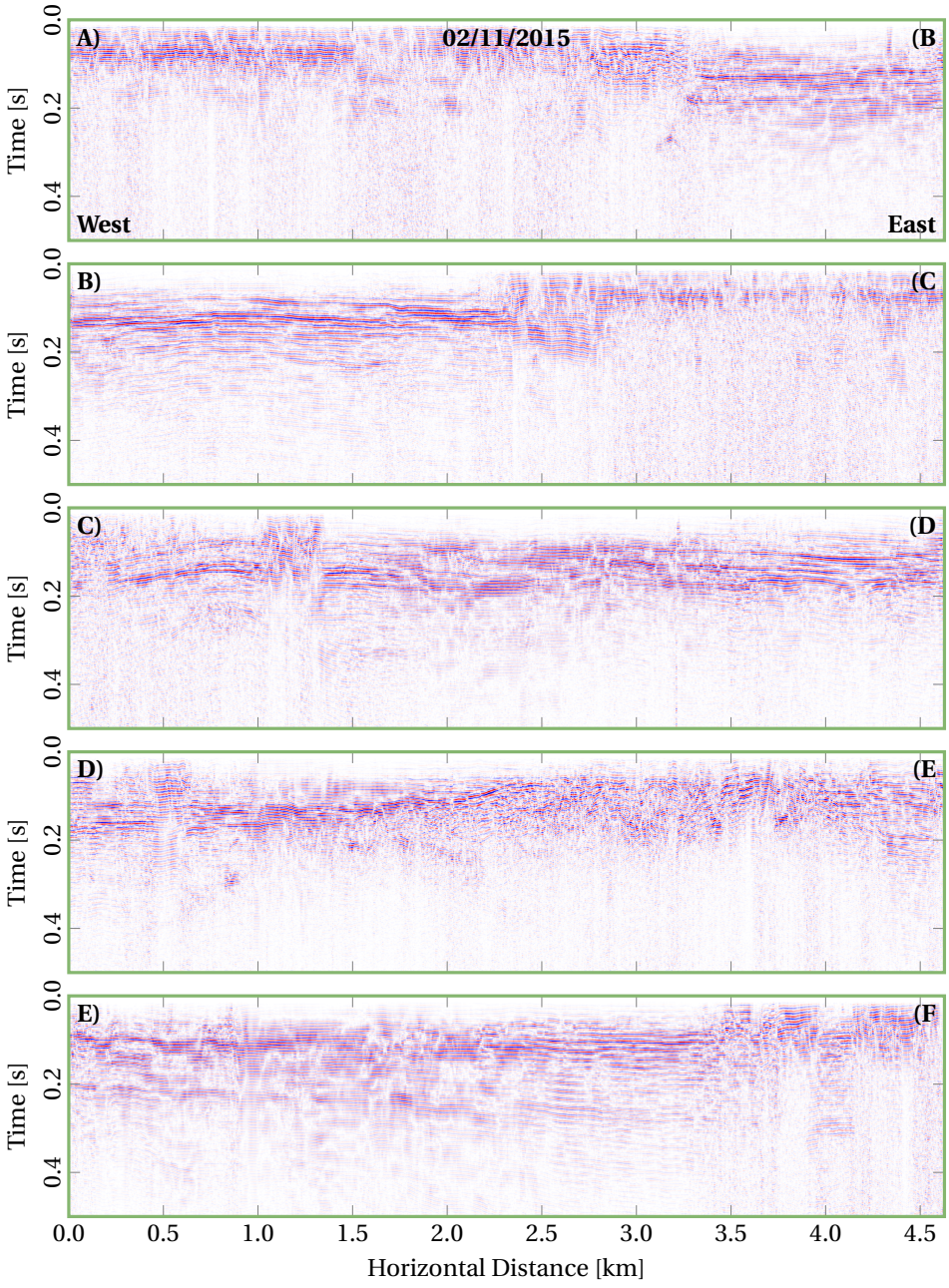

Figure A.16: RMS-amplitude-trace-balanced NMO stacks for the 02/11/2015. Same colour bar as in Figure A.11. For the location of the cross-sections see Figure A.2; axis-border colour corresponds to track colour.

as discussed in Vanić (2016).

A.7. CONCLUSION

Processing the Danube data was a challenge due to the noisy environment and the main goal of imaging P*S/Scholte waves could not be met, as only sparse P*S/Scholte waves could be found. On the other hand the P-wave processing did give good final stacks. These are interpretable with some caution as some high-frequency events in them may be cross-line riverbank reflections for example. This survey, however, was the first survey of its kind in the area and should help to constrain the geology of the Fruška Gora mountain.

B

Equation 4.22 is a Solution to the Acoustic Wave Equation With Source Terms

We here wish to demonstrate that Equation 4.22:

$$p = \cos\left(\omega_0[\, t - \boldsymbol{s}_O \cdot \boldsymbol{x}_O\,]\right) e^{-\omega_0 \sigma_z |z|}, \tag{4.22}$$

is a solution to the acoustic wave equation with source terms. For this we introduce, following Wapenaar and Berkhout (1989), the acoustic wave equation as:

$$\left(\frac{1}{c^2}\partial_t^2 - \Delta\right) p = \rho \partial_t^2 i_v, \tag{B.1}$$

where i_v denotes the volume-injection source distribution. We assume there are no force sources.

Equation 4.22 is generated by a plane of volume-injection sources at $z = 0$ that inject a plane cosine wave. We can write the responsible volume injection source as:

$$i_v = -2\frac{\sigma_z}{\omega_0 \rho}\delta(z)\cos(\omega_0[t - \boldsymbol{s}_O \cdot \boldsymbol{x}_O]). \tag{B.2}$$

We now want to check that Equation 4.22 satisfies Equation B.1 for this source distribution, Equation B.2. Inserting Equation 4.22 into the left-hand side of Equation B.1 we find:

$$\left(\frac{1}{c^2}\partial_t^2 - \Delta\right) p = \omega_0^2 \left[\left(\boldsymbol{s}_O \cdot \boldsymbol{s}_O - \frac{1}{c^2}\right) - [\partial_z |z|]^2 \sigma_z^2 + 2\frac{\sigma_z}{\omega_0}\delta(z)\right] p. \tag{B.3}$$

To further simplify this expression we need to discuss the behaviour of $[\partial_z |z|]^2$. For $z \neq 0$ $[\partial_z |z|]^2 = 1$, for $z = 0$ $[\partial_z |z|]^2$ is undefined. Recall that we would treat this function as a

distribution, which means that we can define the value in terms of limits. If we take the limit as we approach either side of $z = 0$ then the double sided limit of $[\partial_z |z|]^2$ is one. As such we define that:

$$[\partial_z |z|]^2 \equiv 1. \tag{B.4}$$

B

With this and the help of Equation 4.20, which defines the evanescent slowness σ_z as the term inside the parentheses in Equation B.3, we can simplify Equation B.3 to:

$$\left(\frac{1}{c^2}\partial_t^2 - \Delta\right) p = 2\omega_0 \sigma_z \delta(z) \cos(\omega_0 [t - \boldsymbol{s}_O \cdot \boldsymbol{x}_O]). \tag{B.5}$$

Inserting the volume injection source, Equation B.2, into the right-hand side of Equation B.1 we find:

$$\rho \partial_t^2 i_v = 2\omega_0 \sigma_z \delta(z) \cos(\omega_0 [t - \boldsymbol{s}_O \cdot \boldsymbol{x}_O]). \tag{B.6}$$

This is equal to the right-hand side of Equation B.5, and hence Equation 4.22 satisfies the acoustic wave equation, Equation B.1, for the $z = 0$ volume-injection source plane as defined in Equation B.2.

C

Alternative Derivation Of Directional Acoustic Snapshot Wavefield Decomposition For RTM

To directionally decompose snapshots of an acoustic wavefield in homogeneous media, following **Holicki** et al. (2019), under the relaxed condition of operating on a snapshot and its time derivative or integral, consider the source-free linearized acoustic pressure wave equation:

$$\partial_t^2 p = c^2 \Delta p, \tag{C.1}$$

where Δ denotes the Laplacian, or sum of second order spatial derivatives. To simplify the following derivation we transform Equation C.1 to the full wavenumber domain:

$$\partial_t^2 \tilde{p} = -c^2 \boldsymbol{k} \cdot \boldsymbol{k} \tilde{p}, \tag{C.2}$$

We can combine the identity $\partial_t \tilde{p} = \partial_t \tilde{p}$ with Equation C.2 to formulate the following linear system:

$$\partial_t \begin{pmatrix} 1 \\ \partial_t \end{pmatrix} \tilde{p} = \begin{pmatrix} 0 & 1 \\ -c^2 \boldsymbol{k} \cdot \boldsymbol{k} & 0 \end{pmatrix} \begin{pmatrix} 1 \\ \partial_t \end{pmatrix} \tilde{p}, \tag{C.3}$$

which we can write in matrix notation as:

$$\partial_t \tilde{\boldsymbol{q}} = \tilde{\boldsymbol{A}} \tilde{\boldsymbol{q}}, \tag{C.4}$$

where:

$$\tilde{\boldsymbol{q}} = \begin{pmatrix} 1 \\ \partial_t \end{pmatrix} \tilde{p}, \tag{C.5}$$

$$\tilde{\boldsymbol{A}} = \begin{pmatrix} 0 & 1 \\ -c^2 \boldsymbol{k}\cdot\boldsymbol{k} & 0 \end{pmatrix}. \tag{C.6}$$

If we now apply eigenvalue decomposition to this system we find:

$$\partial_t \tilde{\boldsymbol{q}} = \tilde{\boldsymbol{L}}\tilde{\boldsymbol{\Lambda}}\tilde{\boldsymbol{L}}^{-1}\tilde{\boldsymbol{q}}, \tag{C.7}$$

where the eigenvector and eigenvalue matrices, $\tilde{\boldsymbol{L}}$ and $\tilde{\boldsymbol{\Lambda}}$ respectively, are defined as:

C

$$\tilde{\boldsymbol{L}} = \begin{pmatrix} 1 & 1 \\ ci\sqrt{\boldsymbol{k}\cdot\boldsymbol{k}} & -ci\sqrt{\boldsymbol{k}\cdot\boldsymbol{k}} \end{pmatrix}, \tag{C.8}$$

$$\tilde{\boldsymbol{\Lambda}} = \begin{pmatrix} ci\sqrt{\boldsymbol{k}\cdot\boldsymbol{k}} & 0 \\ 0 & -ci\sqrt{\boldsymbol{k}\cdot\boldsymbol{k}} \end{pmatrix}. \tag{C.9}$$

In Chapter 2 it was found, among other normalizations of the eigenvectors, that choosing the signs of the square roots according to the vertical wavenumber leads to up-down wavefield decomposition. Hence we choose to sign the wavenumber square root according to κ_z from Equation 2.30:

$$k_{r,z} = \sqrt{\boldsymbol{k}\cdot\boldsymbol{k}} = \operatorname{sign}(\kappa_z)\,|\boldsymbol{k}|. \tag{C.10}$$

We can now define the directionally decomposed wavefields $\boldsymbol{d}$ in terms of Equation C.7 as:

$$\tilde{\boldsymbol{d}} = \tilde{\boldsymbol{L}}^{-1}\tilde{\boldsymbol{q}}, \tag{C.11}$$

where the inverse of the eigenvector matrix is:

$$\tilde{\boldsymbol{L}}^{-1} = \frac{1}{2}\begin{pmatrix} 1 & (cik_{r,z})^{-1} \\ 1 & -(cik_{r,z})^{-1} \end{pmatrix}. \tag{C.12}$$

The decomposed fields then read:

$$\begin{pmatrix} \tilde{p}^{+} \\ \tilde{p}^{-} \end{pmatrix} = \frac{1}{2}\begin{pmatrix} 1 & (cik_{r,z})^{-1} \\ 1 & -(cik_{r,z})^{-1} \end{pmatrix}\begin{pmatrix} 1 \\ \partial_t \end{pmatrix}\tilde{p}. \tag{C.13}$$

Comparing Equations C.13 to 2.34 we no longer have the numerator. Instead we now divide by the magnitude of the wavenumber vector signed according to κ_z. This means that low-wavenumber noise is amplified while high-wavenumber noise is suppressed. We also divide by the acoustic wave speed instead of multiplying with the specific acoustic impedance. This form of decomposition is evidently also mass density independent, only the medium velocity needs to be known. This has important implications for wavefield decomposition as often the density in real media is not known, even in the vicinity of recording devices. With this type of decomposition it is not necessary to know the density.

Note that if one wants to cast the decomposition in terms of $cik_{r,z}$ instead of its inverse one needs to use the temporal primitive of the pressure instead of the time derivative. To convert from one normalization to the other we rewrite the full wavenumber-domain acoustic pressure wave equation as:

$$\partial_t \tilde{p} = -c^2 \boldsymbol{k}\cdot\boldsymbol{k}\,\partial_t^{-1}\tilde{p} = (cik_r)^2\,\partial_t^{-1}\tilde{p}, \tag{C.14}$$

where ∂_t^{-1} should be understood as a temporal primitive, or indefinite temporal integration with a zero constant of integration. With this transform the decomposition reads:

$$\begin{pmatrix} \tilde{p}^+ \\ \tilde{p}^- \end{pmatrix} = \frac{1}{2} \begin{pmatrix} 1 & cik_r \\ 1 & -cik_r \end{pmatrix} \begin{pmatrix} 1 \\ \partial_t^{-1} \end{pmatrix} \tilde{p}. \tag{C.15}$$

Decomposition of acoustic single-component wavefields as they are forward or backward modelled in time using, for example, finite-difference techniques, has turned out to be a simple wavenumber-domain operation. Although the described method only works in homogeneous media, it can be easily approximated to heterogeneous media by allowing the propagation velocity to vary spatially, $c = c(\boldsymbol{x})$, and transforming $-ik_r\partial_t^{-1}\tilde{p}$ back to the space domain before multiplying with the spatially varying wave speed $c(x)$.

In finite-difference RTM it is often easier to use Equation C.13 than Equation C.15 as the time derivative is implicitly computed by the employed finite-difference operators. However, Equation C.15 is less sensitive to numerical errors in the time derivative, but amplifies high-wavenumber artefacts, whereas Equation C.13 amplifies low-wavenumber artefacts.

BIBLIOGRAPHY

Aki, K. and P. Richards (2002). *Quantitative seismology*. Vol. 1. University Science Books.

Allouche, N.el (2011). "Converted waves in shallow marine environments: modelling and field experiments". PhD thesis. Delft University of Technology. ISBN: 9789088913341.

Allouche, N.el, G.G. Drijkoningen, W. Versteeg, and R. Ghose (2011). "Converted waves in a shallow marine environment: Experimental and modeling studies". In: *Geophysics* vol. 76, no. 1, T1–T11. ISSN: 00168033. DOI: 10.1190/1.3511524.

Almagro Vidal, C., D. Draganov, J. van der Neut, G.G. Drijkoningen, and K. Wapenaar (2014). "Retrieval of reflections from ambient noise using illumination diagnosis". In: *Geophysical Journal International* vol. 198, no. 3, pp. 1572–1584. DOI: 10.1093/gji/ggu164.

Amdahl, G.M. (1967). "Validity of the single processor approach to achieving large scale computing capabilities". In: *Proceedings of the April 18-20, 1967, spring joint computer conference*, pp. 483–485.

Amundsen, L. and A. Reitan (1995). "Decomposition of multicomponent sea-floor data into upgoing and downgoing P- and S-waves". In: *Geophysics* vol. 60, pp. 563–572.

Amundsen, L. and J.O.A. Robertsson (2014). "Wave equation processing using finite-difference propagators, Part 1: Wavefield dissection and imaging of marine multicomponent seismic data". In: *GEOPHYSICS* vol. 79, no. 6, T287–T300. DOI: 10.1190/geo2014-0151.1.

Barr, F. and J. Sanders (1989). "Attenuation of water-column reverberations using pressure and velocity detectors in a water-bottom cable". In: *SEG Technical Program Expanded Abstracts 1989*, pp. 653–656. DOI: 10.1190/1.1889557.

Baysal, E., D.D. Kosloff, and J.W.C. Sherwood (1983). "Reverse time migration". In: *Geophysics* vol. 48, no. 11, pp. 1514–1524. DOI: 10.1190/1.1441434.

Bizley, D. (22, 2016). *Polarcus breaking records with largest man-made moving object*. Oilfield Technology. URL: https://www.oilfieldtechnology.com/exploration/22012016/polarcus-breaking-records-with-largest-man-made-moving-object/ (visited on Aug. 30, 2019).

Brougois, A., M. Bourget, P. Lailly, M. Poulet, P. Ricarte, and R. Versteeg (1990). "Marmousi, model and data". In: *EAEG Workshop-Practical Aspects of Seismic Data Inversion*.

Caffarelli, L. and L. Silvestre (2007). "An extension problem related to the fractional Laplacian". In: *Communications in partial differential equations* vol. 32, no. 8, pp. 1245–1260.

Chen, T. and B. He (2014). "A normalized wavefield separation cross-correlation imaging condition for reverse time migration based on Poynting vector". In: *Applied Geophysics* vol. 11, no. 2, pp. 158–166.

Chew, W. and Q. Liu (1996). "Perfectly matched layers for elastodynamics: a new absorbing boundary condition". In: *Journal of Computational Acoustics* vol. 4, no. 4, pp. 341–359.

Claerbout, J. (1985). *Imaging the earth's interior*. Vol. 1. Blackwell scientific publications Oxford.

Cohen, J.K. and J.J.W. Stockwell (2008). *CWP/SU: Seismic Un*x Release No. 4.0: an open source software package for seismic research and processing*. Version 4.0. URL: https://github.com/JohnWStockwellJr/SeisUnix/wiki (visited on Apr. 30, 2016).

Dankbaar, J.W.M. (1985). "Separation of P- and S-waves". In: *Geophysical Prospecting* vol. 33, pp. 970–986.

De Hoop, A. and J. van der Hijden (1984). "Generation of acoustic waves by an impulsive point source in a fluid/solid configuration with a plane boundary". In: *The Journal of the Acoustical Society of America* vol. 75, no. 6, pp. 1709–1715.

— (1985). "Seismic waves generated by an impulsive point source in a solid/fluid configuration with a plane boundary". In: *Geophysics* vol. 50, no. 7, pp. 1083–1090.

Deming, W.E. (1943). "Statistical adjustment of data". In: Published, in part, in 1938 in mimeographed form under the title: Some notes on least squares.

Department of Defense (2008). *Global Positioning System Standard Positioning Service Performance Standard*. Department of Defense.

Díaz, E. and P. Sava (2015). "Understanding the reverse time migration backscattering: noise or signal?" In: *Geophysical Prospecting* vol. 64, no. 3, pp. 581–594. DOI: 10.1111/1365-2478.12232.

Drijkoningen, G.G., D. Dieulangard, E. Kjos, and **M.E. Holicki** (2015). "Air Gun near the Sea Floor as Shear-wave Source?" In: *77th EAGE Conference and Exhibition 2015*. DOI: 10.3997/2214-4609.201413356.

Drijkoningen, G.G., N. el Allouche, J. Thorbecke, and G. Bada (2012). "Nongeometrically converted shear waves in marine streamer data". In: *Geophysics* vol. 77, no. 6, P45–P56. DOI: 10.1190/geo2012-0037.1.

Fei, T.W., Y. Luo, S. Aramco, and G.T. Schuster (2010). "De-blending reverse-time migration". In: *SEG Technical Program Expanded Abstracts 2010*. Society of Exploration Geophysicists, pp. 3130–3134.

Frasier, C. (1970). "Discrete time solution of plane P-SV waves in a plane layered medium". In: *Geophysics* vol. 35, no. 2, pp. 197–219. DOI: 10.1190/1.1440085.

Frigo, M. and S. Johnson (2005). "The Design and Implementation of FFTW3". In: *Proceedings of the IEEE* vol. 93, no. 2, pp. 216–231. ISSN: 0018-9219. DOI: 10.1109/JPROC.2004.840301.

Grimbergen, J., F. Dessing, and K. Wapenaar (1998). "Modal expansion of one-way operators in laterally varying media". In: *Geophysics* vol. 63, no. 3, pp. 995–1005.

SEG-Y_r2.0: SEG-Y revision 2.0 Data Exchange format (2017). Standard. Tulsa, Ok 74170-2740, USA: SEG Technical Standards Committee.

Hemon, C. (1978). "EQUATIONS D'ONDE ET MODELES". In: *Geophysical Prospecting* vol. 26, no. 4, pp. 790–821. DOI: 10.1111/j.1365-2478.1978.tb01634.x.

Holicki, **M.E.** and G.G. Drijkoningen (2016). "Extending RTM Imaging With a Focus on Head Waves". In: *EGU General Assembly Conference Abstracts*. Vol. 18. EGU General Assembly Conference Abstracts, EPSC2016–14494.

Holicki, **M.**, G. Drijkoningen, and K. Wapenaar (2017). "Snapshot Wavefield Decomposition For Heterogeneous Velocity Media". In: *79th EAGE Conference and Exhibition 2017*. European Associaion of Geoscientists and Engineers.

— (2019). “Acoustic Directional Snapshot Wavefield Decomposition”. In: *Geophysical Prospecting* vol. 67, no. 1, pp. 32–51. DOI: 10.1111/1365-2478.12700.

Holicki, M., K. Wapenaar, and G. Drijkoningen (2016). “Time-slice wavefield decomposition”. In: *SEG Technical Program Expanded Abstracts 2016*. Society of Exploration Geophysicists, pp. 4367–4371.

Jones, I. (2014). “Tutorial: migration imaging conditions”. In: *First Break* vol. 32, no. 12, pp. 45–55.

Kennett, B. (1984). “AN OPERATOR APPROACH TO FORWARD MODELING, DATA PROCESSING AND MIGRATION”. In: *Geophysical Prospecting* vol. 32, no. 6, pp. 1074–1090. DOI: 10.1111/j.1365-2478.1984.tb00755.x.

Leaney, K. and E. Schlumberger (1990). “Parametric wavefield decomposition and applications”. In: *1990 SEG Annual Meeting*. Society of Exploration Geophysicists.

Lindstrom, P. (2014). “Fixed-Rate Compressed Floating-Point Arrays”. In: *IEEE Transactions on Visualization and Computer Graphics* vol. 20, no. 12, pp. 2674–2683. DOI: 10.1109/TVCG.2014.2346458.

Liu, F., G. Zhang, S. Morton, and J. Leveille (2011). “An effective imaging condition for reverse-time migration using wavefield decomposition”. In: *Geophysics* vol. 76, no. 1, S29–S39.

Lu, S., D. Whitmore, A. Valenciano, and N. Chemingui (2015). “Separated-wavefield imaging using primary and multiple energy”. In: *The Leading Edge* vol. 34, no. 7, pp. 770–778.

Luo, S. and D. Hale (2012). “Velocity analysis using weighted semblance”. In: *Geophysics* vol. 77, no. 2, U15–U22. DOI: 10.1190/geo2011-0034.1.

Margrave, G.F. and M.P. Lamoureux (2019). *Numerical Methods of Exploration Seismology: With Algorithms in MATLAB™*. Cambridge University Press.

Matenco, L. and D. Radivojević (2012). “On the formation and evolution of the Pannonian Basin: Constraints derived from the structure of the junction area between the Carpathians and Dinarides”. In: *Tectonics* vol. 31, no. 6.

McMechan, G. (1983). “Migration By Extrapolation Of Time-Dependent Boundary Values”. In: *Geophysical Prospecting* vol. 31, no. 3, pp. 413–420. ISSN: 1365-2478. DOI: 10.1111/j.1365-2478.1983.tb01060.x.

Poynting, J. (1884). “On the transfer of energy in the electromagnetic field”. In: *Philosophical Transactions of the Royal Society of London* vol. 175, pp. 343–361.

QGIS Development Team (2018). *QGIS: Geographic Information System*. Open Source Geospatial Foundation. URL: http://qgis.org (visited on Nov. 19, 2018).

Revelo, D. and R. Pestana (2019). “Up/Down acoustic wavefields decomposition using a single propagation and its application in reverse time-migration”. In: *Geophysics* vol. 84, no. 4, pp. 1–82.

Robertsson, J.O.A., D.-J. van Manen, C. Schmelzbach, C. Van Renterghem, and L. Amundsen (2015). “Finite-difference modelling of wavefield constituents”. In: *Geophysical Journal International* vol. 203, no. 2, pp. 1334–1342. ISSN: 0956-540X. DOI: 10.1093/gji/ggv379.

Scheimer, J. and I. Borg (1984). “Deep seismic sounding with nuclear explosives in the Soviet Union”. In: *Science* vol. 226, no. 4676, pp. 787–792.

C

SEG-D, Rev 3.1 (2015). Standard. Tulsa, Ok 74170-2740, USA: SEG Technical Standards Committee.

Shen, P. and U. Albertin (2015). "Up-down separation using Hilbert transformed source for causal imaging condition". In: *SEG Technical Program Expanded Abstracts 2015*. Society of Exploration Geophysicists, pp. 4175–4179.

Slade, G.W. (2013). "The fast fourier transform in hardware: A tutorial based on an FPGA implementation". In: *ResearchGate*.

Suprajitno, M. and S. Greenhalgh (1985). "Separation of upgoing and downgoing waves in vertical seismic profiling by contour-slice filtering". In: *Geophysics* vol. 50, no. 6, pp. 950–962.

Thorbecke, J. and D. Draganov (2011). "Finite-difference modeling experiments for seismic interferometry". In: *Geophysics* vol. 76, no. 6, H1–H18. DOI: 10.1190/geo2010-0039.1.

Toljić, M., L. Matenco, M.N. Ducea, U. Stojadinović, J. Milivojević, and N. Đerić (2013). "The evolution of a key segment in the Europe–Adria collision: The Fruška Gora of northern Serbia". In: *Global and Planetary Change* vol. 103, pp. 39–62.

Ursin, B. (1983). "Review of elastic and electromagnetic wave propagation in horizontally layered media". In: *Geophysics* vol. 48, no. 8, pp. 1063–1081.

Vanić, M.S. (2016). "Combined P- and Converted-Wave Processing and Interpretation for shallow-seismic riverine data from the Fruška Gora region". MSc thesis. Delft University of Technology.

Wapenaar, C. and A. Berkhout (1989). *Elastic wave field extrapolation: Redatuming of single-and multi-component seismic data*. Elsevier.

Wapenaar, C., P. Herrmann, D. Verschuur, and A. Berkhout (1990). "Decomposition of multicomponent seismic data into primary P- and S-wave responses". In: *Geophysical Prospecting* vol. 38, no. 6, pp. 633–661.

White, J.E. (1965). *Seismic waves; Radiation, transmission, and attenuation*. McGraw-Hill, New York.

Whitmore, N. (1983). "Iterative depth migration by backward time propagation". In: *SEG Technical Program Expanded Abstracts 1983*, pp. 382–385. DOI: 10.1190/1.1893867.

Yilmaz, Ö. (2001). *Seismic Data Analysis*. 2nd ed. Society of Exploration Geophysicists. ISBN: 9781560800989. DOI: 10.1190/1.9781560801580.

Yoon, K. and K. Marfurt (2006). "Reverse-time migration using the Poynting vector". In: *Exploration Geophysics* vol. 37, no. 1, pp. 102–107. DOI: 10.1071/EG06102.

Zhang, S., S. Wang, A. Zhang, and Y. Li (2017). "Numerical study on attenuation of bubble pulse through tuning the air-gun array with the particle swarm optimization method". In: *Applied Ocean Research* vol. 66, pp. 13–22. ISSN: 0141-1187. DOI: 10.1016/j.apor.2017.05.007.

CURRICULUM VITÆ

Max Enno HOLICKI

09/04/1990 Born in Stade, Germany.

EDUCATION

1997–1998 Church Hill First School, Norfolk, The United Kingdom
1998–2000 Grimston Junior School, Norfolk, The United Kingdom
2000–2002 Antwerp International School, Belgium
2002–2006 Zürich International School, Switzerland
2006–2008 Antwerp International School, Belgium
International Baccalaureate

2008–2011 B.Sc. in Earth & Space Sciences
Jacobs University Bremen, Germany
Thesis: Graviational Modelling of Olympus Mons
Supervisors: Prof.dr. V. Unnithan & Prof.dr. J. Voigt

2011–2013 M.Sc. IDEA League Applied Geophysics
Technische Universiteit Delft, The Netherlands
Eidgenössische Technische Hochschule Zürich, Switzerland
Rheinisch-Westfälische Technische Hochschule Aachen, Germany
Schlumberger Oilfield Services, Gatwick, The United Kingdom
Thesis: Automated Seismic Interference Detection In Marine Acquisition Scenarios
Supervisors: Dr. S. Rentsch & Dr. M. Vasallo

2013–2020 Ph.D. in Applied Geophysics
Delft University of Technology, The Netherlands
Thesis: Directional Wavefield Decomposition of Snapshots of Acoustic Wavefields
Promotors: Dr.ir. G.G. Drijkoningen & Prof.dr.ir. C.P.A. Wapenaar